EFFECT OF MICROSTRUCTURE AND INTERNAL HYDROGEN ON FATIGUE CRACK PROPAGATION OF ULTRAHIGH STRENGTH STEELS

Narayana Sastry Cheruvu

A.M.I.I.M., (1972), M.E. (1975)

A dissertation submitted to the faculty
of the Oregon Graduate Center
in partial fulfillment of the
requirements for the degree
Doctor of Philosophy
in
Materials Science

September, 1980

The dissertation "Effect of Microstructure and Internal Hydrogen on Fatigue Crack Propagation of Ultrahigh Strength Steels" by Narayana Sastry Cheruvu has been examined and approved by the following Examination Committee:

William E. Wood, Thesis Advisor
Associate Professor

John S. Blakemore
Professor

Jack H. Devletian
Associate Professor

Nicholas G. Eror
Associate Professor

ACKNOWLEDGEMENTS

I wish to express my thanks to Dr. W. E. Wood, who has not only provided me facilities to carry out this work but also has given me moral support during this period.

I am most grateful to Dr. Warren Garison, who carried out magnetic saturation analysis experiments for me.

I would also like to thank Mr. Rao Gudimetla for his help in computer programming and for many valuable discussions during the course of this work. In addition, I would like to thank Mr. R. Padmanabhan and Mr. S. Shankar for their valuable suggestions while preparing this thesis.

I am also grateful to Mrs. Barbara Ryall for her drawings and Ms. Nancy Fick for her long hours of typing.

I am also indebted to Ms. Mel Marsh, who helped me and my family during my stay in Oregon. I owe a special debt of gratitude to my wife, Raja, for standing by me throughout this work.

TABLE OF CONTENTS

Page

LIST OF TABLES

LIST OF FIGURES

ABSTRACT

Effect of Microstructure and Internal Hydrogen on Fatigue Crack Propagation of Ultrahigh Strength Steels

Narayana Sastry Cheruvu, Ph.D.
Oregon Graduate Center, 1980

Supervising Professor: William E. Wood

The effect of microstructure and internal hydrogen on fatigue crack propagation of quenched and tempered AISI 4340 steel has been investigated. The microstructural variables viz., prior austenite grain size, substructure of martensite, retained austenite and type of carbides were altered by choosing various austenitizing temperatures and tempering temperatures. Optical metallography and transmission electron microscopy were used to characterize these microstructural variables. Significant amounts of retained austenite films were observed at the lath and prior austenite grain boundaries, particularly in the coarse grained structures. The retained austenite was mechanically unstable ahead of a crack tip, and as well as during tensile deformation under plane stress and plane strain conditions.

The microstructural variations that were induced by various heat treatments used in this study did not significantly affect the threshold stress intensity for fatigue crack growth. Crack growth rates near threshold stress intensity and at intermediate stress intensity ranges were nearly independent of microstructure. However, the specimens with higher fracture toughness exhibited better resistance to crack growth at high stress intensity ranges than the specimens with lower fracture toughness.

However, the presence of internal hydrogen enhanced the crack growth rates by an order of magnitude over that of the specimens without hydrogen. The magnitude of enhancement in crack growth rates was dependent on the applied stress intensity range and on the prior austenite grain size. The maximum crack growth enhancement was observed at an intermediate stress intensity range, $\Delta K = 8$ to 15 Ksi$\sqrt{in}$, ($\Delta K = 8.8$ to 16.5 Mpa$\sqrt{m}$) for all prior austenite grain sizes. The crack growth rate at low stress intensity ranges ($\Delta K < 10$ Ksi$\sqrt{in}$) was very sensitive to the prior austenite grain size. Specimens with coarse grained structures exhibited lower crack growth rates than those with fine grain structures. The crack growth mode at low applied stress intensities in the coarse grained structures was predominantly transgranular fracture while in fine grained structures it was mostly intergranular. Crack growth rates in specimens tempered at 280°C for all grain sizes were slightly higher at intermediate applied stress intensity ranges than in specimens tempered at 180°C. These results are discussed in terms of the fracture mode and the diffusion of hydrogen to the prior austenite grain boundaries.

1. INTRODUCTION

Low alloy ultrahigh strength steels such as 4340 are conventionally heat treated at 870°C for 1 hr. prior to oil quenching and tempered at a suitable temperature to achieve optimum mechanical properties (strength and ductility). These steels are rarely used above 200 Ksi (1380 Mpa) yield strength levels because of their poor toughness at these strength levels. In recent years, substantial work has been carried out[1-7] to improve plane strain fracture toughness of these steels without affecting yield strength. These investigations have led to a conclusion that the plane strain fracture toughness of ultrahigh strength low alloy steels can be improved by two fold, without changing the basic alloy, by austenitizing at higher temperatures than normally employed 870°C. This improvement in plane strain fracture toughness was basically attributed to the variation in microstructure and to the reduction of segregation of impurity and alloying elements.[1-7]

By using the plane strain fracture toughness, K_{1c}, it is possible to predict the critical flaw or defect size for a given stress level in a brittle structural component. However, subcritical size cracks grow in structures, which are inherently present in any structural material, to a critical size under cyclic loading or static loading particularly in the presence of corrosive environment followed by catastrophic failure. Unfortunately, the plane strain fracture toughness does not give any information about subcritical crack growth rates in service. The nature of subcritical crack growth rates in service particularly under cyclic loading is as important as, if not more important than, the plane strain fracture toughness since many structural failures are due to fatigue. Very limited data are available on the effect of these modified heat treatments on fatigue crack growth behavior of ultrahigh strength low alloy steels.[8,9]

Furthermore, the ultrahigh strength low alloy steels are more susceptible to hydrogen embrittlement, and this increases the probability of premature service failures of structures. A few parts per million of dissolved hydrogen or presence of environments such as water, hydrogen, etc., are sufficient to greatly accelate the fatigue crack growth in ultrahigh strength steels. Although extensive work has been done in recent years to understand the effect of high temperature austenitization treatment with respect to hydrogen assisted cracking under static loading,[10-12] little work has been carried out to understand the role of microstructure coupled with internal hydrogen on the fatigue crack growth behavior of ultrahigh strength low alloy steels.

Further, an increase in fracture toughness alone is not necessarily sufficient to guarantee improved component reliability unless it is accompanied by an improved resistance to fatigue crack growth. Hence, the purpose of the present investigation was to evaluate the effects of high temperature austenitization treatments and internal hydrogen on fatigue crack growth behavior of AISI 4340 steel.

2. BACKGROUND

2.1 Microstructure

When plain carbon or alloy steels are quenched from the austenitizing temperature, they exhibit different martensite morphologies viz. plate or acicular and lath martensite depending upon composition and heat treatment. Increasing the carbon content or the amount of alloying elements in the steel favours the formation of plate martensite.[13,14] In low alloy steels, such as 4340 and 300-M, a decrease in the amount of plate martensite has been reported as the austenitization temperature was increased.[1,3] In general, the martensite needles are irrationally arranged in plate martensite; while in the lath martensite, bundles of martensite needles form almost parallel as packets. These parallel laths in a packet of martensite are predominantly separated by low angle boundaries, and in some isolated areas the adjacent laths are twin related. The lath martensite is extensively dislocated. However, internal twinning in the lath martensite has been occasionally observed.[15] On the other hand the plate martensite is predominantly twinned.

Several investigators have studied the effect of high temperature austenitization treatment on the microstructure of low alloy steels.[1,3-6] The findings of these investigations can be summarized as follows:

a) The high temperature austenitization treatment increases the prior austenite grain size.[1,6]

b) The high temperature austenitization treatment retards the second phase nucleation at the prior austenite grain boundaries upon subsequent quenching.[6]

c) The conventional austenitization treatment results in predominantly twinned plate martensite, while high temperature austenitization treatment gives dislocated lath martensite upon subsequent quenching.[1,3] However, Youngblood and Raghavan[4] reported that the amount of twinning in the martensite was independent of the austenitizing temperature (over the temperature range 870°C to 1200°C in 300-M steel).

d) It has been reported[1] that the high temperature austenitization treatment increases the amount of lath boundary retained austenite. Contrary to these observations, Youngblood and Raghavan[4] and McDarmaid[3] have reported that the amount of retained austenite in 300-M steel austenitized at 1200°C was about the same as that in the steel austenitized at 870°C.

e) The high temperature austenitization treatment reduces the segregation and partitioning of impurity and alloying elements at the prior austenite grain boundaries as well as on twin boundaries.[5,16]

Although extensive work has been carried out to establish the effect of high temperature austenitization treatment on the microstructure of these steels, little attention has been given to the following aspects:

a) The presence of retained austenite on the prior austenite grain boundaries.

b) The mechanical stability of retained austenite ahead of the crack tip, and during tensile deformation under plane stress and plane strain conditions.

c) The variation of carbide precipitation on twins as a function of austenitizing temperature.

Hence, in this investigation the major emphasis was given on the above aspects in addition to the identification of non-martensitic products at the prior austenite grain boundaries (if any) by transmission electron microscopy.

2.2 Fatigue Crack Propagation

Failure of structures in service due to cyclic loading involves crack initiation, crack propagation and final fracture. The crack initiation period is often absent in high strength materials because of pre-existing flaws such as cracks or inclusions. It is well established[17] that fracture mechanics provides the most useful and meaningful way of presenting fatigue crack propagation data since the loading, specimen geometry and crack size are all incorporated in a single parameter, the "stress intensity factor" K. Paris and Erdgon[18] have proposed an empirical equation relating stress intensity range, ΔK, ahead of a crack tip to crack growth rate per cycle, da/dN, i.e.,

$$da/dN = A\ (\Delta K)^{m} \qquad (1)$$

where A and m are material constants, "a" is crack length and N is number of cycles. Several investigators[19-21] have confirmed that for various materials the crack growth rate per cycle is controlled by the stress intensity range, ΔK, ahead of a crack tip as described in equation (1). Equation (1) is valid only in the intermediate crack growth rates, $10^{-6} < da/dN < 10^{-4}$ in/cycle. It underestimates crack growth rates at high stress intensity ranges where K_{max} approaches the fracture toughness of the material, and overestimates da/dN at very low stress intensity ranges as ΔK approaches the threshold stress intensity below which crack growth cannot be detected. Recent studies[22] have shown that a plot of the log da/dN vs log ΔK gives a signoidal curve which exhibits three stages as shown in figure 1. In region A, the threshold region, the crack growth is very sensitive to the stress intensity range. In region A the crack growth rate is also sensitive to the microstructure, the load ratio, $R = K_{min}/K_{max}$, the test environment, and the stress history. Region B exhibits linear crack growth. Unlike region A this region is insensitive to both microstructure and load ratio. A sharp increase in crack growth rate was observed in region C with increasing ΔK. In this region crack growth rates are very sensitive to both microstructure and load ratio. The effect of microstructure, load ratio, and environment on each region will be discussed in the following sections.

2.2.1 Effect of Microstructure on Fatigue Crack Growth. Microstructure is recognized as an important variable in fatigue crack growth.[23,25] Recently, the effect of microstructure on fatigue crack propagation has been discussed based on the fracture mode.[21,23,24] Fatigue fracture modes that are observed in high strength steels and other alloys are broadly classified into (i) the classical ductile striation mode and (ii) the static mode of fracture, viz. cleavage, intergranular and void coalescence. Microstructure plays an important role only in those regions where fatigue crack growth is associated with the static mode of failure.

For intermediate crack growth rates (region B) failure generally occurs in steels by a ductile striation mechanism.[8,9,25] Thus, in this region, there is little or no influence of microstructure on crack growth rates. The variation in microstructure of 300-M[9] and Fe-Cr-C[8] steels induced by changing the austenitization temperature has no affect on fatigue crack growth rate in this region, and crack growth occurs predominantly by a ductile striation mode. Furthermore, Ritchie[26] compared fatigue crack growth rates of temper embrittled and unembrittled 300-M steel, and demonstrated that the growth rates and mode of failure (striation mode) were the same for both cases. Ritchie,[26] and Begley and Toolin[27] have observed little influence of temper embrittlement on fatigue crack growth rates in 300-M and Ni-Cr-Mo-V steels. On the other hand, the presence of impurities in En 24 steel[28] and temper embrittlement in En 30 steel[29] have been reported to enhance crack growth rates approaching region C. This enhancement in growth rates was associated with the change in fracture mode (ductile striation to intergranular fracture mode).

At higher stress intensity ranges, the region C, fracture mode changes from ductile striation to static fracture modes, and growth rates become sensitive to microstructure. The fatigue crack growth rate in this region is partly controlled by the fracture toughness of the material which is known to depend on microstructure.[30,31] The distribution and size of second phase particles have been shown to affect crack growth rates in steels and Al alloys.[32,33] Heald et al[33] have compared fatigue crack growth rates between spheroidized, mixed spheroidized/pearlitic, and coarse pearlitic structures in a 1.0 percent C steel. The lowest crack growth rates were observed for the spheroidized condition. Further the amount and coarseness of pearlite was increased, the growth rates increased.

Unlike region B, region A crack growth rates and the threshold stress intensity are sensitive to microstructure and mechanical properties.[8,9,25,34-36] It is not possible to separate the effect of microstructure and mechanical properties on crack growth, since mechanical properties are controlled by microstructure. It is well known from the Hall-Petch relation that the grain size has a strong influence on mechanical properties. Further, mechanical properties, including yield stress, are strongly dependent on size, shape and distribution of second phase particles. Klensil et al[37] have studied the effect of grain size on the endurance limit of low carbon steel and proposed an equation similar to the Hall-Petch relation.

The threshold stress intensity is generally reduced as the yield strength of the material is increased.[23,25,34] The effect of carbide size in a low alloy steel on threshold stress intensity and crack growth rates at low stress intensity ranges was studied by Benson.[34] As the carbide particle size increased, the yield strength decreased, and an increase in threshold stress intensity was observed.[34]

Several investigators have studied the effect of grain size on the threshold stress intensity and on crack growth rates at low stress intensity ranges in high strength steels,[8,9] mild steels,[35] and Ti alloys.[25] It has been shown[35] that as the grain size of mild steel is increased, the threshold stress intensity significantly increases. In 300-M steel, increasing the prior austenite grain size from 25 μm to 250 μm decreases the crack growth rates at low stress intensity ranges without affecting the threshold.[9] Contrary to this, in Fe-4% Cr-0.3% C[8] increasing the prior austenite grain size increases the crack growth rates near threshold stress intensity. A cyclic softening steel (300-M) produced a slight increase in threshold when the prior austenite grain size was increased,[9] whereas in a cyclic hardening steel a slight decrease in the threshold stress intensity has been observed.[8] In type 316 stainless steel[36] and also Ti alloys[25], increasing grain size resulted in an increase in threshold.

Various mechanisms have been proposed to explain the effect of grain size on the threshold behavior.[9,25,35,36] Masounave and Bailon[35] have argued that deviation of the crack in coarse grained ferrite resulted in an effective reduction in macroscopic fatigue crack growth rate. Priddle[36] also considered that an increase in grain size from 50 μm to 350 μm would lower the effective stress intensity at the crack tip because of crack tip deviation in the coarse grained structures. Ritchie[9] and others[25,34,38] attribute grain size effect on threshold behavior to the environment. It is argued[9,34-38] that moisture in the air decomposes into atomic hydrogen and oxygen at the crack tip and the stress gradient ahead of a crack tip drives hydrogen into the metal lattice where it accumulates in the region of maximum hydrostatic tension which results in the reduction of cohesive strength. The diffusion of hydrogen to the grain boundaries, ahead of a crack tip, weakens grain boundaries relative to the grain interiors. The effect of prior austenite grain size on fatigue crack growth in high strength steels at low stress intensity ranges is not well understood. However, Ritchie[9] has rationalized the observed lower crack growth rates in coarser grained steel in terms of diffusion of hydrogen atoms to the grain boundaries through the plastic zone by a dislocation "sweep-in" mechanism. He argued that in coarser grained structures the plastic zone size remains small compared to the grain diameter until much higher stress intensities, which results in a reduced environmental influence.

2.2.2 Effect of Load Ratio on Fatigue Crack Growth.

The influence of load ratio, $R = K_{min}/K_{max}$, on the shape of the fatigue crack growth curve is shown in figure 1. It is clear that the load ratio affects the low and high crack growth rates (regions A and C), while intermediate crack growth rates are almost insensitive to load ratio.

The load ratio has been reported to have little influence on fatigue crack growth rate in the intermediate region of 4340, 300-M, 4140, Fe-Cr-C and En 30 steels.[8,9,31,38,39] In this region the crack growth for all load ratios is found to be predominantly by a ductile striation mechanism.

The models of fatigue crack growth are based on the concept of one striation growth increment per cycle, and such models also predict little or no influence of load ratio on crack growth rates. Whenever the mechanism of crack growth is by ductile striation, crack growth rate is controlled by the amount of crack opening per cycle, and is dependent only upon elastic modulus.[30]

As the load ratio is increased, K_{max} increases for a given ΔK, $K_{max} = \Delta K/(1-R)$. Crack growth by the ductile striation mechanism is primarily controlled by ΔK and hence, in the intermediate crack growth region where the mechanism of crack growth is by ductile striation, crack growth is independent of load ratio.

On the other hand, static mode of failures are controlled by K_{max} and thus, at high crack growth rates where the crack growth is associated with static mode of failure, the load ratio plays an important role on fatigue crack growth. Crack growth rates increase with load ratio. Carlson and Ritchie[8] and Ritchie[9] have demonstrated this effect of load ratio on fatigue crack growth rates in Fe-Cr-C and 300-M steels. The presence of static mode of failures was also confirmed in these steels.[8,9]

As the load ratio is increased, the threshold stress intensity decreases in several alloys tested in air.[8,25,38] The threshold stress intensity has been found to be insensitive to load ratio when they are tested in vacuum.[25,38,39] Furthermore, several investigators have observed corrosion products on the fracture surfaces of steel specimens tested in air.[34,39-41] In region A, both intergranular and transgranular fracture modes have been observed in high strength steels.[25,39-41] The occurrence of intergranular fracture in region A, contrary to region C, is controlled by both ΔK and K_{max}.[39-41] The intergranular fracture mode was absent in specimens tested in vacuum.[25,38,39] Based on these observations, several investigators[8,9,25,34,38-41] have attributed the effect of the load ratio on this region to environmental effects. As the load ratio is increased, K_{max} increases for a given ΔK and thus the stress gradient ahead of a crack tip increases, leading to greater hydrogen transport. This causes grain boundary weakening and, hence, to an increase in growth rates and a decrease in threshold stress intensity.

Another interpretation of influence of load ratio on fatigue crack growth rates near threshold has been proposed,[43] and is based on the concept of crack closure. The concept of crack closure relies on plastic deformation ahead of a crack tip to introduce residual stresses, which cause closure of the crack surfaces during the unloading cycle. Since the crack is unable to propagate while it remains closed, the net effect of closure is to reduce the applied ΔK value to a lower effective value (ΔK_{eff}) actually experienced at the crack tip. As the load ratio is increased, the crack is assumed to remain open for a larger portion of the cycle, thus increasing the value of ΔK_{eff} and hence the growth rate.

However, Ritchie[30] and others[44] pointed out that the crack closure arguments do not account for the fact that the fatigue crack growth rates of steels in region B are almost insensitive to load ratio, where crack closure is equally likely to occur. The explanations for the effect of load ratio on fatigue crack growth rates near threshold remains uncertain. However, several investigators[9,25,34,39,41] have shown that the nature of environment plays a major role on crack growth in this region.

2.2.3 Effect of Environment on Fatigue Crack Growth.

The pioneer work on the influence of environment on fatigue was carried out by Haigh[45] and by Gough and Sopwith.[46] It has been found[45,46] that the fatigue lives of most structural alloys are significantly reduced by the presence of air (versus vacuum). Further, the fatigue crack growth rates were also found to be affected by the test environment.[38,39] These investigators compared the crack growth rates of En 24 and 4340 steels tested in vacuum and air and demonstrated that the growth rates near the threshold region in air were slightly higher than in vacuum. At higher ΔK, crack growth rates in air and vacuum were almost the same. Dahlberg[47] and Spitzig and Wei[48] showed that wet environments can have a significant effect on crack growth rates of ultrahigh strength steels. Although, they have not considered the effect of wet environment on the three stages of fatigue crack growth, they reported that the moisture in the environment enhanced crack growth rates.

Several investigators[49-58] have classified the effect of corrosive environment on fatigue crack growth behavior based on the threshold stress intensity, K_{1scc}, of the material under sustained loading. Stress corrosion cracking is the subcritical crack growth under the combined action of static stress and a corrosive environment. In this case the crack growth is represented as log da/dt vs log K. The salient features of stress corrosion cracking are the existence of three stages viz. region i where the crack growth rate increases sharply with stress intensity, region ii where the crack growth rate is independent of stress intensity and region iii where the crack growth rate again sharply increases with stress intensity as fracture toughness of the material is approached (Figure 2). The K_{1scc} in figure 2 represents the threshold stress intensity below which stress corrosion cracking does not occur.

Environment enhanced fatigue crack growth of high strength materials has been characterized[49,50,55-57] in terms of three general patterns of behavior, based on K_{1scc}, as illustrated in figure 3. Figure 3(a) represents the true corrosion fatigue behavior where fatigue crack growth rates are enhanced and the threshold stress intensity range for crack growth is reduced by the presence of an aggressive environment from the synergistic action of corrosion and cyclic loading. This type of behavior has been observed in AF1410,[59] Ni-Cr-Mo,[53,54]Ni-Cr-Co-Mo[53,54] and HY 80[52] steels which do not stress corrode under sustained loading until much higher stress intensities (i.e., $K_{1scc} = K_{1c}$). In stress corrosion fatigue, figure 3(b), the crack growth rates are enhanced when the maximum stress intensity, K_{max}, is greater than K_{1scc} and environmental effects on crack growth are negligible when $K_{max} < K_{1scc}$. Figure 3(c) exhibits both true and stress corrosion fatigue. A broad range of material-environmental systems exhibit this behavior.

Several similarities, in subcritical crack growth in the aggressive environments, under sustained loading and cyclic loading have been observed.[60-65] Some of the similarities are as follows:

(a) The acceleration of fatigue crack growth in the hydrogen environment of steels[60] and Ni alloys[61] has been reported to be maximum at about room temperature. The percentage of intergranular fracture was also found to be maximum in the specimens tested at this temperature.[60] Similar observations have been made in hydrogen assisted cracking of steels under sustained loading.[62,63]

(b) The addition of oxygen to the hydrogen environment reduced the crack growth rates both in sustained loading and cyclic loading.[60,64] And

(c) The mode of fracture has been reported to be identical in high strength steels under both sustained loading and cyclic loading.[65]

Based on the similarities between corrosion fatigue and stress corrosion cracking, earlier investigators[49-51,55-57] have suggested that the mechanism of hydrogen embrittlement is the same for true corrosion fatigue, stress corrosion fatigue and stress corrosion cracking.

Two models were proposed by Wei and Landes[65] and Austen and Walker[56,57] for making a quantitative estimation of the effects of an aggressive environment on fatigue crack growth. In the superposition model, proposed by Wei and Landes,[65] the rate of fatigue crack growth in the aggressive environment is considered to be the algebraic sum of two components: one representing the crack growth rate in the inert environment (da/dN)v and the other an environmental component which is computed from sustained load crack growth data. That is

$$(da/dN)_{env} = (da/dN)_{vacuum} + \frac{(da/dt)}{\text{Frequency}} \qquad (2)$$

This model has been verified in several material-environmental systems including 18Ni (250 grade) maraging steel tested in dehumidified hydrogen and in medium carbon low alloy high strength steels tested in distilled water and in dehumidified gaseous environments.[65] Gerberich et al.[66] and Bucci[67] also showed that for high strength steels, Al alloys and Ti alloys tested in distilled water and in 3.5% NaCl solution, the superposition model correctly predicts stress corrosion fatigue crack growth behavior.

The process competition model, proposed by Austen and Walker,[56,57] considers that fatigue and stress corrosion crack growth processes are mutually competitive (but not additive) and the crack will grow at the fastest available rate for a given stress intensity.

These two models only account for stress corrosion fatigue, however, and to date, no model has been developed to account for true corrosion fatigue behavior.

Summarizing, the microstructure and the load ratio play an important role on fatigue crack growth rates only at low and high stress intensity ranges. Further, the presence of an aggressive environment enhances the fatigue crack growth rates. The fatigue crack growth behavior of conventionally heat treated ultrahigh strength low alloy steels has been well studied. However, little work has been done[8,9] to establish the role of high temperature austenitization treatment on fatigue crack growth characteristics.

Extensive amounts of work have been done relative to the effect of microstructure per se and the corrosive environment per se on fatigue crack growth behavior of high strength steels. However, the cumulative effects of these parameters, for instance, the role of prior austenite grain size upon the true and stress corrosion fatigue behaviors has not received adequate attention.

Hence, in this investigation an attempt has been made to understand the role of microstructure coupled with internal hydrogen on fatigue crack growth behavior of ultrahigh strength steels.

3. EXPERIMENTAL PROCEDURE

3.1 Material Preparation

The material used in this investigation was commercial aircraft quality AISI 4340 steel. The steel was received as 0.75 in (18mm) thick hot rolled plates in a fully annealed condition, and the chemical composition of this steel is given in table I. Compact tension specimens, in accordance with ASTM specifications E-399-72, were machined from the plate in L-T orientation and their dimensions are shown in figure 4. These specimens were used for fatigue crack growth studies. Tensile plate specimens were also machined in order to study the mechanical stability of retained austenite by magnetic saturation analysis and by transmission electron microscopy. The dimensions of these specimens are shown in figures 5 and 6.

3.2 Heat Treatment

The various austenitizing temperatures and two tempering temperatures were chosen in this investigation in order to vary the microstructural variables including the prior austenite grain size, retained austenite, type of carbides, etc. The various heat treatments used in this investigation are listed in table II.

All austenitizing treatments were carried out in a vertical tube furnace under a controlled atmosphere and the furnace temperature was maintained within ±5°C. The austenitization treatment was done for 1 hr. at either 870°C, 1100°C, or 1200°C followed by quenching in agitated oil.

For the step quenching treatments, the specimens were initially austenitized at 1200°C for 1 hr. in a tube furnace and then they were transferred to a 870°C neutral salt bath furnace for half an hour prior to oil quenching. The tempering treatments were carried out in a neutral salt bath for 1 hr. either at 180°C or 280°C.

3.3 Hydrogen Charging

Following the heat treatment, all specimens were mechanically polished to remove any decarburised layer from the surface. To study the effect of internal hydrogen on fatigue crack growth behavior, the specimens were cathodically charged in an electrolyte containing 4% sulfuric acid and phosphorous as a poison. Ten cc of 5% solution of phosphorous in carbon disulphide were added to 600 cc of electrolyte. Each specimen was charged in a fresh bath for 24 hours at a current density of 0.005 amp/cm^2. Immediately after charging, the specimens were ground on all surfaces using 120 grit emery paper and ultrasonically cleaned for 10 mts. in a 10% hydrochloric acid solution. The specimens were then rinsed thoroughly and cadmium plated in a cyanide bath consisting of 28 grams/liter of CdO and 105 grams/liter of NaCN containing commercial brightener. The pH of the solution was maintained to 13 by the addition of NaOH. A current density of 0.02 amp/cm^2 was employed for cadmium plating. The purpose of cadmium plating was to trap charged hydrogen within the specimen.

3.4 Fatigue Crack Growth Testing

Compact tension specimens were used for the fatigue crack growth studies. Prior to crack growth testing, a 0.008 in (0.02 cm) thick slot was machined in order to act as a notch for introducing fatigue precrack. A 22,500 lbs. (≈10,200 Kg.) capacity servo controlled instron system was used for fatigue precracking and crack growth testing. A fatigue precrack of at least 0.12 cm (0.05 in) long was introduced and precracking was done at a stress intensity range of $\Delta K = 25$ Ksi$\sqrt{in}$ (≈27.5 MPa$\sqrt{m}$). After the fatigue precrack was initiated, the precracking load was reduced in stages to minimize residual stress effects, prior to final crack growth testing at low stress intensity ranges ($\Delta K < 25$ Ksi$\sqrt{in}$). At each stage the crack was allowed to grow through the plastic zone associated with previously applied ΔK. Crack growth tests were conducted under sinusoidal tension-tension with a load control, at a load ratio of 0.25 and testing frequency was 10 Hz. The tests were conducted in ambient air. The crack length was monitored using COD gauge on X-Y recorder and number of cycles were recorded. The crack length measurements were taken, at every load level, over increments of crack growth about 1.0 mm (0.04 in). The actual crack length was determined from the crack opening displacement vs crack length calibration curve (figure 7). All crack growth tests were conducted under plane strain conditions.

3.5 Fatigue Crack Growth Analysis

The crack length vs number of cycles data was fitted to a polynomial of degree 2, 3, and 4. When this data was fitted to a polynomial of degree greater than or equal to 3, the resulting curve had inflections and thus gave negative crack growth rates, da/dN. Although curve fitting to a polynomial of degree 2 gave a smooth curve in a majority of the cases, occasionally inflections were observed. Similar results were reported by Davies et al.[68] Since the negative crack growth rates are physically impossible, it was decided to fit the data to a 8-point incremental-step orthogonal polynomial.[8,9] The construction of orthogonal polynomial and regression analysis has been described in reference 69. Use of this regression analysis eliminated the inflections and the merits of this analysis has been discussed by Ritchie.[70] The first eight a vs N points (i.e., points 1 to 8) were fitted to a second order orthogonal polynomial. The polynomial was then differentiated at the middle two points (i.e., points 4 and 5) and da/dN recorded for these two values of crack length. The program then moved forward two points while dropping first two points and a new polynomial was fitted between these data points (i.e., points 3 to 10). The da/dN was again calculated at the middle two points (i.e., points 6 and 7) and this procedure repeated until all the points had been analysed.

The stress intensity range, ΔK, at these crack lengths, was calculated using the following equation developed by Brown and Srawley[71] and then log da/dN vs log ΔK was plotted.

$$\Delta K = (\Delta P/BW)\ 29.6(a/W) - 185.5(a/W) + 655.7(a/W)$$
$$- 1017(a/W) + 638.9(a/W) \qquad (3)$$

Where $\Delta P = P_{max} - P_{min}$; B = the specimen thickness; W = the specimen width; and a = crack length.

3.6 Microscopy

3.6.1 Optical Metallography. Small sections were cut from the mid thickness of compact tension specimens for optical metallography. These specimens were successively ground from 120 to 600 grit, and then polished using 0.3 μm alumina powder. All specimens were etched with 4% picral, 2% nital and a few drops of zephyron chloride solution. These specimens were observed in Carl-Zeiss optical microscope.

3.6.2 Transmission Electron Microscopy. Thin foils for transmission electron microscopy were taken from the fractured compact tension specimens. Sections of about 0.02 in (0.5 mm) thick were cut with the specimen flooded with coolant to avoid heating. These sections were mechanically polished to reduce thickness to 0.005 in (0.13 mm) prior to electropolishing to 0.002 in (0.05 mm) thickness. Discs of 3.0 mm dia. were punched from these slices. These discs were polished using a Fishione double jet polishing unit. A solution of 100 grams of chromic trioxide, 540 cc of glacial acetic acid and 28 cc of distilled water was used as electrolyte for both stages of electro-polishing. A voltage of 35 V for the initial polishing and 55 V for the double jet polishing was employed at a current density of 0.1 to 0.2 amp/cm^2. The temperature of the solution was maintained below 15°C during polishing.

To study the mechanical stability of retained austenite in front of a crack tip, under monotonic and cyclic loading, sections were cut perpendicular to the crack growth direction as shown in figure 8 (the K_{1c} test was interrupted as soon as P_{max} was reached and the fatigue test was stopped at $a/W = 0.58$). The schematic of the plastic zone ahead of the crack tip is also shown in figure 8. In order to include the plastic zone within the foil, these sections were carefully polished from both sides in such a way that part of the crack front was seen on both sides of the foil as shown in figure 9(a). Discs were punched across the crack front and then jet polished. These discs after jet polishing were examined in scanning electron microscope (figure 9(b)), to make sure that the plastic zone was included in the foils. The region marked "A" in figure 9(b) was part of the plastic zone.

Thin foils for transmission electron microscope, to study the effect of deformation under plane stress and plane strain conditions on the mechanical stability of retailed austenite, were taken from the surface and from the cross section of broken tensile plate specimen as shown in figure 6.

All these foils were observed in a Hitachi HU 11B electron microscope at an operating voltage 100 or 125 KV.

3.6.3 Scanning Electron Microscopy. Scanning electron microscopy was carried out using a JEOL (JSM-35) scanning electron microscope at a secondary operating voltage of 25 KV. In order to preserve the fracture surfaces from the oxidation, the fracture surfaces were coated with "Den Kote" spray. The specimens were ultrasonically cleaned in acetone and petroleum ether prior to the examination.

3.7 Magnetic Saturation Analysis

The magnetic saturation technique was used to determine the amount of retained austenite as a function of austenitizing temperature and deformation to supplement transmission electron microscope results. The heat treated specimens, figure 5, were sent to the University of California at Berkeley for testing. The detailed procedure of this technique is described in reference 72. With this system it is possible to measure magnetic flux changes in the specimen, which depends upon the magnetic phase (martensite) present.

3.8 Hydrogen Analysis

Following the crack growth testing, coupons of about 1 gram were cut from the hydrogen charged compact tension specimens. These coupons were stored in liquid nitrogen to prevent hydrogen outgassing until the coupons were analyzed. These coupons were analyzed for hydrogen content using the ultrasensitive hydrogen detector developed by Das.[75] This system works on the principle of selective permiation of hydrogen through a semipermeable metallic membrane. This system can detect hydrogen concentrations of a few parts per billion. Details of operating procedure and accuracy of the instrument are described elsewhere.[75]

4. RESULTS

4.1 Microstructural Characterization

4.1.1 Optical Metallography. The prior austenite grain size and general microstructure of as quenched specimens austenitized at different temperatures were observed by optical metallography. The variation of prior austenite grain size for different austenitization treatments used in this investigation was determined from optical micrographs and are shown in table III and figure 10. It is evident from figure 10 and table III that large differences in prior austenite grain size were achieved by these treatments. A dark etching constituent at the prior austenite grain boundaries is shown in figure 11(a) and (b). Similar observations have been made by Wood[6] and he has concluded that these dark etching constituent could be non-martensitic products, such as upper bainite or lower bainite. Since auto tempered martensite also etches dark, it is very difficult to characterize this micro constituent through light microscopy. Extensive transmission electron microscopy was employed in this investigation to characterize and identify the dark etching constituent and other microstructural details like substructure of martensite, retained austenite and type of carbides, etc. Transmission electron microscope studies were carried out only for the specimens austenitized at different temperatures and quenched and tempered either at 180°C or 280°C.

4.2 Transmission Electron Microscopy

4.2.1 General Microstructure. Transmission electron microscopy studies revealed that all austenitization treatments resulted in mixed microstructures consisting of plate martensite and packets of parallel laths. The amount of plate martensite decreased with increasing austenitization temperature. Lath martensite was predominant in specimens austenitized either at 1200°C or in step quenched cases. In the fine grain structures, the regions of plate martensite and lath martensite are shown in figure 12. Martensitic plates or laths often extended across the whole grain and this was not observed in the coarse grain structures. These results are in agreement with the earlier reports.[1,3] The plate martensite in specimens austenitized at 870°C consisted of a mixture of dislocated plates and twinned plates (marked A and T in figure 12 (d)). Similar results were reported by Lai et al.[1] They have also reported that the plate martensite obtained from higher austenitization treatments was dislocated but not twinned. Occasionally twinned plate martensite was observed in the specimens austenitized at higher temperatures.

The substructure of lath martensite was very similar for all austenitizing treatments. The laths were predominantly dislocated, however, internal twinning in a few isolated laths was also observed. Internal twinning in some individual laths has also been shown by previous investigators for plain carbon and alloy steels.[13-15,74] In general, laths were separated by low angle boundaries, although, in some regions, twin-related laths were also occasionally observed (figure 13). In concurrence with the observations of other investigators,[75] these laths of martensite are predominantly in juxtaposition to $\langle 100 \rangle_M \parallel$ and $\langle 111 \rangle_M$ orientations.

Careful analysis of lath martensite structures indicated the presence of at least three different types of lath morphologies viz. convergent laths, regular parallel laths and large laths containing extensive carbides, similar to the observations of Law et al[74] and Chilton et al[76] in low alloy and plain carbon steels. Convergent laths, figure 14(a), were most frequently observed. The laths appear to merge together with curved boundaries. The lath marked "A" to have developed at an angle to other laths around it in the packet. A regular parallel lath structure was occasionally observed within each martensite packet, with individual laths having planar boundaries, figure 14(b). Finally, large laths containing extensive carbides were observed, figure 14(c). These large laths were most probably formed in the early stages of transformation. By dark field imaging, Law et al[74] have concluded that these variations in morphology of lath martensite are not due to sectioning effects.

4.2.2 Variation of Twinning. Extensive twinning was observed in the specimens austenitized at 870°C or 1100°C prior to quenching. Direct quench from 1200°C resulted in samples relatively free from twinning. The difference in microstructures between direct quenched and step quenched from 1200°C treatments was that the latter treatment resulted in more twinning.

The amount of twinning appeared to decrease as the austenitization temperature was increased. This observation is contrary to the observation made by Carlson et al[77] for Fe-4.0% Cr-0.3% C steel. They have reported that the probability of observing twinning increased with increasing austenitizing temperature. This has been attributed[77] to the enrichment of carbon in the austenite due to the dissolution of more carbides during the high temperature austenitization treatment. If this is the case, the high temperature austenitization treatment should lower the Ms temperature. Contrary to this, an increase in Ms temperature in 4340 steel has been reported[1] for the coarse grained structures. Parker[78] ruled out the possibility of any undissolved carbides in 4340 and 4330 steels quenched after austenitizing at 870°C. Furthermore, no undissolved carbides were detected by transmission electron microscopy in the present investigation even in the specimens austenitized at 870°C.

It has been reported[14] that higher austenitization treatments tend to reduce segregation and partitioning of impurity and alloying elements in the austenite. Ogura et at,[14] by selective etching, have shown the segregation of carbon, phosphorous, sulfur, chromium, etc., at the twin and prior austenite grain boundaries and concluded that segregation decreases with increasing solution treatment temperature. In other words, higher austenitization results in a more homogeneous austenite. Recently, Khan and Wood[79] have shown an increased amount of twinning in step quenched 4340 steel with decreasing intermediate holding temperatures or increasing holding times at these temperatures. This was explained on the basis of local variation of impurity and alloying elements in the austenite. Local variation of impurity and alloying elements may change the stacking fault energy in those regions which have been shown to affect the amount of twinning in the martensite.[80,81] The observed decrease in twinning with increasing austenitization temperatures is consistent with segregation effects during the austenitizing treatment.

4.2.3 Martensite Morphology at Prior Austenite Grain Boundaries.

In a majority of the cases, the martensitic structure extends to the prior austenite grain boundaries, figure 12, suggesting that non-martensitic products were not present at these grain boundaries. Large, irregular shaped laths were occasionally observed at prior austenite grain boundaries, irrespective of grain size, as shown in figure 15. Extensive carbide precipitation within these laths is also evident in figures 15 (a) to (d). Figure 16(a) shows an irregular shaped lath in a specimen austenitized at 1200°C and tempered at 280°C. It is seen that this lath is heavily dislocated. Dark field image using cementite spot reversed the contrast of cementite as shown in figure 16(b). It is clear from figure 16(b) that cementite precipitated in more than one orientation. Cementite at the prior austenite grain boundary can also be seen. The same dark field image at low magnification, figure 16(d), shows distribution of cementite within the irregular lath and at its boundary. The carbides were found to be about 60 to 200Å in width and 200 to 1500Å in length.

On the other hand, both dislocated and twinned irregular shaped laths at prior austenite grain boundaries were observed in step quenched specimen as shown in figures 15 (b) and (c) and 17. The dark field image using a (110) type twin spot confirmed the presence of twins as shown in figure 17(b).

Figure 18 is a transmission electron micrograph of a specimen austenitized at 870°C and tempered at 180°C, showing prior austenite grain boundaries. It is clearly seen in figure 18(a) that some martensite plates adjacent to the prior austenite grain boundaries were internally twinned. Dark field analysis using a twin spot confirmed the presence of twins as shown in figures 18(b) and (c).

Further, Huang and Thomas[82] have reported that the substructure of upper or lower bainite contains dislocated laths. They also observed about 4000Å long carbide needles in low alloy steel isothermally transformed at 275°C.

All the above observations viz. the extension of martensite plates or laths to the prior austenite grain boundaries, the presence of twins in martensite plates or laths adjacent to the prior austenite grain boundaries, and fine carbide needles (200 to 1500 Å in length) in more than one orientation within the irregular shaped lath at grain boundaries, suggest that non-martensitic products were not present at the prior austenite grain boundaries.

Kamada et al[83] have observed heavily dislocated irregular shaped laths in Fe-5% Ni-2% C steel and they called it blocky martensite. They have also pointed out that blocky martensite tends to exist alone unlike parallel laths. The presence of blocky martensite has been reported in step quenched 4340 steel[84] at the prior austenite grain boundaries and internal twinning within the blocky martensite has been observed.

Hence, it was concluded that the dark etching constituent observed in optical micrographs is auto tempered blocky martensite.

4.2.4 Variation of Retained Austenite.

Thin films of retained austenite were observed in quenched tempered (at 180°C) specimens, at the lath, packet and prior austenite grain boundaries regardless of austenitizing temperature. A slight increase in the amount of retained austenite at the lath and grain boundaries was observed with increasing austenitization temperature.

By means of dark field imaging, using (002) retained austenite spot, the morphology of retained austenite at lath boundaries austenitized at 870°C, 1200°C, and step quenched specimens is shown in figures 19 and 20. Comparing these figures, it is clear that the direct quench from 1200°C or step quench treatment results in slightly higher amount of lath boundary retained austenite than the 870°C treatment (estimated ≈ 5% versus 3%). The step quenching treatment does not affect the amount of retained austenite between laths. The retained austenite films in fine grained (870°C) structures were not continuous around the martensite laths while in coarse grained (direct 1200°C or step quench) structures, almost continuous films of retained austenite were observed. The thickness of these films ranged from 100Å to 400Å. Thin films of retained austenite were also observed at the boundaries of convergent, regular and large laths. These results are consistent with the observations made in Fe-V-C steel.[74]

Analysis of SAD pattern, as illustrated in figure 19(c) (see figure 22), revealed that the orientation relationship between the austenite and martensite was the Kurdjumov-Sachs (K-S) relationship; i.e., $\langle 011\rangle_M \parallel \langle 111\rangle_A$, $\langle 111\rangle_M \parallel \langle 110\rangle_A$. In addition to the K-S relationship, the Nishiama-Wesserman (N-W) relationship was also occasionally observed, figure 21.

Thomas and Rao[85] have observed both K-S and N-W orientation relationships in the same packet of martensite. Recently Rao[86] has found that both K-S and N-W orientation relationships were alternating within the same packet and N-W relationship predominated upon the addition of 2% Mn or 5% Ni to Fe-3% C-4% Cr steel.

4.2.5 Variation of Retained Austenite at Prior Austenite Grain Boundaries. The presence of retained austenite at prior austenite grain boundaries plays an important role in tempered martensite embrittlement and hydrogen assisted cracking since the retained austenite decomposes into cementite upon subsequent tempering and thus contributes embrittling carbides on grain boundaries which weakens the grain boundaries. The variation of retained austenite at prior austenite grain boundaries as a function of austenitization temperature is shown in figures 22 and 23.

A bright field image obtained in a specimen austenitized at 870°C is shown in figure 22(a) and SAD pattern obtained from figure 22(a) is shown in figure 22(c). The dark field image using a (002) retained austenite spot reversed the contrast of retained austenite as shown in figure 22(b). It is clear, from the figure 22(b), that very little retained austenite was present along the prior austenite grain boundaries in fine grained structures. Dark field analysis on both sides of grain boundaries was also carried out and a trace amount of retained austenite was observed along the prior austenite grain boundaries.

Significant amounts of retained austenite films were observed in the coarse grained structures (both direct quench from 1200°C and step quenched specimens), along the prior austenite grain boundaries in addition to interlath films of retained austenite as shown in figures 23(b) and 23(d). It is interesting to note that the amount of retained austenite at the prior austenite grain boundaries also was not affected by the step quenching treatment after initial austenitizing at 1200°C. The amount of retained austenite at prior austenite grain boundaries also increased with increasing austenitizing temperature.

4.2.6 Mechanical Stability of Retained Austenite.

The mechanical stability of retained austenite has been studied in specimens austenitized at 1200°C prior to quenching and tempering at 180°C. The retained austenite is found to be mechanically unstable in front of a crack tip (loaded monotonically or cyclically to the load corresponding to K_{1c}) or deformed under plane stress or plane strain conditions. In deformed specimens two situations were encountered, viz.

a) regions having small amounts of discontinuous films of retained austenite between laths, and

b) regions having no lath boundary retained austenite, although in both the cases the laths were in juxtaposition to $\langle 100 \rangle_M \,/\!/\, \langle 111 \rangle_M$ orientations.

Figures 24(a) and 24(d) are bright field micrographs obtained from two different areas. The selected area diffraction patterns obtained from these areas revealed the presence of spots belonging to $[100]_M$ and $[111]_M$ zone axes and $[110]_A$ austenite zone axis (figure 24(c)). Dark field image using a (002) austenite spot confirmed the presence of a very small amount of discontinuous films of retained austenite between laths (figures 24(b) and 24(e)).

Figures 25(a) and (b) show typical regions of lath martensite with no retained austenite between laths. The SAD pattern obtained from figure 25(a) is shown in figure 25(c). Analysis of SAD patterns, as illustrated in figure 25(d), indicate the existence of only martensite spots belonging to $[100]_M$ and $[111]_M$ zones. The absence of extra spots due to retained austenite confirmed that retained austenite present at the lath boundaries prior to deformation transformed into martensite. Because retained austenite films prior to deformation are 400Å or less in thickness, it was difficult to carry out an analysis in these regions to determine whether the retained austenite transformed into dislocated and/or twinned martensite upon deformation.

The variation of retained austenite within a given undeformed specimen was recently explained by Sarikaya et al[87] based on adjacent lath orientations. They argued that the twin related laths have self accommodating strains (associated with martensitic transformation) and retained austenite should not be present between these laths. Contrary to these observations Law et al[74] have shown the presence of interlath films of retained austenite between twin related laths. The parallel laths of martensite obtained from deformed specimens, shown in figures 24 and 25, are twin related. Furthermore, the presence of discontinuous films of retained austenite, in deformed samples, in between laths (figure 24), suggests that the retained austenite transforms to martensite upon deformation. The variation of retained austenite, figures 24 and 25, in deformed specimens may be associated with inhomogeneous deformation (from grain to grain) of polycrystalline specimens. In polycrystalline specimens, some grains are more favorably oriented for slip than the others. The grains which are suitably oriented for slip deform more than the grains which are less favorably oriented for slip. The retained austenite transformation to martensite depends on percentage of deformation, it is possible to observe some retained austenite in the grains which are less favorably oriented for deformation.

Although the stability of retained austenite depends on composition, Law et al[74] and Syn et al[88] have reported that the retained austenite in Fe-1% V-25% C and Fe-9% Ni-1% C steels is mechanically unstable. Further, Syn et al[88] have demonstrated that the retained austenite transforms to dislocated martensite. These results support the results of the present investigation.

4.2.7 Mode of Deformation. The mode of deformation under plane strain and plane stress condition was investigated in the specimens austenitized at 1200°C and tempered at 180°C. The mode of deformation in plane strain and plane stress conditions was found to be different.

The microstructure deformed under plane strain conditions exhibited a substructure with extensive dislocation networks and/or extensive twinning. A typical extensive twinned region is shown in figures 26 and 27 (a) and (b). On the other hand, only extensive dislocation networks were observed in the specimens deformed under plane stress conditions (figures 27 (c) and (d)). The relative absence of twins in undeformed specimens and presence of extensive twinning in deformed specimens under plane strain condition suggests that these are deformation twins and not transformation twins. (Direct classification of deformation and transformation twins, in these systems, by transmission electron microscope is difficult). These results suggest that lath martensite deformed by twinning under plane strain conditions, whereas under plane stress it deformed by slip.

Investigations by Magee and Davies[89] on the mode of deformation of lath and plate martensite have shown that the mode of deformation depended not only on the morphology and substructure of martensite but also on the carbon content. They demonstrated that plate martensite deformed by twinning when the carbon content exceeded 0.3 wt. %, while lath martensite deformed by slip up to 0.54% C under plane stress conditions. They also pointed out that in mixed microstructures (consisting of both twinned plate martensite and dislocated lath martensite) when the carbon content is equal or greater than 0.4 wt.%, plate martensite deformed by twinning and lath martensite deformed by slip.

Although the high temperature austenitization treatment resulted in predominantly laths and a few plates of martensite in 4340 steel, Zackay et al[90] reported that this plate martensite was dislocated.[1]

The difference in deformation under plane strain and plane stress conditions is the existence of a triaxial state of stresses in the former case which is absent in plane stress condition. It has been established[91] that the presence of triaxial state of stresses favors mode of deformation by twinning.

4.2.8 Structure of Tempered Martensite.

In plain carbon and alloy steels the various stages of tempering involve:

1. segregation of carbon atoms to lattice defects,
2. precipitation of iron carbides,
3. the decomposition of retained austenite,
4. precipitation of alloy carbides (in alloy steels) and
5. recovery and recrystallization.

Speich and Leslie[92] and Honeycombe[93] published excellent reviews on this topic. In this investigation two tempering temperatures were employed viz. 180°C and 280°C.

(a) 180°C Tempered Structure--The structures of the specimens tempered at 180°C were similar to those of as quenched specimens, as reported by Lai et al,[1] except in the amount of carbides. Tempering at 180°C for 1 hr. resulted in a microstructure consisting of both epsilon carbide and cementite. Varying the austenitizing temperature did not produce a significant difference in the type or amount of carbides. Figure 29 shows an example of extensive epsilon carbide precipitation inside the lath martensite. The selected area diffraction pattern obtained from figure 28(a) is shown in figure 28(c). The diffraction pattern consists of $[100]_M$ ferrite zone and $[11\bar{2}0]_E$ carbide zone. The orientation relationship between epsilon carbide and martensite was $[11\bar{2}0]_E \parallel [100]_M$. The same orientation relationship was observed in tempered martensite by Lai[94] and Murphy et al.[95] They indicated that this orientation relationship was consistent with the Jack relationship[96] in tempered martensite, i.e. $[0001]_E \parallel [011]_M$ and $(10\bar{1}0)_E \parallel (101)_M$ within 1 to 2 deg. The dark field image, figure (b) was obtained from the encircled spot in figure 18(c), showing the contrast reversal of epsilon carbide.

(b) <u>280°C Tempered Structure</u>--The microstructures of the specimens tempered at 280°C were quite different from the microstructures of the specimens tempered at 180°C. Extensive amounts of only cementite precipitation inside the lath, at the lath and grain boundaries and on twins were observed. Cementite precipitation within the lath and at the lath and grain boundaries is shown in figure 29 to 31.

Interlath films of retained austenite are not observed in these structures suggesting that the retained austenite is thermally unstable at 280°C. Several investigators[97-99] have reported that retained austenite decomposes into cementite upon tempering around 300°C. Seal and Honeycombe[100] have suggested that the absence of cementite precipitation at the lath boundaries during the low tempering temperature treatment is due to the presence of retained austenite between laths. They propose that carbides do not form at the martensite interfaces at low tempering temperatures (<280°C) because of higher solubility of carbon in the austenite. Upon tempering at higher temperatures, the retained austenite will have transformed and carbides begin to form at the lath boundaries because of high carbon concentration.

The cementite and ferrite were observed to obey the Bagaryakski orientation relationship,[101] as illustrated in figures 29(d), 30(d) and 31(c), i.e. $(100)\ Fe_3C \parallel (011)_M$; $(010)Fe_3C \parallel (111)_M$ and $(001)\ Fe_3C \parallel (211)_M$.

Figures 32 to 34 show the variation of cementite on twins as a function of austenitizing temperature. The dark field images using (002) Fe_3C spots reverse the contrast of cementite on twins. The cementite precipitates on twins as shown in figure 32(c) are very small when compared to cementite in figures 33(c) and 34(b). It is interesting to note that more cementite was precipitated on twins as the austenitization temperature was lowered or step quenched from 1200°C to 870°C.

Ogura et al[16] have shown that higher austenitization treatment tends to reduce segregation of impurities and alloying elements in the austenite. They have also shown segregation of carbon on twin boundaries will be reduced with increasing austenitizing temperature upon quenching. The segregation of carbon, during austenitization treatment or quenching, on twin boundaries may be responsible for the variation of cementite precipitation on twins as a function of austenitizing temperature.

SUMMARY OF MICROSTRUCTURE

The transmission electron microscopy results can be summarized as follows:

1. Non-martensitic products were not observed at the prior austenite grain boundaries.
2. Amount of twinning decreased with increasing austenitization temperature.
3. Retained austenite films were observed at the lath, packet and prior austenite grain boundaries. The amount of retained austenite seemed to increase slightly with increasing austenitization temperature.
4. The retained austenite was mechanically unstable at the crack tip.
5. The retained austenite was mechanically unstable under both monotonic and cyclic loading and also during tensile deformation under plane stress and plane strain conditions.
6. The lath martensite deformed by twinning under plane strain conditions, and it deformed by slip under plane

stress conditions.

7. The retained austenite was stable even after tempering at 180°C and it decomposed into ferrite and cementite upon tempering at 280°C.
8. The tempering at 180°C resulted in a microstructure consisting of both epsilon carbide and cementite while tempering at 280°C resulted only in cementite.
9. The amount of carbide precipitation on twins decreased with increasing austenitization temperature. This is consistent with segregation of carbon during austenitization or quenching treatment.

4.3 Magnetic Saturation Analysis

The amount of retained austenite in the quenched and quenched and tempered condition was determined by magnetic saturation analysis. The variation in the amount of retained austenite as a function of strain under tensile loading was also measured. The results are shown in figures 35 and 36. It is clear from these figures that the amount of retained austenite prior to loading (0% deformation) was almost independent of the austenitizing temperature. These results were in agreement with an earlier report.[7] The retained austenite content was slightly decreased upon tempering at 180°C (figure 36) and the retained austenite amount was very low (<1%) in 280°C tempered structures, suggesting that the retained austenite was thermally unstable upon tempering at 280°C. It is also evident that the retained austenite transformed to martensite upon deformation and the amount of retained austenite was less than 1% at 2% strain in all structures. A significant amount of retained austenite transforms at 0.2% strain and the retained austenite present in the 180°C tempered condition was more stable with respect to stress and strain than in the as quenched condition.

4.4 Mechanical Properties

The room temperature tensile properties of quenched and tempered AISI 4340 steel have been reported elsewhere.[102] A summary of these properties for the heat treatments studied in this investigation are listed in table IV. From this table, it is evident that plane strain fracture toughness (K_{1c}) of specimens tempered at 180°C was strongly dependent on the austenitizing temperature. The yield strength was almost independent of austenitizing temperature but tempering at 280°C, as expected, slightly decreased yield strength compared to specimens tempered at 180°C. The percentage of elongation decreased from 13.6 to 8.6 as the austenitizing temperature was increased from 870°C to 1200°C. However, Ritchie and Horn[7] have shown that percentage of elongation, under plane strain condition, was almost independent of austenitizing temperature.

4.5 Fatigue Crack Growth

4.5.1 Effect of Microstructure on Crack Growth.

Fatigue crack propagation data is presented in the form of crack growth rate curves of da/dN vs ΔK, plotted on logarithmic scales over a range of growth rates 10^{-8} to 10^{-3} in/cycle. The variation of crack growth rate as a function of stress intensity range for all microstructures is shown in figures 37 to 44. The effect of prior austenite grain size on crack growth rates is compared in figure 45. In order to avoid overlapping of data points, not all curves are plotted in figure 45 but the trend is the same. All curves exhibited three distinct regions, viz. regions A, B and C (threshold region, linear crack growth rate region and fast crack growth rate region), which are characteristically observed in fatigue crack growth curves.

Crack growth rates for all microstructures were measured as low as 10^{-8} in/cycle and the corresponding stress intensity was taken as threshold stress intensity, ΔK_0, for fatigue crack growth. The threshold stress intensity range was approximately 2.8 $Ksi\sqrt{in}$ for all microstructures. The fatigue crack growth rates were also nearly independent of microstructure at low and intermediate stress intensity ranges. The accuracy of the instron testing system, used in this program, in determining applied ΔK at low stress intensity ranges was 0.2 $Ksi\sqrt{in}$. Thus a slight decrease in crack growth rates at low ΔK (figure 45) in specimens with coarse grain structures was considered negligible. Similar decrease in crack growth rates has been reported in 300 M steel when the prior austenite grain size was increased from 20 μm to 200 μm.[8] However, the accuracy of their testing system was not reported.[8]

The intermediate range of crack growth rates, represented by the linear portion of crack growth curves (region B), could be represented by the Paris equation (1). The values of material constants A and m of the Paris equation are listed in table V for all heat treatments. There was no significant difference in the magnitude of constant "m". A slight variation in the values of "A" was observed with heat treatment. Miller[103] and others[24] have shown that the value of "m" was inversely related to the static fracture toughness. The variation of "m" with plane strain fracture toughness compared with the results of several investigations is shown in figure 46. It is clear from this figure that the results of the present investigation are in agreement with earlier reports.[6,24]

Although there was little variation in crack growth rates between various microstructures (figure 45), the transition from region B crack growth to region C was strongly dependent on fracture toughness of the material. The region B crack growth was extended to higher stress intensity ranges in 1200°C/180°C structures than in 870°C/180°C structures (figure 45). At high stress intensities the 1200°C/180°C structure showed better resistance to crack growth than the 870°C/180°C structure because of the higher toughness of the former structure. The extension of region B to higher stress intensity ranges is beneficial because it would increase the probability of detecting a crack in service before catastrophic failure occurs. All microstructures exhibited an acceleration in crack growth rates, as K_{max} approached K_{1c}.

4.5.2 Effect of Microstructure and Internal Hydrogen on Crack Growth. The fatigue crack growth rates obtained from charged specimens for all heat treatments are shown in figures 47 to 54. Although all curves show three clearly distinguishable regions of crack growth rates, when the applied K_{max} was greater than K_{1scc}, stress corrosion fatigue region, the slope of log da/dN vs log ΔK nearly approaches zero suggesting that static hydrogen assisted cracking component was playing an important role.

The fatigue crack growth rates of charged specimens are compared with the crack growth rates of specimens without hydrogen as a function of austenitizing temperature in figure 55. However, crack growth data obtained from step quenched specimens are not included in these figures since the crack growth rates were almost the same as in the specimens quenched directly from 1200°C (figure 56). The differences in microstructure between the direct quench from 1200°C and the step quench from 1200°C to 870°C specimens were the absence of twinning and segregation in the former case. The fact that similar crack growth rates were observed in both structures suggests that twinning and segregation did not play a significant role. Crack growth rates seemed to depend only on prior austenite grain size for a given tempering treatment. These curves clearly demonstrate the regions of true corrosion fatigue and stress corrosion fatigue. (The threshold stress intensity, K_{1scc}, was found to vary from 10 to 16 ksi$\sqrt{in.}$ for these microstructures[12]). It is evident from these figures that the presence of internal hydrogen enhanced the fatigue crack growth rates. The enhancement in crack growth rates in charged specimens tempered at 280°C is shown in figure 56 for different grain sizes. The maximum enhancement in crack growth rates was observed at intermediate stress intensity ranges (ΔK = 8 to 15 ksi$\sqrt{in.}$, i.e., K_{max} = 10.5 to 20 ksi$\sqrt{in.}$) for all microstructures (figure 56). It is clear from figure 56 that increasing the prior austenite grain size the maximum enhancement in crack growth occurred at higher stress intensities.

This enhancement in crack growth rate was associated with the threshold stress intensity for hydrogen assisted cracking, K_{1scc}. At low stress intensity ranges ($\Delta K<10$ ksi$\sqrt{\text{in.}}$) the crack growth rates in the specimens with coarse grained structures were lower than those with fine grained structures. As the prior austenite grain size was increased from 25μm to 250μm (by austenitizing at higher temperatures than the conventional 870°C) the crack growth rate decreased from 2×10^{-5} to 9×10^{-7} in/cycle at $\Delta K = 3$ ksi$\sqrt{\text{in.}}$ At an intermediate stress intensity region, $\Delta K>10$ ksi $\sqrt{\text{in.}}$ slightly higher crack growth rates were observed in the specimens with coarse grained structures than in the specimens with fine grained structures. The extension of this region was dependent on plane strain fracture toughness (figure 55).

The effect of tempering temperature on crack growth rates is shown in figures 57 to 60 for different grain sizes. The crack growth rates at low stress intensity ranges were independent of tempering temperature. It is evident from these figures that tempering at 280°C instead of 180°C slightly increased the crack growth rates at intermediate stress intensity ranges regardless of austenitizing treatment.

The differences in microstructure between specimens tempered at 280°C and 180°C are the absence of retained austenite and the transition of carbides from epsilon carbide + cementite to cementite in specimens tempered at 280°C. In addition to these microstructural differences, the yield strength of specimens tempered at 280°C was about 20 ksi lower than those tempered at 180°C. The presence of retained austenite and epsilon carbide was reported to be beneficial for hydrogen assisted cracking.

Based on this argument, the specimens tempered at 180°C should exhibit lower crack growth rates than for the specimens tempered at 280°C. However, the susceptibility to hydrogen assisted cracking decreases with decreasing yield strength. Dropping the yield strength by tempering at 280°C instead of 180°C should lower the crack growth rates. Hence, the effects of yield strength, absence of retained austenite, and carbide type are opposite. Thus, at low stress intensity ranges the drop in yield strength in specimens tempered at 280°C may be counteracting the detrimental affect of cementite and absence of retained austenite; while at intermediate stress intensity ranges the transition from epsilon carbide to cementite predominates over the yield strength effect (since retained austenite is mechanically unstable).

Summarizing, for the crack growth rate results of cathodically charged specimens, an increase in the prior austenite grain size decreased the crack growth rates at low stress intensity ranges. On the other hand, an increase in the prior austenite grain size or replacement of epsilon carbide with cementite slightly increased the crack growth rates at intermediate stress intensity ranges.

4.6 Fractography

Following the crack growth testing, the fracture surfaces were examined using a scanning electron microscope to determine the mechanism of crack growth (mode of failure) at various stress intensity ranges for each heat treatment.

4.6.1 Effect of Microstructure. Fracture morphology near threshold stress intensity range, $\Delta K = 3$ ksi$\sqrt{in.}$, consisted of a flat, ductile transgranular mode with isolated areas of intergranular separation (figure 61). It is clear from this figure that the amount of intergranular fracture was less than 1% for all grain sizes. This suggests that the grain boundaries are more resistant to fracture than the grain interiors. The percentage of intergranular fracture increased with increasing stress intensity range and reached a maximum for all heat treatments at around $K = 8$ to 15 ksi$\sqrt{in.}$ A further increase in the applied stress intensity range resulted in a drop in the amount of intergranular fracture (figure 62). Although no quantitative estimations were made, the percentage of intergranular fracture was slightly higher in specimens tempered at 280°C than in specimens tempered at 180°C (figure 63). Similar observations were made by Ritchie[9,30] in 300 M steel. The appearance of these intergranular facets varied in their surface roughness--some were flat and featureless, some were dimpled and others exhibited a localized tearing representative of local ductility. Typical localized tearing on an intergranular facet is shown in figure 64. Some of these regions exhibited ductile fatigue striations as shown in figure 64 (b) and (c). The calculated crack growth rate from the average spacing of these striations (7×10^{-6} in/cycle) was approximately equal to the macroscopically measured crack growth rate (1×10^{-5} in/cycle). This type of striations were observed only in the specimens austenitized at 1200°C and tempered at 180°C.

At intermediate stress intensity ranges, $\Delta K > 15$ ksi$\sqrt{in}$, the mechanism of crack growth is shown in figures 65 and 66. In agreement with the earlier reports on similar steels,[104] the distinct fatigue striations were observed only as isolated packets. Typical such regions are shown in figure 66. Once again the calculated crack growth rates from the average spacing of these striations are approximately equal to the measured crack growth rates. It is also evident from these figures that the striations cover a larger area in 1200°C/180°C structures than in 1100°C/180°C or 870°C/180°C structures and packets of striations were more often observed in structures with high fracture toughness. Miller et al[104] have observed the fatigue striations as isolated patches in 4340 steel and reported that the amount of striations increased with toughness. Hence, the present observation is consistent with the fact that improved toughness enhances the localized ductility ahead of a crack tip and thus increases the probability of observing distinct striations in specimens exhibiting higher fracture toughness.

At high stress intensity ranges, corresponding to region C crack growth, the mechanism of failure consisted of fibrous, quasicleavage, and intergranular separation (figure 67). The onset of this region which is sensitive to the fracture toughness is consistent with the presence of static mode of failure (figure 67).

4.6.2 Effect of Internal Hydrogen. The fracture morphology at low stress intensity ranges, $\Delta K = 3\ \text{Ksi}\sqrt{\text{in}}$, was predominantly intergranular in fine grained structures (870°C/180°C or 280°C) while in coarse grained structures it was mostly transgranular (figure 68). The variation in the amount of intergranular fracture as a function of grain size in uncharged and charged specimens is shown in table VI. The variation of intergranular fracture with grain size in specimens tempered at 280°C was not included in this table since the trend was the same. However, the amount of intergranular fracture was slightly higher in specimens tempered at 280°C than in the specimens tempered at 180°C. It is clear from this table that the percentage of intergranular fracture in charged specimens decreases with increasing prior austenite grain size, while in uncharged specimens the mode of failure is predominantly transgranular for all grain sizes. These results suggest that in uncharged specimens the grain boundaries are stronger than grains, while in charged specimens the prior austenite grain boundaries are weakened because of the diffusion of hydrogen to the grain boundaries. In coarse grain structures hydrogen has to diffuse over a larger region ahead of a crack tip in order to weaken the grain boundaries, which results in a reduced environmental influence. The fracture morphology in fine grain structures (25μm) was very similar to that observed in the same 4340 steel tested under sustained loading.[12] This similarity indicates that sustained-load crack growth and fatigue crack growth below K_{1scc} followed essentially the same path through the prior austenite grain boundaries. The percentage of intergranular fracture increased with stress intensity range for all grain sizes (figure 69) and the maximum percent intergranular fracture occurred at ΔK values of 8-15 $Ksi\sqrt{in}$.

At intermediate stress intensity ranges the mode of failure was predominantly by intergranular separation regardless of the prior austenite grain size (figures 69(c) and 70). These intergranular facets were nearly featureless and no evidence of fatigue striations was observed on these facets. In the regions of transgranular failure, fatigue striations were occasionally observed in 1200°C/180°C structures as shown in figure 71. This figure also shows a ductile mode of failure in addition to fatigue striations. The difference in crack growth rates between charged and uncharged specimens at stress intensity range around 20 to 30 $\text{Ksi}\sqrt{\text{in.}}$ was small (figure 55) suggesting that the crack growth due to fatigue was equally important in charged specimens. Hence, it was possible to observe isolated patches of striations in specimens exhibiting higher fracture toughness. As the stress intensity range increased, in addition to intergranular separation, ductile rupture was also observed (figure 72).

4.7 Hydrogen Analysis

The bulk hydrogen content was obtained by analyzing coupons cut from charged compact tension specimens. The average hydrogen content is shown in table VII. In general, the average content was approximately independent of heat treatment except for 1200°C/180°C. However, the number of coupons that were analyzed for 1200°C/180°C treatment was limited, and often the two coupons that were cut from the same charged specimen exhibited a varied hydrogen content which suggests that hydrogen distribution was non uniform in these samples. The non uniform hydrogen distribution in a given sample and varying hydrogen levels varying from one specimen to another for a given heat treatment made it difficult to establish a correlation between hydrogen content and crack growth rates.

5. DISCUSSION

5.1 Effect of Microstructure on Fatigue Crack Growth

The fatigue crack growth results confirmed that the microstructure has an influence on crack growth rates only at high stress intensity ranges. Crack growth rates were nearly independent of microstructure at low and at intermediate stress intensity ranges. At high stress intensity ranges the specimens exhibiting higher toughness showed better resistance to crack growth.

Ritchie's model for threshold stress intensity predicts that threshold stress intensity will be reduced by increasing either the yield stress or the load ratio, since these increase hydrostatic tension at the crack tip. Thus, the local concentration of hydrogen is increased, resulting in a lower threshold.[9] This model does not account for prior austenite grain size effects on crack growth rates near threshold stress intensity. Masounave and Bailon[35] and Priddle[36] have explained the grain size dependence of threshold by considering the crack tip deviation in coarse grained material. These explanations failed to predict the absence of load ratio effect on the threshold measurements in vacuum[25,38,39] where crack tip deviation is equally likely to occur. Furthermore, a corrosive product has been observed by several investigators[25,34,39,40,41] on the fractured surfaces from the threshold region. Several other investigators have also reported that the occurrence of intergranular failure near threshold was also dependent on the air environment[25,39,40,41] and that an intergranular failure mode was absent in specimens tested in vacuum.

Ritchie[9] did not observe intergranular cracking in 300M steel, quenched and tempered at 650°C condition and this observation is consistent with the fact that the susceptibility of steel to hydrogen embrittlement decreases with decreasing yield strength. These observations suggest that any realistic model for the threshold in steels must include environment effects.

Ritchie[9] and others[25,34,38] have argued that the moisture in air decomposes into atomic hydrogen and oxygen at the crack tip, and that the stress gradient at the crack tip drives the hydrogen into the metal which results in the reduction of cohesive strength. The diffusion of hydrogen to the grain boundaries, ahead of a crack tip, weakens the grain boundaries relative to the grain interiors and thus contributes to intergranular failure. In order to weaken the grain boundaries of coarse grained structures, hydrogen has to diffuse farther and hence results in a reduced environmental influence in coarse grained structures compared to fine grained structures.

The mode of failure was predominantly transgranular at $\Delta K = 3$ Ksi$\sqrt{in}$ and the amount of intergranular fracture increased with increasing stress intensity range (figure 62). The maximum amount of intergranular fracture was observed around $\Delta K = 8$-15 Ksi$\sqrt{in}$ for all grain sizes. Cooke et al[39] have postulated that the peak incidence of intergranular fracture mode occurred when the reverse plastic zone size at the crack tip becomes equal to the prior austenite grain size. This conclusion was drawn based on their[39] results of En 30 steel with a prior austenite grain size of 18μm. This type of relationship is not observed in the present investigation particularly when the prior austenite grain size is 100 or 250μm. Gerberich and Moody[23] have pointed out that this peak maximum percentage of intergranular fracture might occur when the maximum stress intensity at the crack tip equals K_{1scc}. The present fractography results confirm that the occurrence of maximum percentage of intergranular fracture does coincide with K_{1scc} since K_{1scc} of these structures has been reported to vary from 10 to 16 Ksi$\sqrt{in.}$[12]

At intermediate stress intensity ranges, where the crack growth curve is linear, the crack growth is associated with a ductile striation mechanism (figures 65 and 66). The value of M in the Paris equation (1) has been found to be between 2.6 and 2.8. This is consistent with most metallurgical and mechanical models[105,106] of ductile fatigue crack growth. These fatigue crack growth models are based on the concept of one striation growth per cycle and predict little or no influence of microstructure on crack growth rate. The present results are consistent with these models.

At high stress intensity ranges (region C), the present results show accelerated crack growth rates associated with the presence of static modes of failure (figure 67). The crack growth rates in this region are primarily controlled by the fracture toughness of the material, and, hence, microstructure plays an important role on fatigue crack growth in region C.

5.2 Effect of Microstructure and Internal Hydrogen on Fatigue Crack Growth.

Several investigators[50-57,60] have studied the influence of external hydrogen or water vapor on fatigue crack growth behavior below and above

K_{1scc}. Based on the similarities of hydrogen assisted cracking under cyclic loading and sustained loading, these investigators have concluded that the mechanism of hydrogen embrittlement and mode of failure were the same under both loading conditions.[60,64,107] The effect of microstructure on fatigue crack growth in cathodically charged specimens will be discussed in the following sections.

(a) Effect of twinning--The fractography results in the present study as well as other investigations[51,60,65,107,110] indicate that hydrogen assisted cracking component in high strength steels under cyclic loading is due to intergranular separation. The variation of twinning (twinned plate martensite vs. lath martensite) in the microstructures used in this study did not have a significant influence on fatigue crack growth rates in charged specimens. Furthermore, the similar crack growth rates that were observed in specimens directly quenched from 1200°C and in step quenched specimens in the present study is consistent with the above argument (figure 57).

(b) Effect of retained austenite--The presence of retained austenite in high strength steels has been claimed to exert a beneficial effect on hydrogen assisted cracking.[111,112] The solubility of hydrogen in the austenite is higher than in martensite and the diffusivity of hydrogen in austenite is lower than in martensite.[113] Hence, in principle, the retained austenite traps hydrogen and thus delays diffusion of hydrogen to the crack tip and reduces the crack growth rates.

Lesser and Gerberich[10] have observed a decrease in the crack growth rates under sustained loading as the austenitizing temperature was increased. The reduction in the crack growth rates was attributed partly to the retained austenite. However, their heat treatments involved austenitizing at various temperatures and then a tempering treatment at 300°C for 3 hrs. The present transmission electron microscopy results, as well as the results of others[98,99] confirm that the retained austenite decomposes into ferrite and cementite upon tempering at 280°C. Hence, the beneficial effect of high temperature austenitization treatment in the Lessar and Gerberich[10] study cannot be attributed to the retained austenite.

It has been reported[1] that the amount of retained austenite increases with austenitizing temperature in 4340 steel. Contrary to these observations, Youngblood and Raghavan[4] and McDarmaid[3] based on transmission electron microscopy results of 300M steel and Horn and Ritchie[7] based on magnetic saturation analysis of 4340 steel, have reported that the amount of retained austenite was independent of austenitizing temperature. In this investigation, the transmission electron microscopy results revealed that the variation in the amount of retained austenite as a function of the austenitizing treatments used in this study was estimated to be about ≈3 to ≈5 percent. However, magnetic saturation analysis indicated that the amount of retained austenite was about the same in both the structures austenitized at 870°C and 1200°C (figures 35 and 36).

The retained austenite was mechanically unstable within the plastic zone ahead of a crack tip (under either monotonic or cyclic loading and during tensile deformation either plane stress or plane strain conditions). Furthermore, the magnetic saturation analysis indicated that significant amounts of retained austenite transformed to martensite at a stress corresponding to 0.02 percent strain, figures 35 and 36. Under plane strain conditions, in the region surrounding the plastic zone (size rp) and extending to twice its dimensions (2rp), the stresses would still be greater than uniaxial strength of the material (figure 73). Horn and Ritchie[7] have concluded that the transformation of retained austenite in as quenched 4340 steel is stress controlled. Thus, according to the present observations and the observations made by Horn and Ritchie,[7] the retained austenite within the plastic zone and surrounding the region where stresses are greater than the yield stress would transform to untempered martensite.

At very low stress intensity ranges the forward plastic zone size is very small compared to even the smallest grain size (20-25μm). Hence, the amount of retained austenite that is being transformed due to stresses can be neglected. Thus, in principle, the presence of retained austenite should decrease the susceptibility to hydrogen assisted cracking at low stress intensity ranges. However, the variation in the amount of retained austenite among the specimens tempered at 180°C was estimated to be about ≈3% to ≈5%, and its effectiveness may not be strong enough to contribute significantly to the observed difference (an order of magnitude) in crack growth rates. The maximum variation in the amount of retained austenite in specimens tempered at 180°C and 280°C was almost 1% to 5%. Even in these specimens, the presence of retained austenite did not reduce the crack growth rates (figure 60). However, the specimens tempered at 280°C have almost 20 Ksi lower yield strength than the specimens tempered at 180°C. The susceptibility of a steel to hydrogen embrittlement increases with increasing yield strength. Further tempering at 280°C instead of at 180°C replaces epsilon carbide by cementite. Thus, the effects of the decrease in yield strength, transition of epsilon carbide to cementite, and absence of retained austenite might be opposing. However, the effect of a 20 Ksi drop in yield strength in ultrahigh strength steels on hydrogen assisted cracking was not significant. Because of too many variables involved, it is almost impossible to evaluate the effects of each variable on crack growth. However, the fact that similar crack growth rates were observed in specimens tempered at 180°C and at 280°C at low stress intensities suggests that the cumulative effect of these variables on crack growth is negligible. The results of Ritchie et al[111] showed little or no effect on stage I crack growth under sustained loading when the retained austenite was varied from 2% to 12% in 300M steel either by tempering at different temperatures or isothermally transforming at 250°C followed by tempering at 300°C. Hence, the present results, as well as the results of Ritchie et al[111] indicate that retained austenite is not playing a significant role in hydrogen assisted cracking at low stress intensity ranges.

At intermediate or high stress intensity ranges, the stressed region with stresses exceeding the yield stress, would extend to a significant portion of a prior austenite grain boundary even in the coarse grain structures (for example, at $\Delta K = 25$ Ksi$\sqrt{in}$, the forward plastic zone radius, rp = 36.8μm and thus stressed region in which stresses exceeding the yield stress would extend to 110.5μm ahead of crack tip). Hence, the beneficial effect of retained austenite to hydrogen assisted cracking at intermediate stress intensity ranges is questionable because of two reasons. First, the transformation of lath and grain boundary retained austenite into untempered martensite in the stressed region enhances the hydrogen assisted cracking. Second, this untempered martensite is supersaturated with hydrogen because of trapped hydrogen in the retained austenite prior to transformation. This supersaturated, untempered martensite with hydrogen would release the hydrogen which in turn would redistribute in the stressed region according to the stress gradient. Hence, the presence of mechanically unstable retained austenite may have a detrimental effect on crack growth rates at intermediate stress intensity ranges.

(c) Effect of prior austenite grain size--It has been established that the hydrostatic stress field at the crack tip is a major controlling factor in the hydrogen embrittlement process.[10,109,111,112] The diffusion of hydrogen is controlled by both elastic and plastic stress fields ahead of a growing crack as shown in figure 74.[112] At very low stress intensity ranges, $\Delta K = 3$ Ksi$\sqrt{in}$, the forward plastic zone is very small and hence the diffusion of hydrogen is controlled by only elastic stress field (figure 75). Troiano's[109] model for hydrogen assisted cracking involves the accumulation of hydrogen followed by a secondary crack nucleation at a region of maximum triaxial state of stress and subsequent joining of the main and the secondary cracks. Rice et al[114] have shown that the maximum triaxial stress ahead of a crack tip may occur at approximately $2\delta t$ (δt is the crack tip opening displacement = $K/2\sigma y\ E$) under plane strain conditions. The location of the peak triaxial stress ahead of a crack is independent of grain size. Thus, at very low stress intensity ranges, peak stresses, $K_{max} = 5\ \text{Ksi}\sqrt{\text{in}}$, may occur at approximately 0.07μm away from the crack tip for all grain sizes. Assuming that secondary crack nucleation occurs at the region of maximum triaxial stress, this does not explain the observed grain size dependence of crack growth rates at low stress intensity ranges.

Furthermore, it is evident from fractography results (table VI) that the grain boundaries are more resistant to fracture than the grains in uncharged specimens. The embrittled zone extending over a small portion of a grain boundary (0.07μm) may not be enough to trigger intergranular separation in the charged specimens, unless a critical amount of hydrogen has been transported to the prior austenite grain boundaries. Richards et al[115] have argued that intergranular fracture can occur only after enough hydrogen has been diffused to the grain boundaries ahead of the crack.

Gerberich et al.[112] have assumed that secondary cracks nucleate over a grain distance ahead of a crack tip and that the crack grows one grain at a time to explain the grain size dependence of hydrogen assisted cracking under sustained loading. Although their first assumption was not confirmed, their second assumption was supported by acoustic emission results. Gerberich et al.[112] have also developed diffusion equations as a function of grain size. Using their equation, the time required (Dt) to accumulate critical hydrogen concentrations on the prior austenite grain boundaries was estimated to be approximately 20 seconds for 25μm prior austenite grain size and 2000 seconds for 250μm prior austenite grain size, at $K_{mean} = 3$ Ksi$\sqrt{in}$, (K_{mean} is used here as it is reported to control hydrogen transport under cyclic loading).[115] The following assumptions are made in order to calculate the crack growth rates in charged specimens:

i) The crack growth in charged specimens is the algebraic sum of crack growth due to fatigue and crack growth due to hydrogen.

ii) The hydrogen assisted crack growth component results in intergranular separation and the crack advances grain by grain.

iii) Crack advancement due to hydrogen occurs only after a critical amount of hydrogen has been diffused to grain boundaries.

Crack growth rates in charged specimens, (da/dN)c, were then computed using the following equation:

$$(da/dN)c = [Dt \cdot f\ (da/dN)_{uc} + d]\ /\ Dt \qquad (4)$$

where f is the frequency, $(da/dN)_{uc}$ is the crack growth rate in uncharged specimen, and d is the average grain diameter. The estimated crack growth rates were found to be 5.4×10^{-6} in/cycle for 25μm grain size and 3.0×10^{-7} in/cycle for 250μm grain size at $\Delta K = 3.6$ Ksi$\sqrt{in}$ ($K_{mean} = 3$ Ksi$\sqrt{in}$). These values are in agreement with the measured crack growth rates of

2.2×10^{-6} in/cycle and 3.5×10^{-7} in/cycle for 25μm and 250μm grain sizes respectively.

However, similar calculations failed to predict the grain size dependence of crack growth rates in the intermediate stress intensity ranges because at low stress intensity ranges, the fluctuating stress field is small and hence approaches the static stress field, while at moderate or high stress intensity ranges, where the amplitude is large, the diffusion equations developed by Gerberich[112] for sustained loading may not be appropriate to use for predicting the crack growth rates in charged specimens.

An alternative explanation for the grain size dependence of crack growth assumes that either the entire prior austenite grain boundary or at least a significant portion of it has to be weakened by the formation of a hydrogen embrittled zone in order to cause intergranular separation. This zone is dependent on the prior austenite grain size and stress intensity range. In the case of fine grain structures, the required critical embrittlement zone is small and is achieved at low stress intensity ranges, while in the coarse grain structures, this zone is attained only at higher stress intensity ranges. The variation of grain size has an effect similar to the variation of frequency of testing on fatigue crack growth behavior in charged specimens. As the frequency increases, the size of embrittled zone ahead of a crack tip decreases for a given stress intensity range and this results in transgranular separation, while at low frequency, this zone increases and causes intergranular separation.[107] It has been observed by several investigators that corrosion fatigue growth rates decreased with increasing frequency.[53-56,107]

On the other hand, as the prior austenite grain size increases, the required critical embrittled zone for intergranular separation increases and this can only be attained at high stress intensity ranges. The fractography results indicate that the mode of failure is predominantly through intergranular separation (table VI) at low ΔK in fine grain structures and only at high ΔK in coarse grain structures. These results are consistent with the above argument. Based on this argument the coarse grain structures should result in lower crack growth rates than fine grain structures.

At intermediate stress intensity ranges, where the critical embrittled zone size is attained even in the coarse grain structures, the crack growth rates become independent of grain size. However, the growing crack has to change its direction at each triple point. In the case of fine grain structures, the crack has to change direction more often than in the coarse grain structures for a given length of crack growth. Thus, there are more constraint points (triple points) for the crack to grow in fine grain structures than in coarse grain structures. Hence, this may result in a slightly lower crack growth rate in fine grain structures than in coarse grain structures.

Frandsen and Marcus[110] have reported that the maximum enhancement in crack growth rate in hydrogen environment under cyclic loading occurs at intermediate stress intensity range in high strength martensitic steel. This maximum enhancement in crack growth has been reported to occur when the forward plastic zone radius was equal to the grain size. However, they have not altered the prior austenite grain size to confirm their hypothesis.

The maximum enhancement in crack growth in the present investigation occurred at ΔK values around 8-15 Ksi$\sqrt{in}$ (figure 56) or K_{max} = 10.5-20 Ksi$\sqrt{in}$. In the coarse grain structures the forward plastic zone size remains small compared to the grain diameter until much higher stress intensities. Thus, it is believed that maximum enhancement in crack growth occurs when the maximum stress intensity at the crack tip is equal to K_{1scc} of the material since K_{1scc} of these microstructures was found to vary from 10 to 16 Ksi$\sqrt{in}$.[12]

(d) Effect of segregation--In recent years extensive work has been carried out to establish the influence of high temperature austenitization treatment on segregation of alloy and impurity elements.[5,16] Wood[6] has suggested that higher austenitizing temperatures tend to reduce the segregation and partitioning of impurity and alloy elements (P, S, Cr, C, etc.) and this reduces lean zones that tend to transform earlier to different structures than the more highly alloyed zone. Further, Khan and Wood[79] have attributed the variation of twinning in step quenched specimens to the localized segregation within the grain. Ogura et al.[16] have shown by selective etching the segregation of these elements at twin and prior austenite grain boundaries. They have also shown the amount of segregation decreases with increasing austenitizing temperature. Ritchie et al.[116] have proposed that austenitizing above 1100°C followed by fast quenching prevents the segregation of impurities to the prior austenite grain boundaries. Clark et al.[5] have shown that thermodynamic driving force for segregation is too small above 1100°C to drive the embrittling species to the grain boundaries and below which substantial segregation to austenite grain boundaries takes place.

It has been shown by McMahon et al.[117] that segregation of impurities, particularly P and S, to grain boundaries have an additive effect on hydrogen assisted cracking. They argued that segregation of impurities to the grain boundaries reduces intergranular cohesion. In high strength steels, hydrogen assisted crack growth is often observed to occur along the prior austenite grain boundaries. This suggests that segregation of impurities play an important role. The critical hydrogen concentration required for intergranular separation will be reduced when impurities are present at the grain boundaries.

It has also been suggested[118] that the segregated impurities on grain boundaries trap hydrogen because of the interaction of impurity and hydrogen atoms and thus preventing the hydrogen diffusion into the bulk. Hence, the hydrogen concentration could build up preferentially at the grain boundaries containing impurity elements.

In steels with yield strengths greater than 200 Ksi, only a very small amount of impurity segregation is needed to embrittle the steels. Banerji et al.[119] have shown that commercial 4340 type steels were susceptible to hydrogen assisted cracking and the mode of failure was intergranular. They have also reported that threshold stress intensity, K_{1scc}, of pure steel was about five times that of commercial steel and the mode of failure was transgranular in pure steel. These results suggest that hydrogen assisted cracking in steels is intergranular only when the grain boundaries are already weakened due to the segregation of impurities.

Segregation of impurities to the grain boundaries, in principle, should increase the susceptibility of the steel to hydrogen assisted cracking. Contrary to expectations, the present investigation showed that there was no noticeable change in the crack growth rates of structures direct quenched from 1200°C and step quenched from 1200 to 870°C, tempered either at 180°C or at 280°C (figure 57). The major difference between these two structures, apart from twinning, is the amount of segregation to the grain boundary.

Recently, Briant and Banerji[120] have studied the segregation of P to grain boundaries in steels containing 0.06% and 0.03% P. Their results indicate that P segregation decreases as the austenitization temperature is increased from 870°C to 1200°C, and the difference in segregation between these two structures decreases with decreasing P content of the steel. In other words, the difference in the amount of segregated impurities in these two structures was very small in a steel containing 0.03% P. Furthermore, Simmons et al.[121] have not observed any segregated impurities on the prior austenite grain boundaries in 4340 steel containing 0.001% P after austenitizing at 843°C. However, they have reported that the hydrogen assisted cracking was intergranular in this steel suggesting that even this limited amount of segregated impurities to the grain boundary was enough to trigger intergranular failure. The steel used in the present investigation contains 0.01% P. Briant and Banerji[120] and Simmons et al.[121]

observations suggest that the variations in the amount of segregated impurities on prior austenite grain boundaries among the heat treatments used in the present study is small. This small variation probably is not enough to reflect in the crack growth rates. It is also possible that even in direct quench from 1200°C, structures may be having the required amount of segregated impurities on grain boundaries to embrittle.

Stress corrosion cracking studies of Lessar and Gerberich[10] have reported lower crack growth rates in coarse grained material. They have concluded that crack growth rates were diffusion limited only, and not due to an enhancement in the cohesive energy of the grain boundaries in the coarse grained materials (because of the reduction in the segregated impurities to the prior austenite grain boundaries).

Based on the above arguments, it is believed that the amount of segregated impurities on the grain boundaries does not vary appreciably with different heat treatments and hence does not significantly alter the crack growth rates.

(e) Effect of tempering temperature--In this study two tempering temperatures, viz. 180°C and 280°C were employed. The basic difference in these two tempered microstructures is the absence of retained austenite and the presence of 100% cementite in the specimens tempered at 280°C regardless of prior austenitizing temperature. The specimens tempered at 180°C consist of a mixture of epsilon carbide and cementite. The transition of epsilon carbide to cementite and the decomposition of retained austenite into ferrite + cementite in the specimens tempered at 280°C resulted in tempered martensite embrittlement.[98,99,122] Thus, increasing the tempering temperature from 180 to 280°C has an additional effect of increasing the susceptibility of the steel to hydrogen assisted cracking.

The change in carbide from epsilon carbide to cementite can affect the susceptibility of steel to hydrogen assisted cracking.[111] The presence of cementite at the grain boundaries may act as a nucleation site for cracking. The decomposition of grain boundary retained austenite further contributes cementite to grain boundaries in specimens tempered at 280°C.

It has been shown[111,123,124] that the microstructures containing epsilon carbide have lower stage II crack growth rates under sustained loading than microstructures containing cementite. However, the results of Ritchie[111] indicate that the transition from epsilon carbide to cementite has little or no effect on stage I crack growth. It has been suggested[124] that epsilon carbide acts as a better hydrogen trap than cementite. The addition of silicon to 4340 steel is known to enhance the stability of epsilon carbide to higher temperatures. Further, silicon reduces the diffusivity of hydrogen potentially making epsilon carbide a more effective trap for hydrogen in 300M steel.[125-127] In stress corrosion cracking studies, Davis et al.[128] found that specimens tempered at 260°C were susceptible to hydrogen embrittlement and this was associated with the precipitation of cementite at the grain boundaries.

At low stress intensity ranges, the crack growth rates in specimens tempered at 280°C were almost the same as in specimens tempered at 180°C while at intermediate stress intensity ranges, the specimens tempered at

280°C showed higher crack growth rates than the specimens tempered at 180°C (figures 58-60). In addition to the transition from epsilon carbide to cementite in specimens tempered at 280°C, the yield strength of specimens tempered at 280°C was about 20 Ksi lower than specimens tempered at 180°C. Thus, it is believed that the drop in yield strength in specimens tempered at 280°C is compensating the detrimental effect of cementite at low stress intensity ranges, while at intermediate stress intensity ranges, the transition from epsilon carbide to cementite predominates over the yield strength effect. These results are in agreement with the results of Ritchie et al..[111]

Summarizing, the present investigation has confirmed that the retained austenite and segregation during austenitization treatment were not playing a significant role on fatigue crack growth rates in charged specimens. Crack growth rates essentially depend upon the prior austenite grain size, particularly at low stress intensity ranges. Tempering at 280°C instead of 180°C enhanced the crack growth in charged specimens only at intermediate stress intensity ranges without affecting the crack growth rates at low stress intensity ranges for each grain size studied in this program.

6. CONCLUSIONS

From the results of this study of effect of microstructure and internal hydrogen on fatigue crack growth behavior in AISI 4340 steel, the following significant conclusions can be made:

1. The retained austenite was mechanically unstable ahead of a crack tip.
2. Retained austenite was also unstable during deformation under plane stress and plane strain conditions.
3. Lath martensite deformed by slip under plane stress conditions while it deformed by twinning under plane strain conditions.
4. In specimens without hydrogen the threshold stress intensity, and fatigue crack growth rates at low and intermediate stress intensity ranges were nearly independent of microstructure.
5. The region B crack growth was extended to higher stress intensities in the specimens exhibiting higher plane strain fracture toughness. Thus, these specimens showed better resistance to crack growth at high stress intensity ranges.
6. The presence of internal hydrogen enhanced the fatigue crack growth rates and the maximum enhancement was associated with an applied K_{max} equivalent to K_{1scc}.

7. The variation in the amount of retained austenite and segregation during the austenitizing treatment did not significantly affect the crack growth rates in charged specimens.
8. The tempering at 280°C instead of 180°C enhanced the crack growth rates in charged specimens only at intermediate stress intensity ranges.
9. The crack growth rates in charged specimens were essentially dependent on prior austenite grain size at low stress intensity ranges. Growth rates significantly decreased with increasing prior austenite grain size at low stress intensity ranges.
10. The crack growth dependence on grain size was explained by assuming the existence of critical embrittled zone ahead of a crack tip.
11. Finally, the high temperature austenitization treatment which increased the plane strain fracture toughness significantly, also improved the resistance to fatigue crack growth in uncharged specimens at high stress intensity ranges and in charged specimens at low and high stress intensity ranges. This heat treatment can be used in practice even when the structures are subjected to cyclic loading and/or exposed to hydrogen environment.

Table I.

CHEMICAL COMPOSITION (WT.%) OF AISI 4340 STEEL

C	Mn	Si	Cr	Ni	Mo	Cu	S	P
0.40	0.69	0.32	0.69	1.87	0.20	0.16	0.015	0.010

Table II.

HEAT TREATMENTS EMPLOYED

I.D.	Austenitizing temperature* °C	Tempering Temperature* °C
870/180	870	180
870/280	870	280
1100/180	1100	180
1100/280	1100	280
1200/180	1200	180
1200/280	1200	280
Step 180	1200 → 870	180
Step 280	1200 → 870	280

* All austenitization and tempering times were 1 hour except step treatment. For step treatment additional 0.5 hrs. austenitization treatment was given at 870°C. All specimens were quenched in agitated oil prior to tempering.

Table III.

VARIATION OF PRIOR AUSTENITE GRAIN SIZE WITH AUSTENITIZATION TREATMENT

Austenitizing Temperature °C	ASTM Grain Size No.	Average Grain Size μm
870	9	20 - 25
1100	5.5	100 - 125
1200	1	200 - 250
1200-870	1	200 - 250

Table IV.

MECHANICAL PROPERTIES OF QUENCHED AND TEMPERED
AISI 4340 STEEL

Heat Treatment	Yield Strength		Tensile Strength		Elongation	Plane Strain Fracture Toughness (K_{Ic})	
	Ksi	MPa	Ksi	MPa	(in %)	Ksi$\sqrt{in}$	MPa$\sqrt{m}$
870/180	225	1550	280	1929	13.6	55	60
870/280	200	1378	240	1654	13.7	75	82
1100/180	220	1515	242	1667	9.0	59	64
1100/280	200	1378	228	1571	9.1	71	77
1200/180	220	1515	268	1847	8.6	86	94
1200/280	200	1378	227	1564	1.2	61	67
Step/180	220	1515	260	1791	7.1	62	68
Step/280	200	1378	240	1654	7.3	52	57

Table V.

VARIATION OF MATERIAL CONSTANTS OF PARIS
EQUATION 1 WITH HEAT TREATMENTS

Heat treatment	A	m
870/180	7.94×10^{-17}	2.6
870/280	1.0×10^{-16}	2.6
1100/180	6.3×10^{-17}	2.6
1100/280	2.5×10^{-18}	2.8
1200/180	3.16×10^{-17}	2.7
1200/280	5.0×10^{-17}	2.6
Step 180	5×10^{-18}	2.8
Step 280	5×10^{-18}	2.8

Table VI.

PERCENT INTERGRANULAR FRACTURE AT $\Delta K \approx 3 MPa\sqrt{m}$

Heat Treatment	Grain Size (μm)	Intergranular Fracture (%)	
		Without Hydrogen	With Hydrogen
870/180	20- 25	<1	≈80
1100/180	100-150	<1	≈30
1200/180	200-250	<1	≈10

Table VII.

VARIATION IN HYDROGEN CONTENT WITH HEAT TREATMENT

Heat Treatment	Average Hydrogen Content in ppm by wt.	# of coupons
870/180	3.416	18
870/280	3.328	12
1100/180	3.226	20
1100/280	3.125	20
1200/180	3.10	12
1200/280	2.6	6
Step 180	3.946	12
Step 280	3.45	20

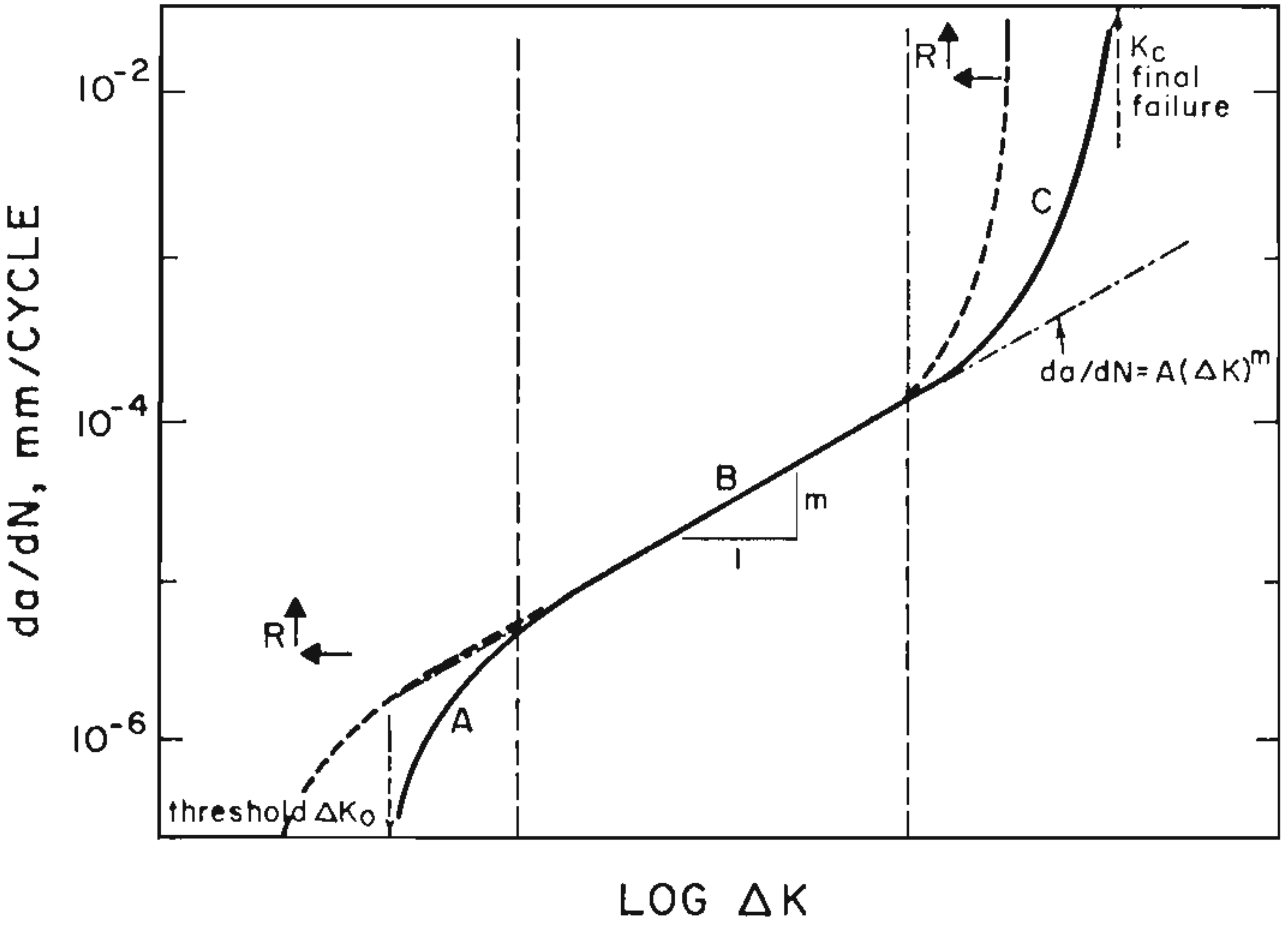

Figure 1. SCHEMATIC ILLUSTRATION OF TYPICAL FATIGUE CRACK GROWTH BEHAVIOR.

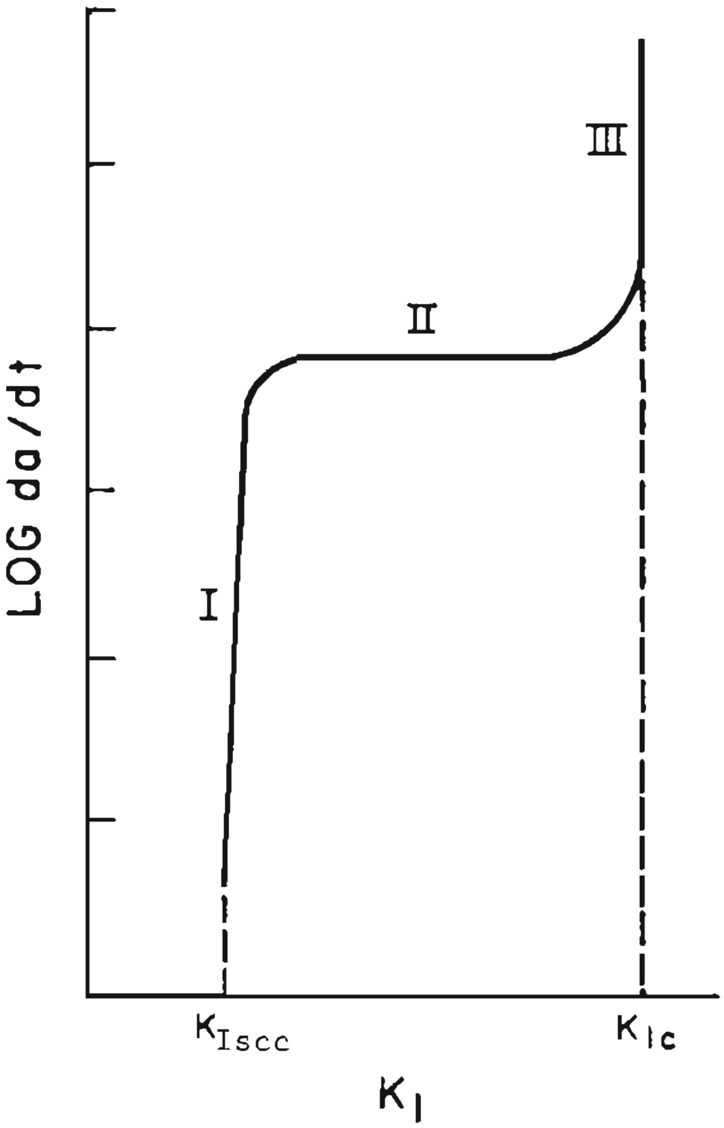

Figure 2. SCHEMATIC ILLUSTRATION OF STRESS CORROSION CRACK GROWTH BEHAVIOR.

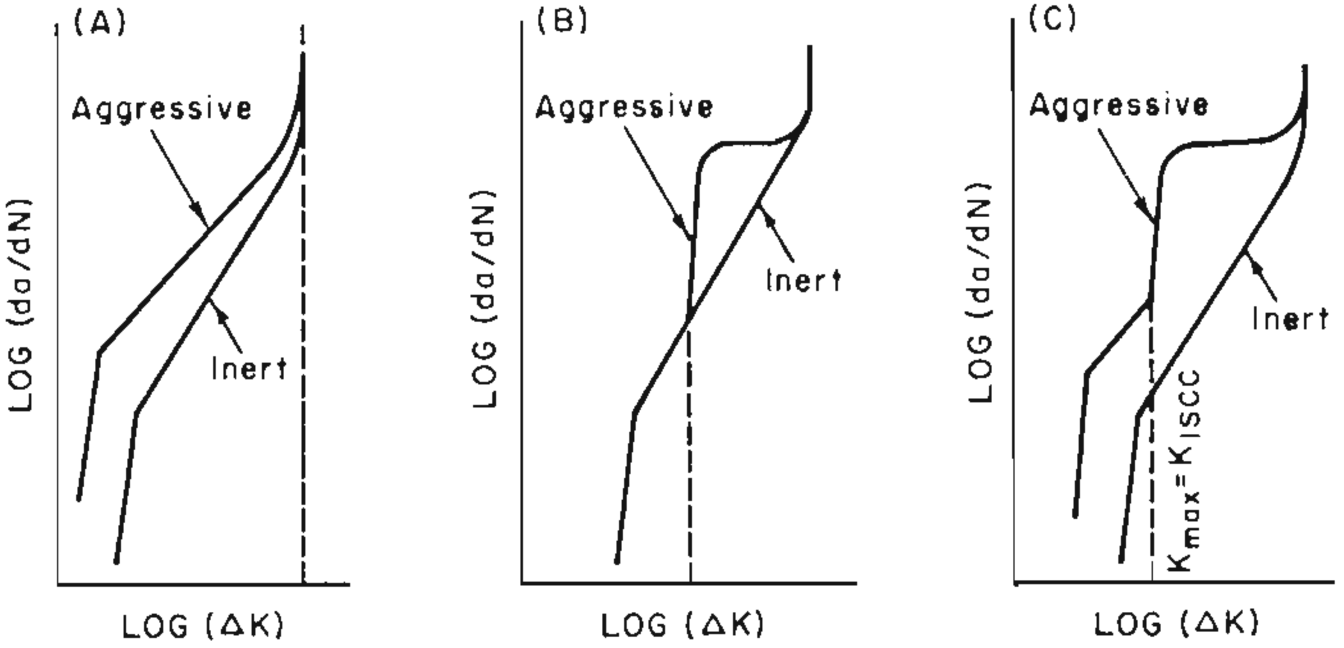

Figure 3. SCHEMATIC ILLUSTRATION OF BASIC TYPES OF CORROSION FATIGUE CRACK GROWTH BEHAVIOR.

(A) TRUE CORROSION FATIGUE (TCF)
(B) STRESS CORROSION FATIGUE (SCF)
(C) SCF ON TCF

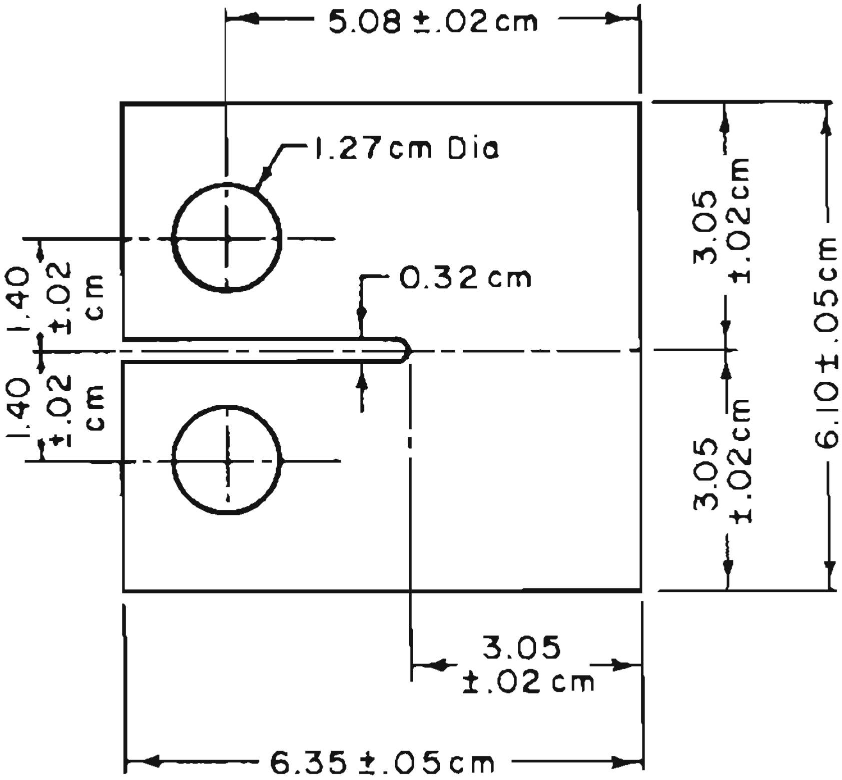

Figure 4. GEOMETRY OF COMPACT TENSION FRACTURE TOUGHNESS SPECIMEN.

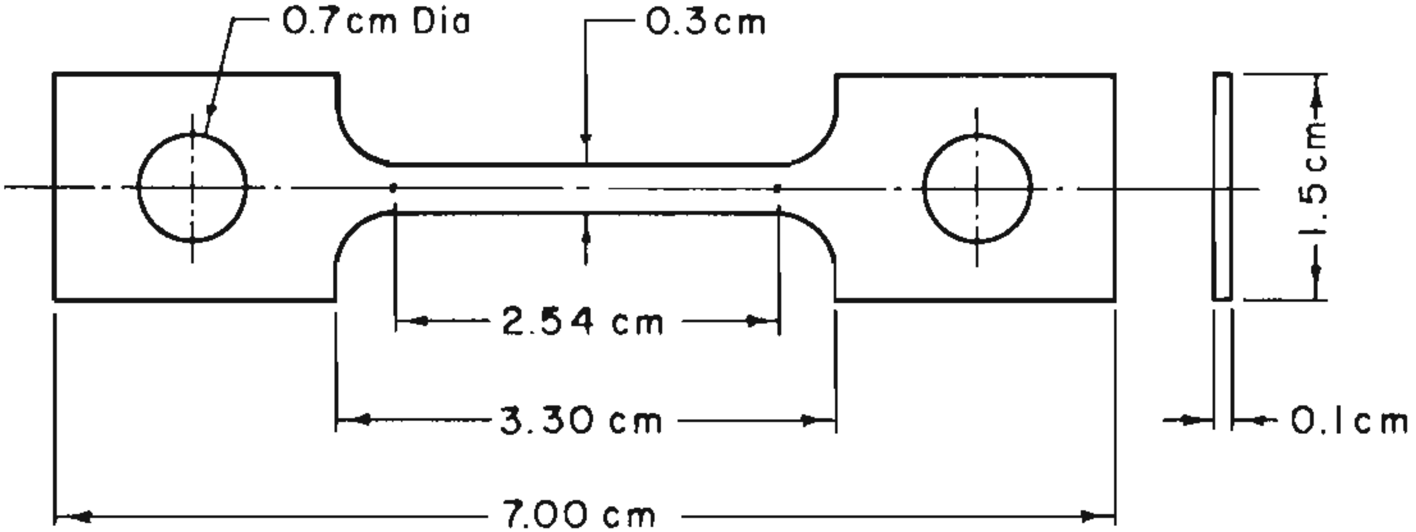

Figure 5. GEOMETRY OF THIN TENSILE SPECIMEN.

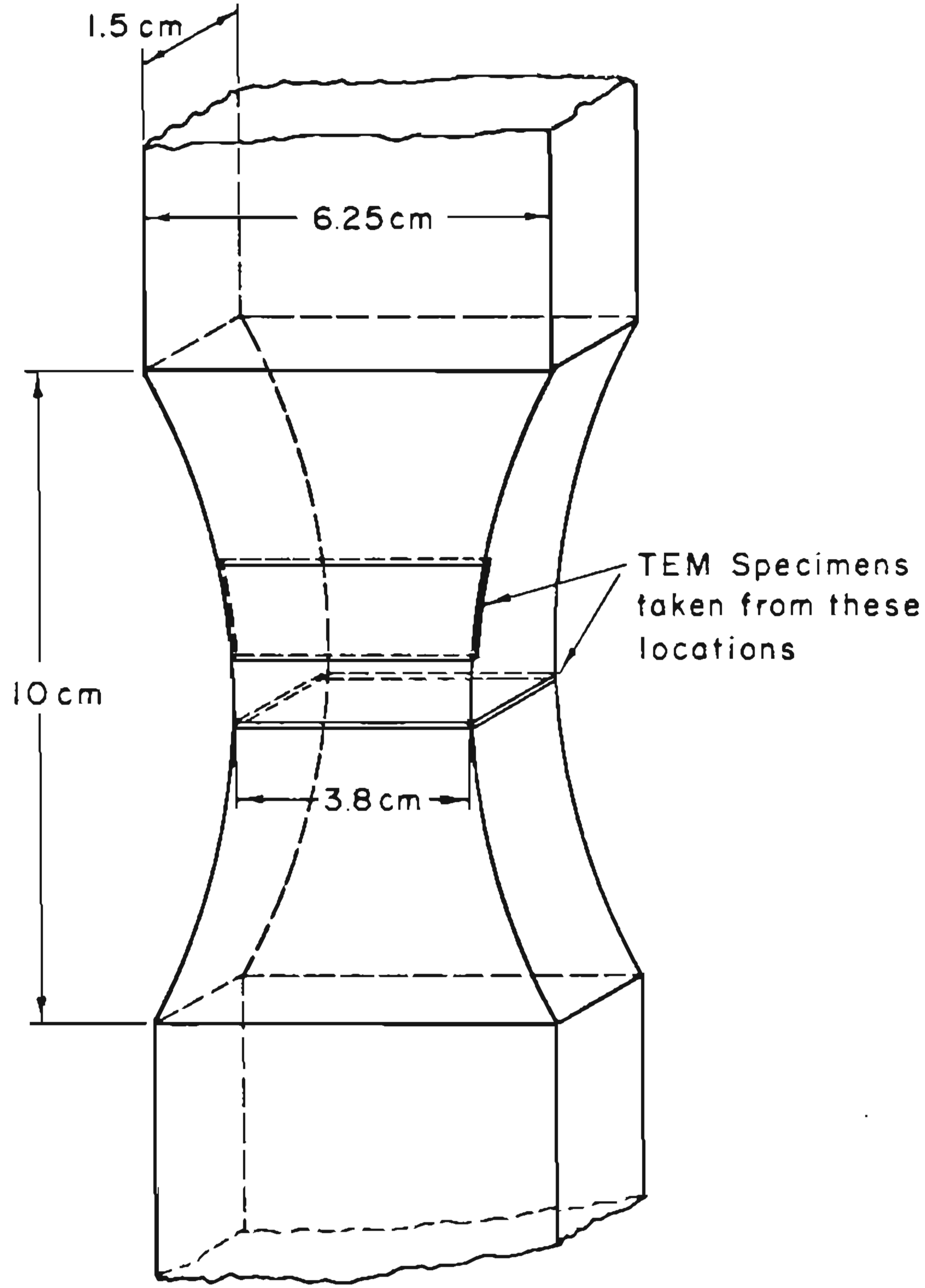

Figure 6. SCHEMATIC DIAGRAM OF TENSILE PLATE SPECIMEN SHOWING THE LOCATIONS OF THIN SLICES FOR ELECTROPOLISHING.

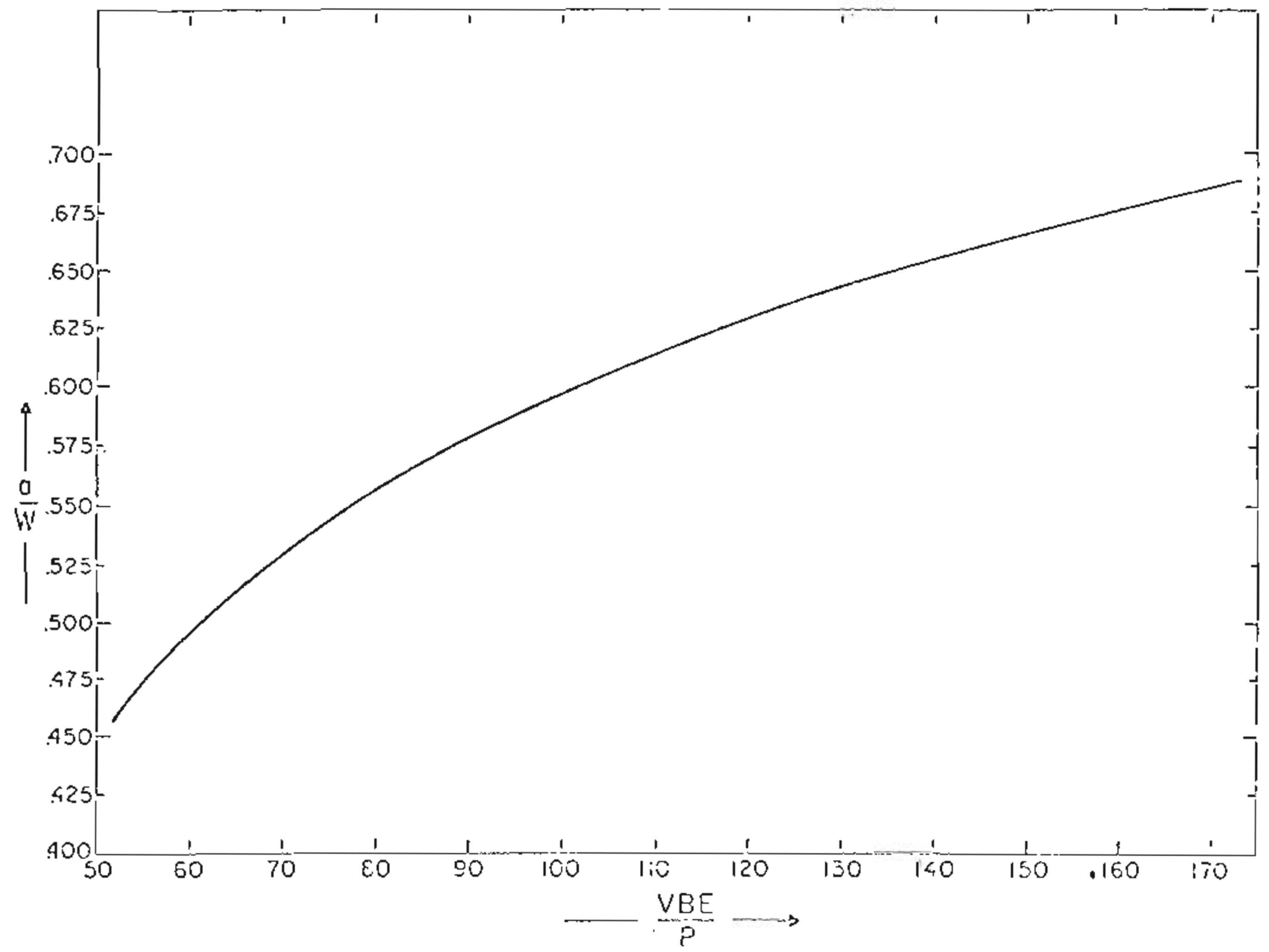

Figure 7. CRACK OPENING DISPLACEMENT AND CRACK LENGTH CALIBRATION.

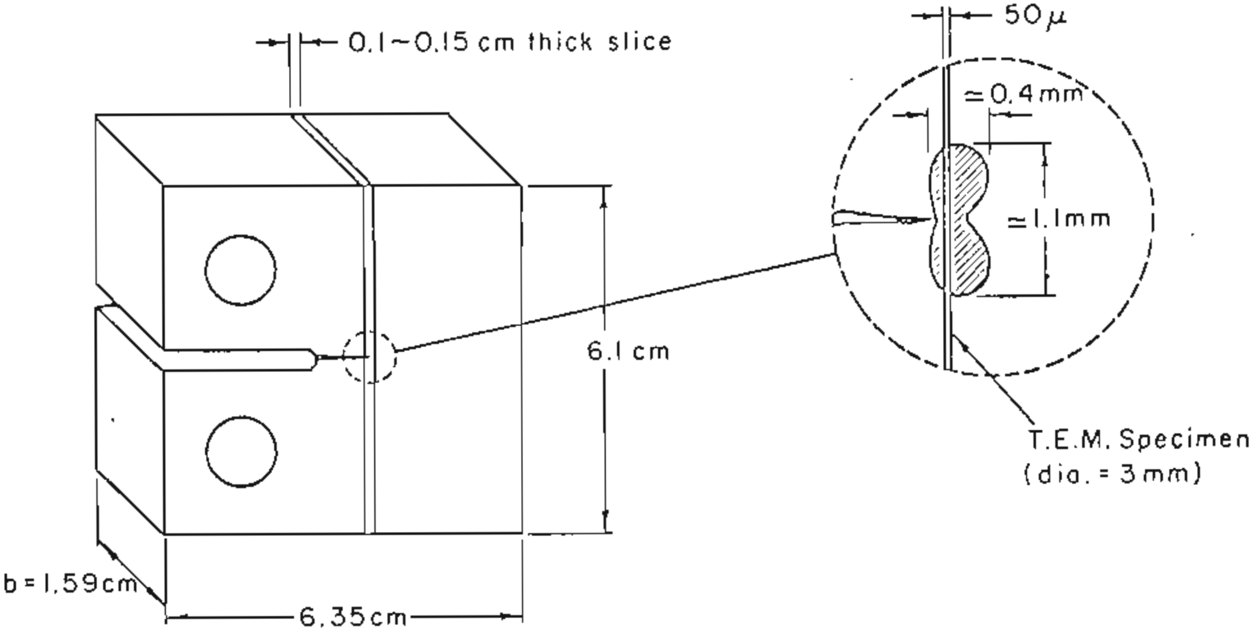

Figure 8. SCHEMATIC DIAGRAM OF A COMPACT TENSION SPECIMEN SHOWING THE LOCATION OF A THIN SLICE AND A TEM DISC FOR ELECTROPOLISHING. THE PLASTIC ZONE AHEAD OF CRACK IS ALSO SHOWN.

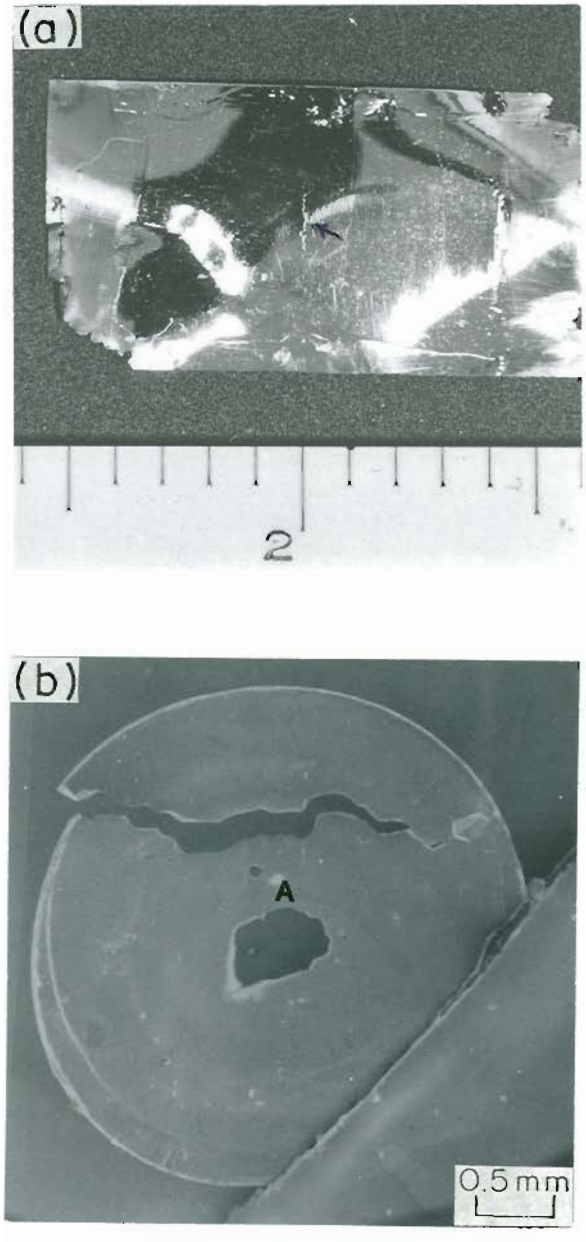

Figure 9. TYPICAL THIN FOIL USED FOR TEM.

(a) AFTER WINDOW POLISHING SHOWING CRACK
(b) AFTER JET POLISHING SHOWING CRACK AND
HOLE, REGION A REPRESENTS THE PLASTIC
ZONE.

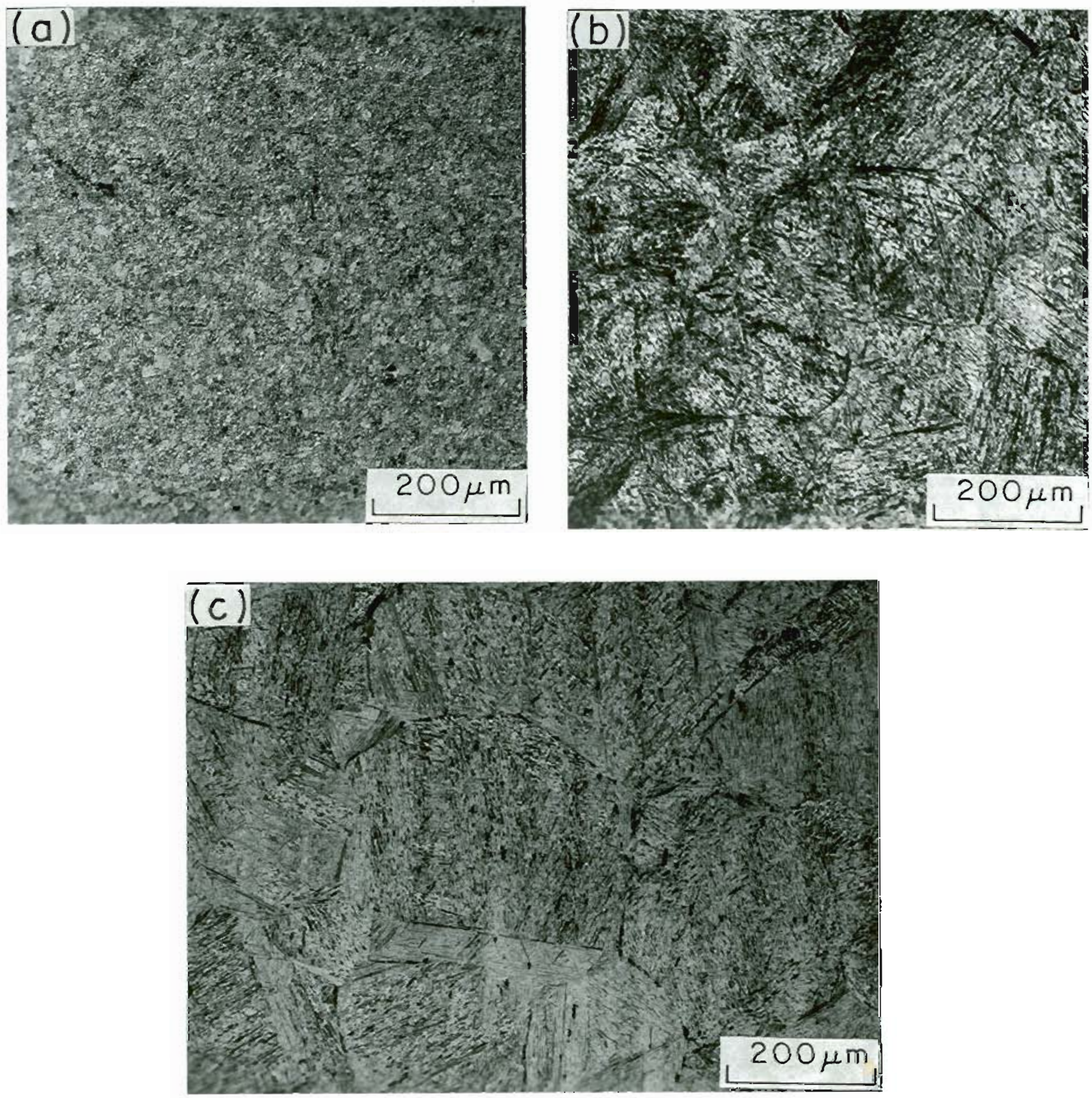

Figure 10. OPTICAL MICROGRAPHS OF AS QUENCHED AISI 4340 STEEL SHOWING THE VARIATION OF PRIOR AUSTENITE GRAIN SIZE WITH AUSTENITIZING TEMPERATURE.

(a) 870°C (b) 1100°C (c) 1200°C.

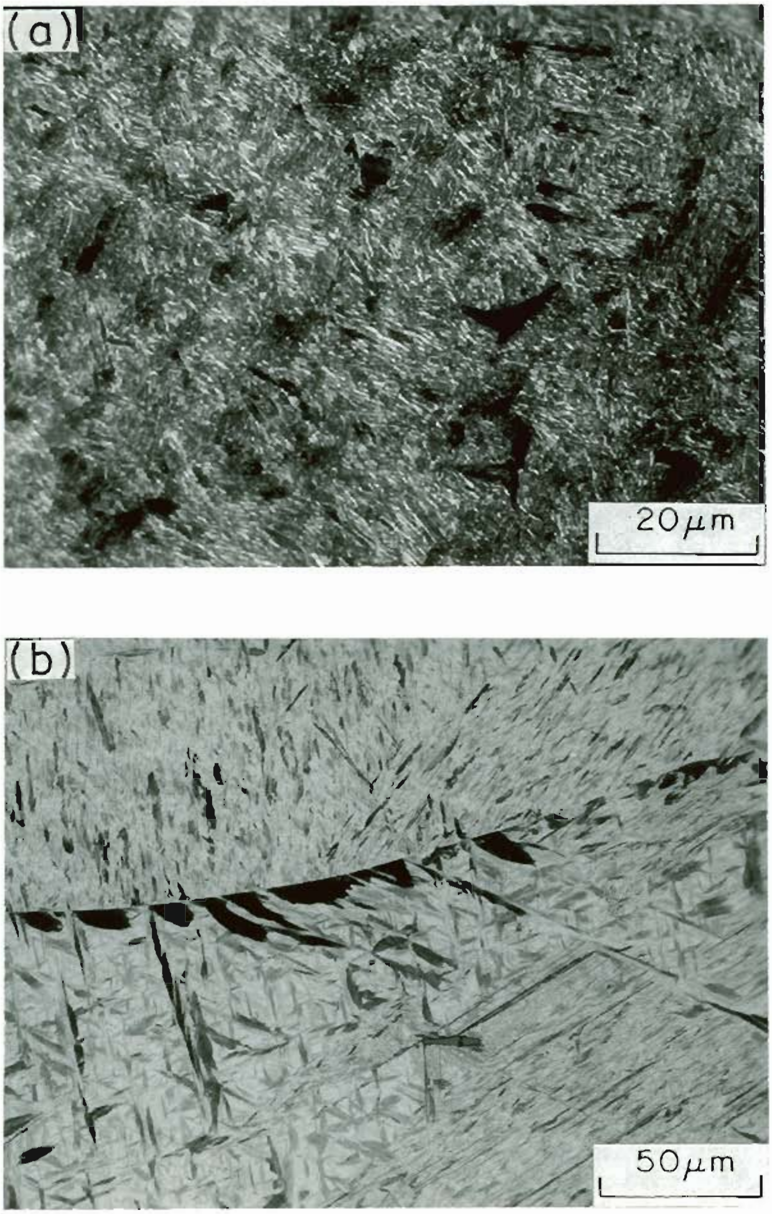

Figure 11. OPTICAL MICROGRAPHS OF AS QUENCHED AISI 4340 STEEL SHOWING DARK ETCHING CONSTITUENT

(a) AUSTENITIZED AT 870°C

(b) AUSTENITIZED AT 1200°C.

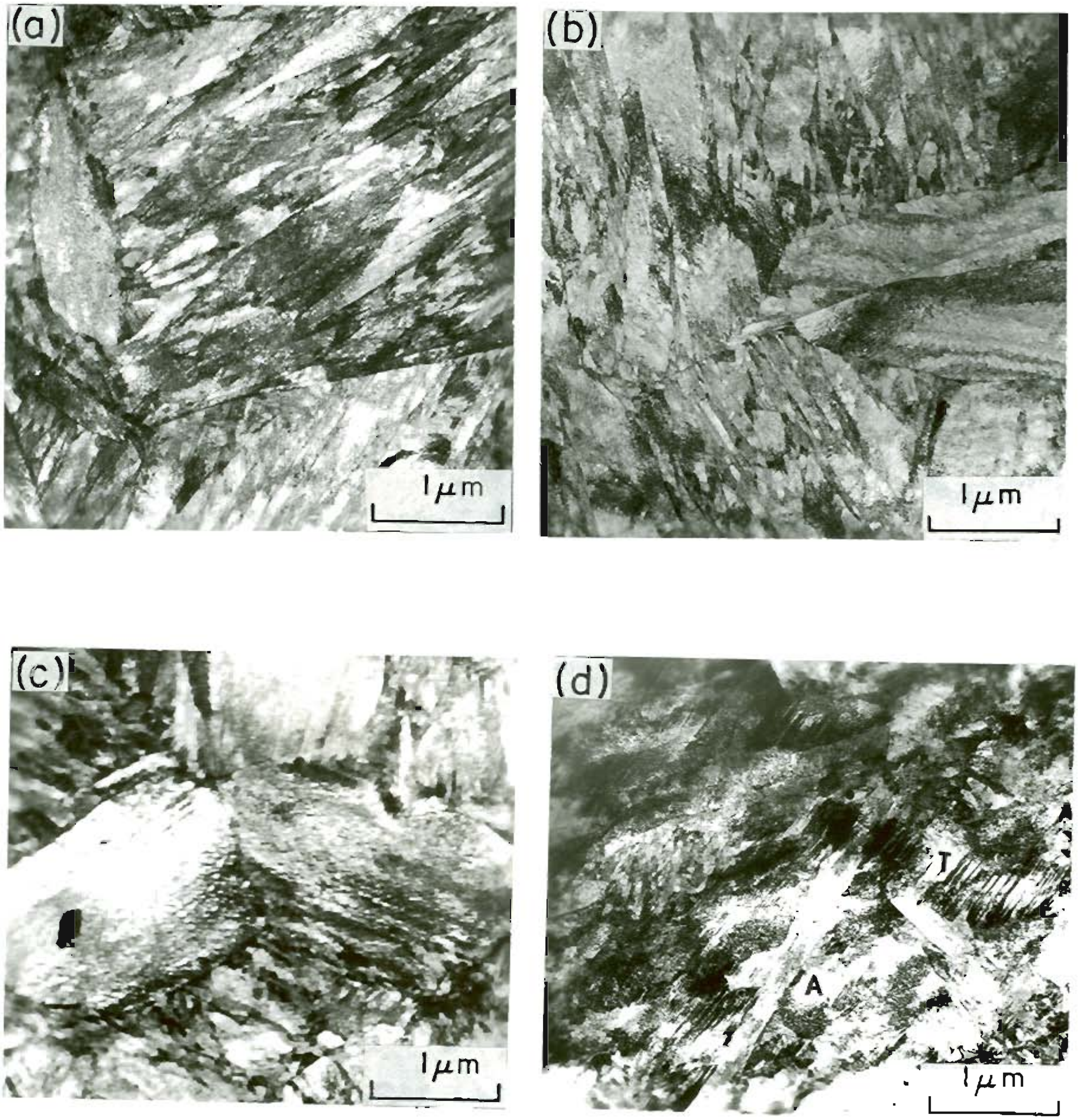

Figure 12. ELECTRON MICROGRAPHS OF 4340 STEEL AUSTENITIZED AT 870°C AND TEMPERED AT 180°C SHOWING REGIONS OF LATH AND PLATE MARTENSITE

(a) and (b) LATH MARTENSITE

(c) and (d) PLATE MARTENSITE

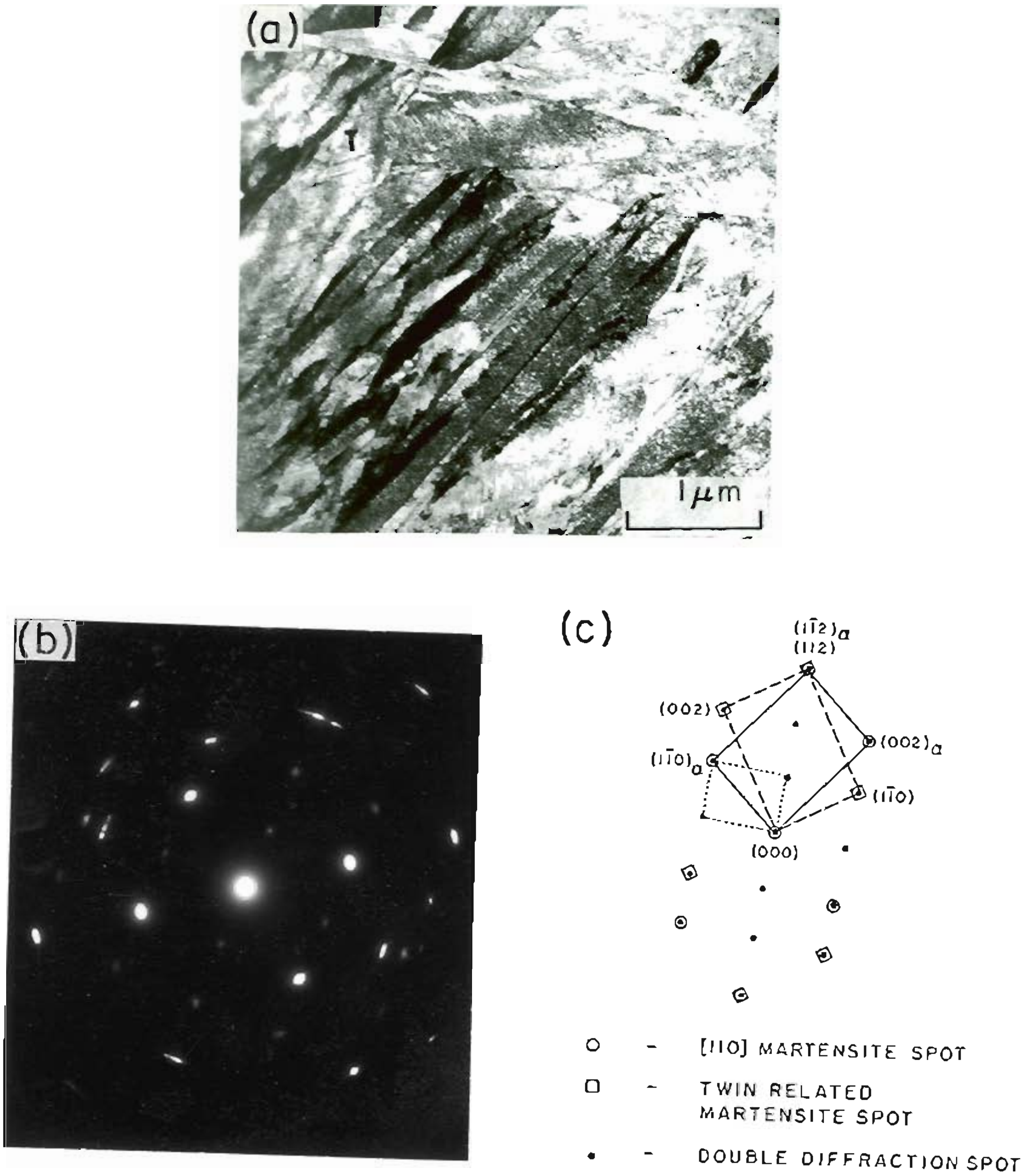

Figure 13. ELECTRON MICROGRAPHS OF AISI 4340 STEEL AUSTENITIZED AT 1200°C AND TEMPERED AT 180°C.

(a) BF MICROGRAPH SHOWING TWIN RELATED LATHS

(b) SAD PATTERN

(c) SCHEMATIC OF SAD

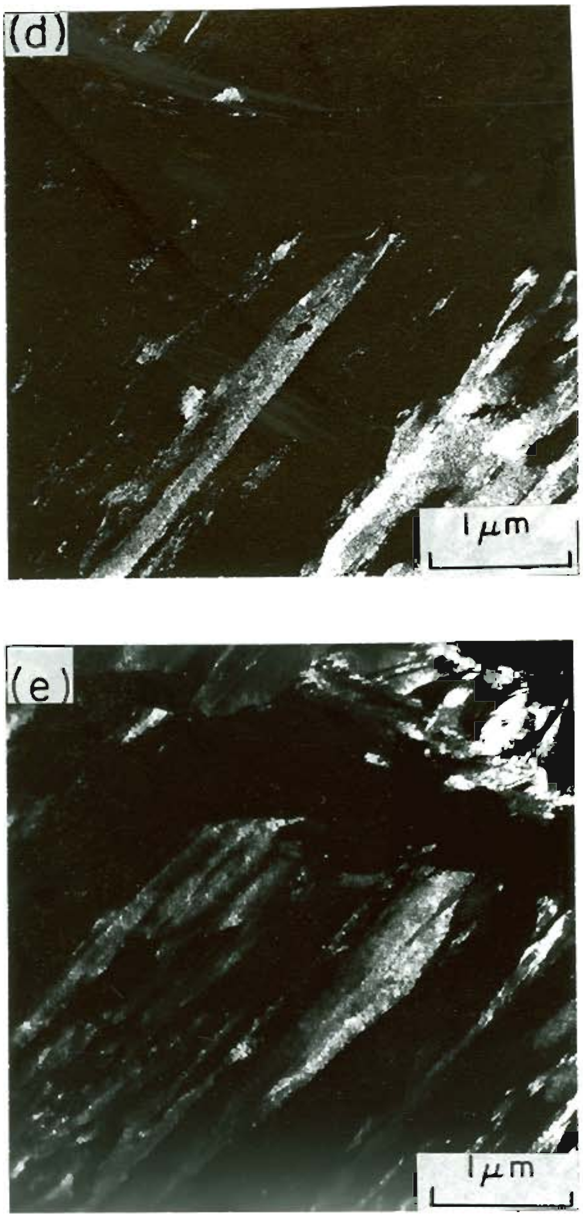

Figure 13. (cont.) ELECTRON MICROGRAPHS OF AISI 4340 STEEL AUSTENITIZED AT 1200°C AND TEMPERED AT 180°C.

(d) and (e) ARE DF MICROGRAPHS SHOWING REVERSAL CONTRAST OF TWIN RELATED LATHS.

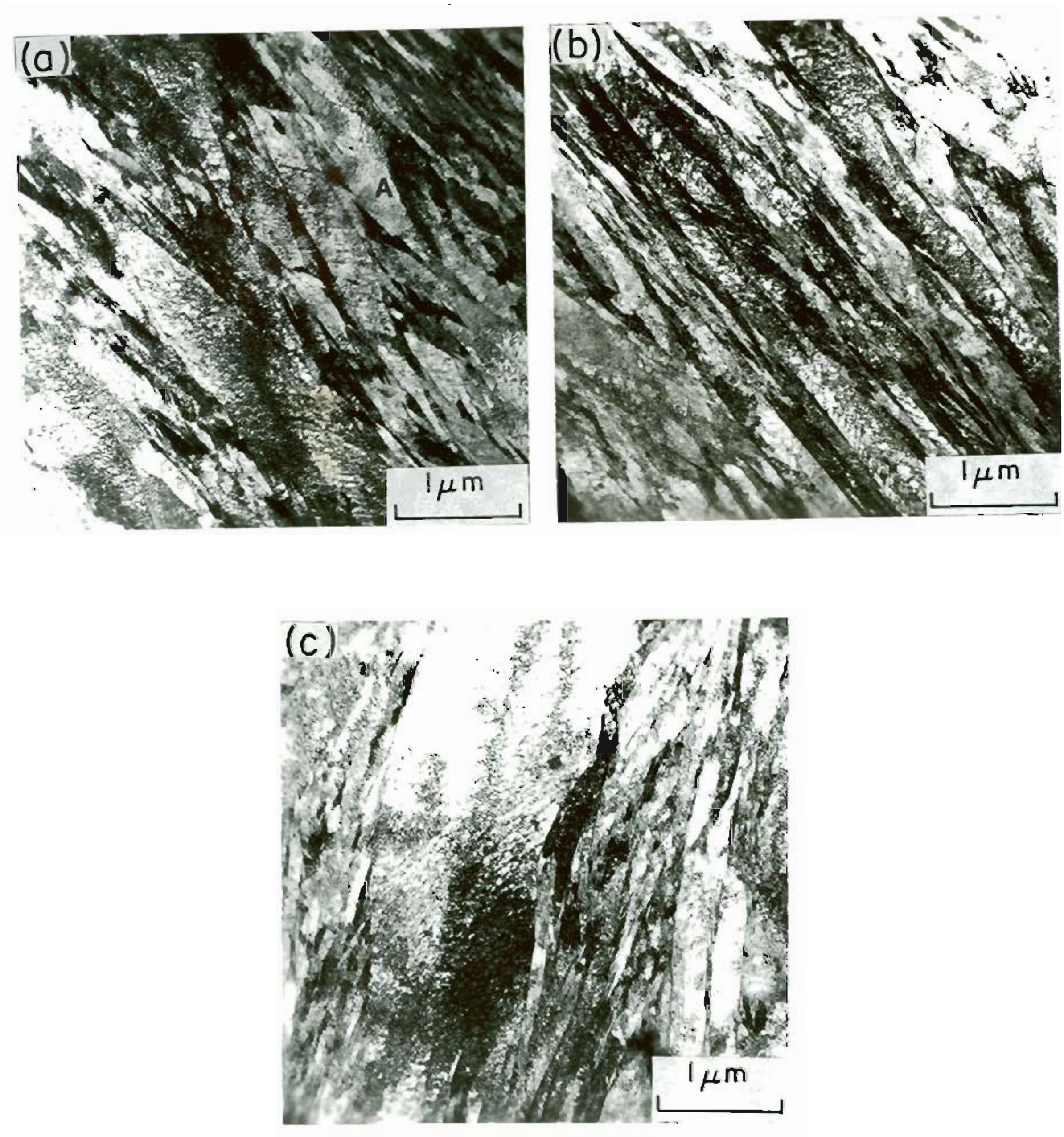

Figure 14. TYPICAL MICROSTRUCTURE OF AISI 4340 STEEL AUSTENITIZED AT 1200°C AND TEMPERED AT 180°C SHOWING LATH MARTENSITE

(a) CONVERGENT LATHS

(b) REGULAR PARALLEL LATHS

(c) LARGE LATH (MICRO TWINS IN THE LATH MARTENSITE IS SHOWN BY ARROW).

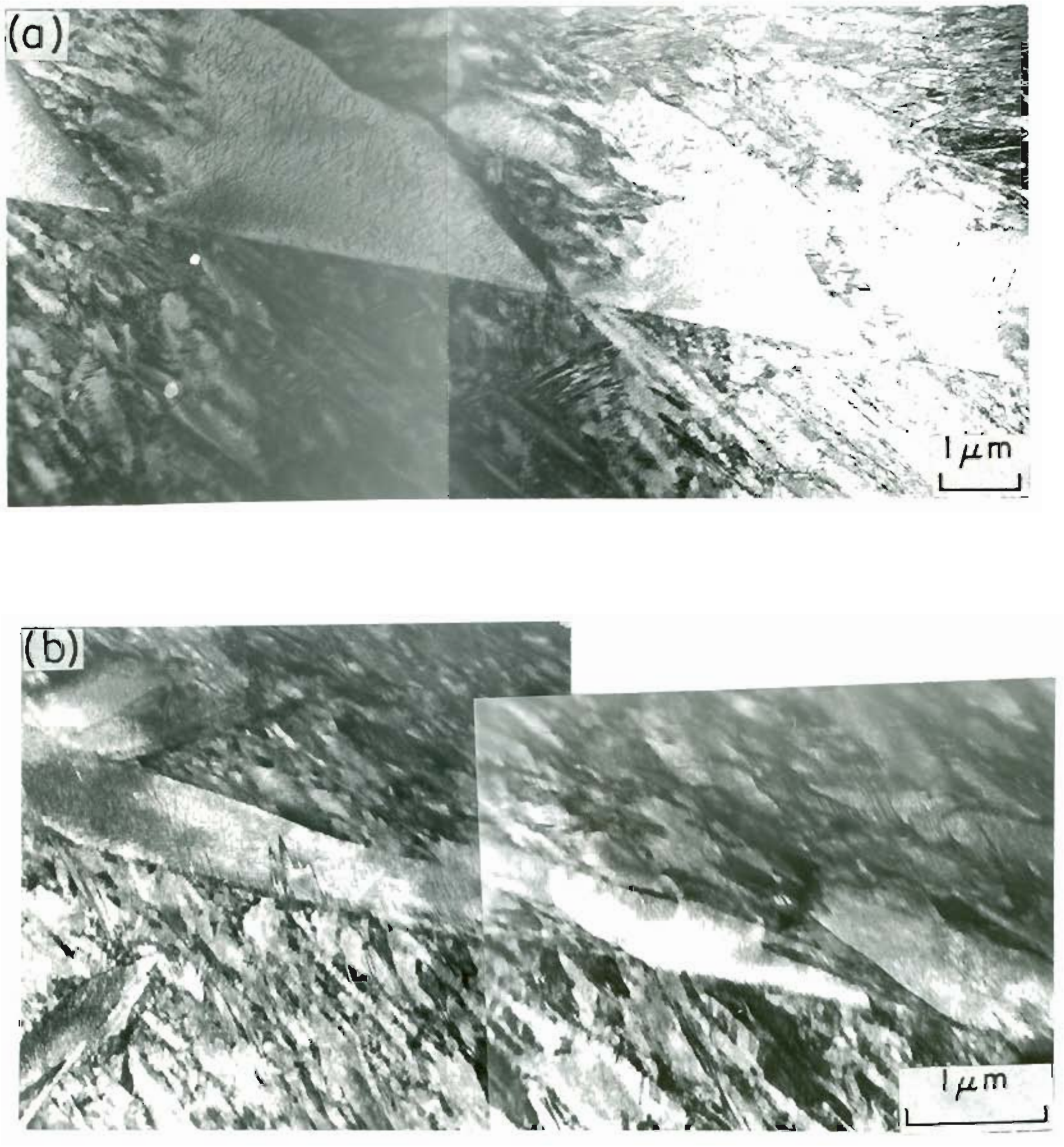

Figure 15. TRANSMISSION ELECTRON MICROGRAPH OF AISI 4340 STEEL SHOWING BLOCKY MARTENSITE AT THE PRIOR AUSTENITE GRAIN BOUNDARIES

(a) AUSTENITIZED AT 1200°C AND TEMPERED AT 280°C

(b) STEP QUENCHED FROM 1200°C TO 870°C AND TEMPERED AT 180°C SHOWING TWINS.

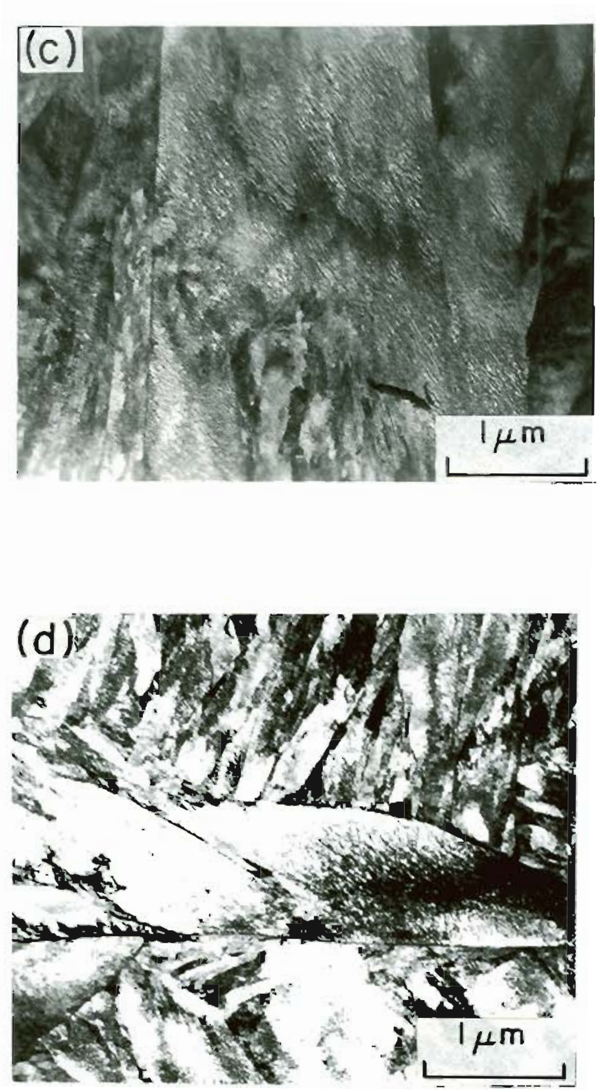

Figure 15. (cont.) TRANSMISSION ELECTRON MICROGRAPH OF AISI 4340 STEEL SHOWING BLOCKY MARTENSITE AT THE PRIOR AUSTENITE GRAIN BOUNDARIES

(c) STEP QUENCHED FROM 1200°C TO 870°C AND TEMPERED AT 180°C SHOWING DISLOCATED MARTENSITE

(d) AUSTENITIZED AT 870°C AND TEMPERED AT 180°C.

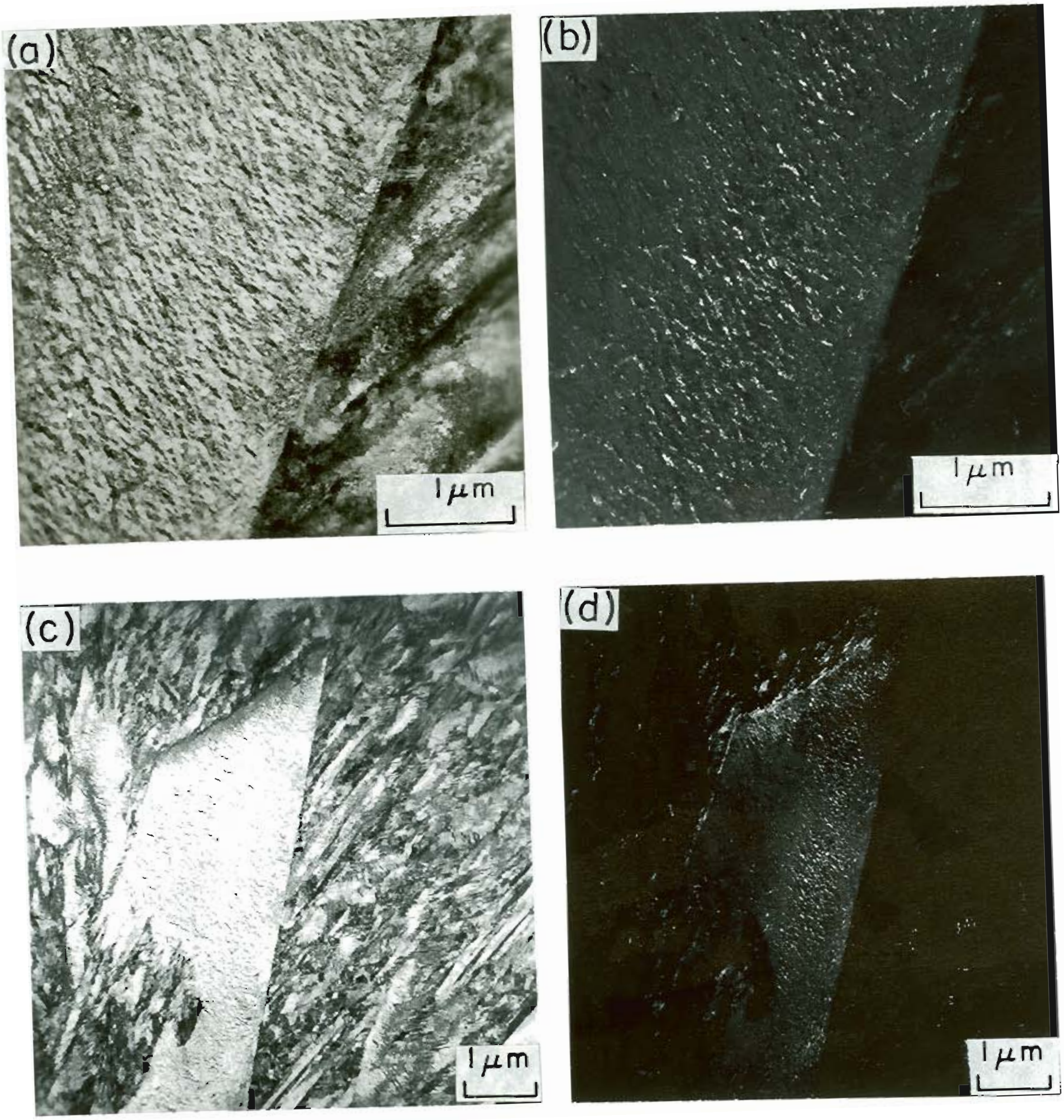

Figure 16. TRANSMISSION ELECTRON MICROGRAPHS OF AISI 4340 STEEL AUSTENITIZED AT 1200°C AND TEMPERED AT 280°C

(a) and (c) BF MICROGRAPH SHOWING DISLOCATED BLOCKY MARTENSITE

(b) and (d) DF MICROGRAPHS SHOWING CEMENTITE IN MORE THAN ONE ORIENTATION. NOTE CEMENTITE ON GRAIN BOUNDARY.

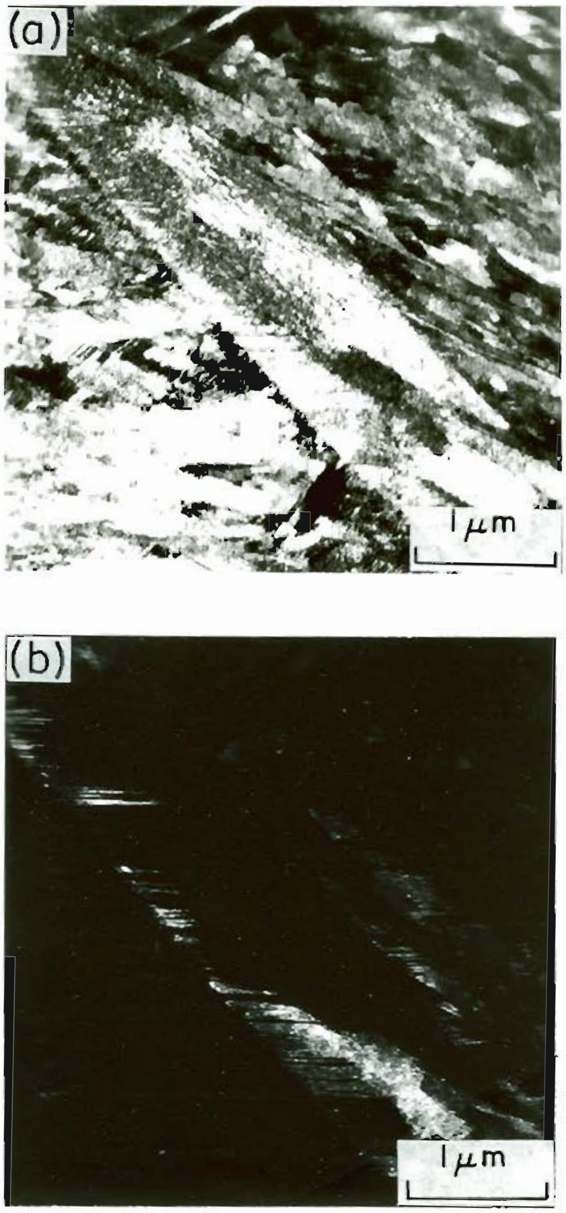

Figure 17. TRANSMISSION ELECTRON MICROGRAPHS OF AISI 4340 STEEL STEP QUENCHED FROM 1200°C TO 870°C AND TEMPERED AT 180°C

(a) BF MICROGRAPH SHOWING TWINS

(b) DF MICROGRAPH.

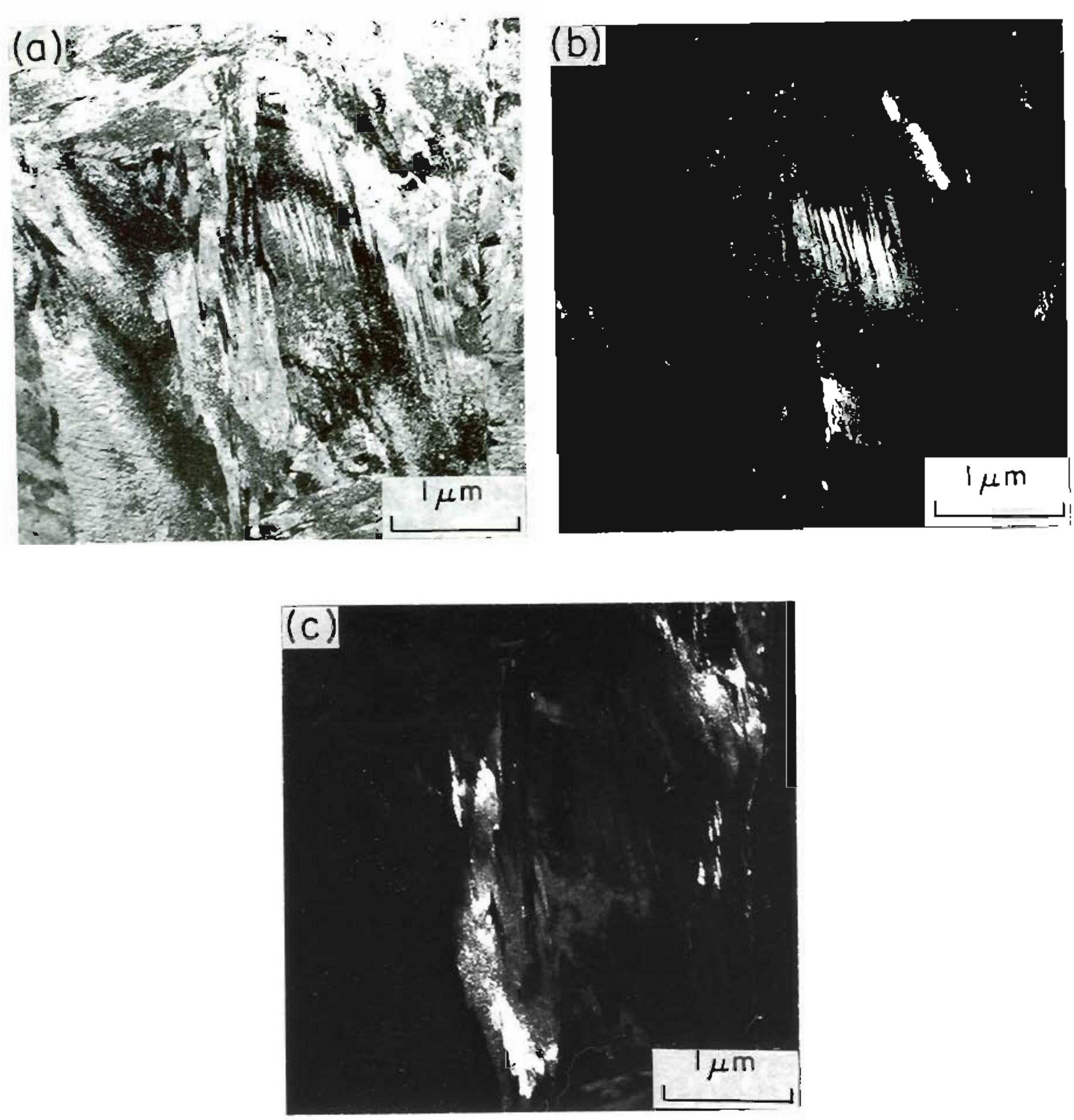

Figure 18. TRANSMISSION ELECTRON MICROGRAPHS OF AISI 4340 STEEL AUSTENITIZED AT 870°C AND TEMPERED AT 180°C SHOWING TWINS IN THE MARTENSITE ADJACENT TO THE PRIOR AUSTENITE GRAIN BOUNDARY

(a) BF MICROGRAPH

(b) and (c) DF MICROGRAPHS SHOWING REVERSAL CONTRAST OF TWINS.

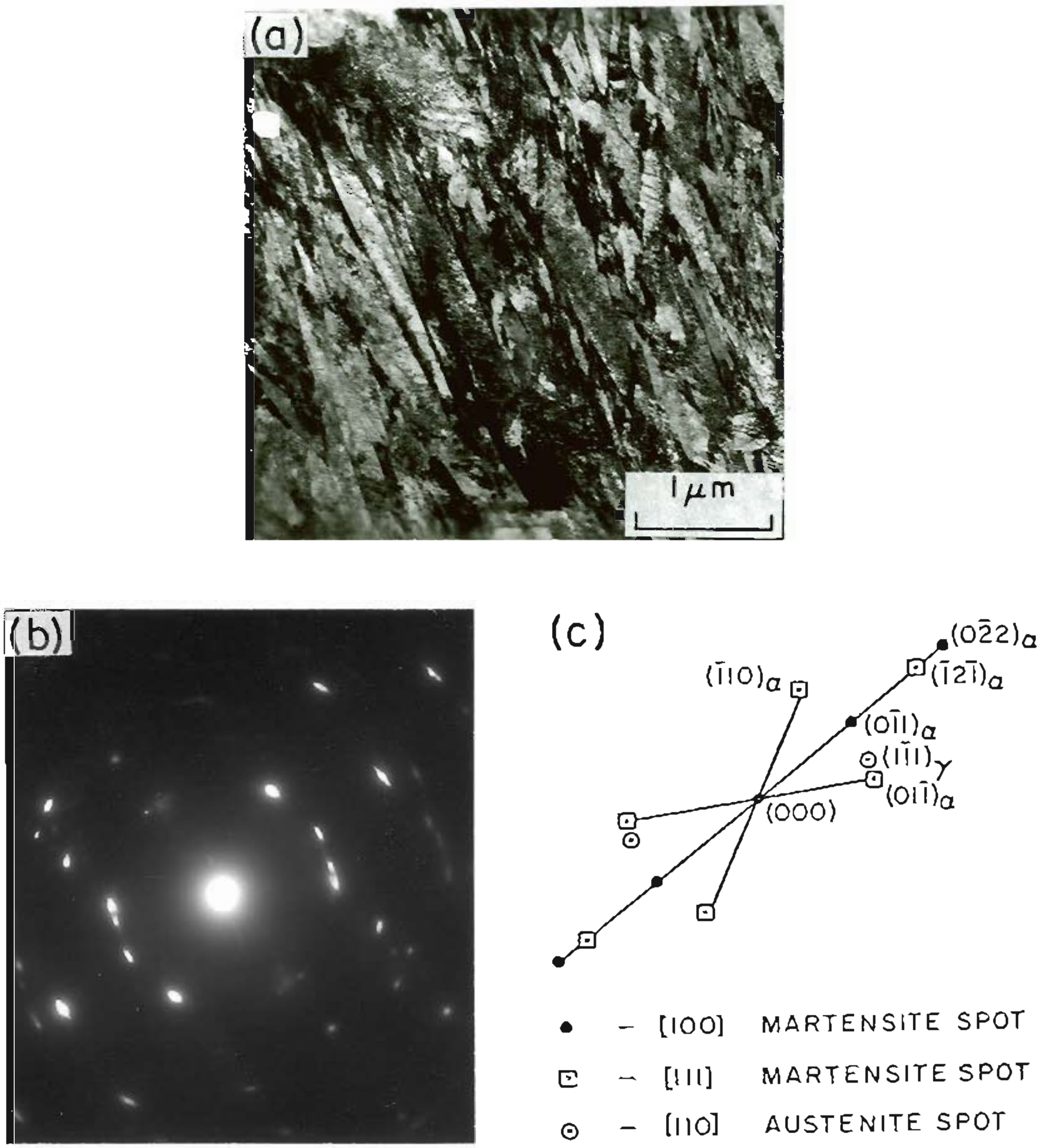

Figure 19. TRANSMISSION ELECTRON MICROGRAPHS OF AISI 4340 STEEL AUSTENITIZED AT 870°C AND TEMPERED AT 180°C

(a) BF MICROGRAPH

(b) SAD PATTERN

(c) SCHEMATIC OF SAD.

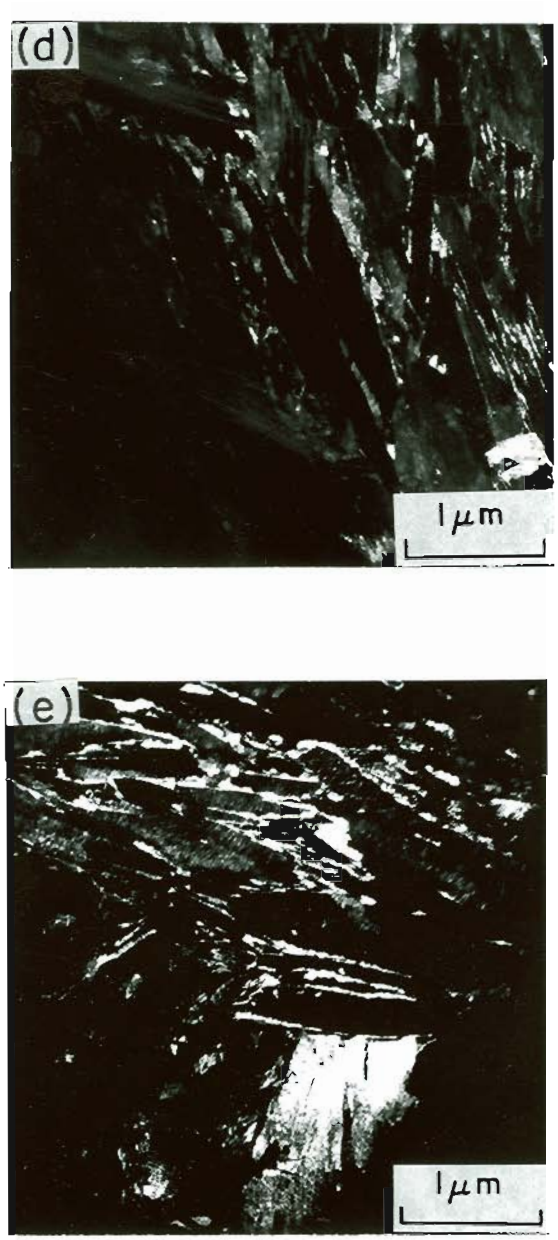

Figure 19. (cont.) TRANSMISSION ELECTRON MICROGRAPHS OF AISI 4340 STEEL AUSTENITIZED AT 870°C AND TEMPERED AT 180°C

(d) DF MICROGRAPH SHOWING A SMALL AMOUNT OF RETAINED AUSTENITE

(e) DF MICROGRAPH OBTAINED FROM DIFFERENT AREA SHOWING INCREASED AMOUNT OF RETAINED AUSTENITE.

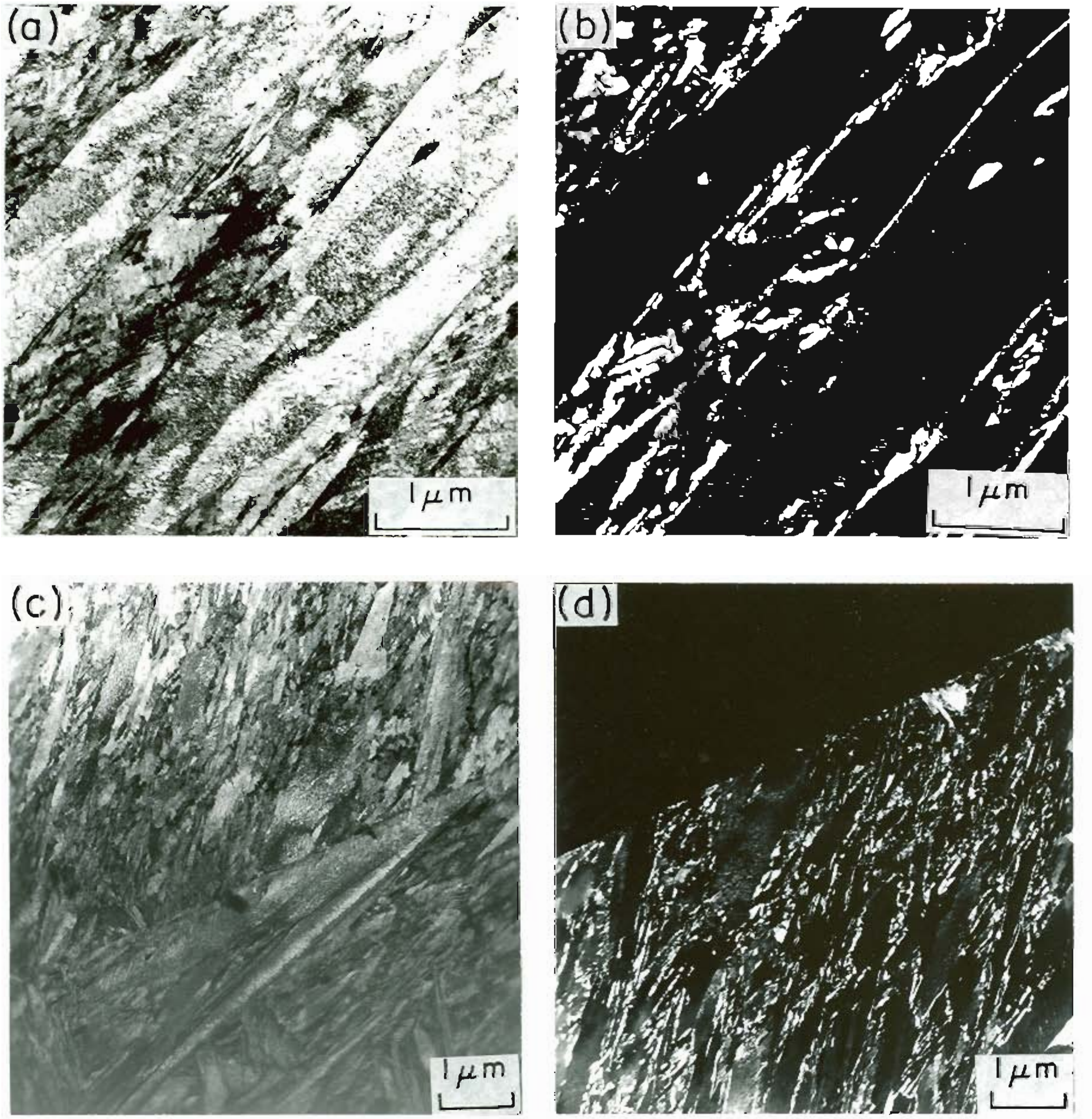

Figure 20. TRANSMISSION ELECTRON MICROGRAPHS OF 4340 STEEL SHOWING THIN FILMS OF RETAINED AUSTENITE AT THE LATH BOUNDARIES

(a) and (b) BF AND DF MICROGRAPHS OBTAINED FROM A SPECIMEN AUSTENITIZED AT 1200°C AND TEMPERED AT 180°C

(c) and (d) BF AND DF MICROGRAPHS OBTAINED FROM STEP QUENCHED SPECIMEN AND TEMPERED AT 180°C.

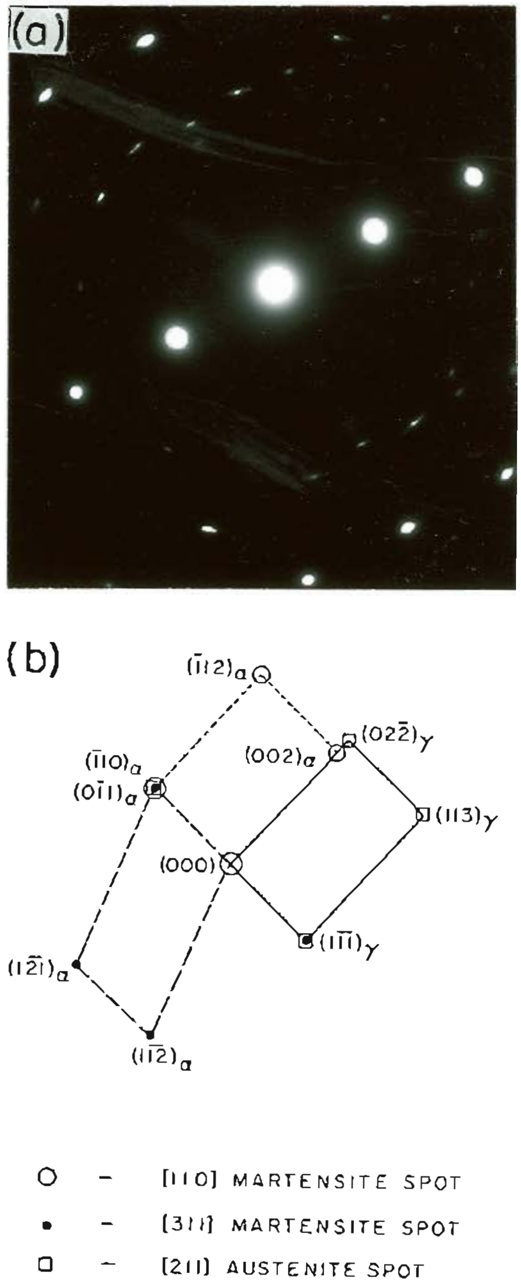

Figure 21. TRANSMISSION ELECTRON MICROGRAPHS OF 4340 STEEL AUSTENITIZED AT 1200°C AND TEMPERED AT 180°C SHOWING N-W ORIENTATION RELATIONSHIP BETWEEN AUSTENITE AND MARTENSITE

(a) SAD PATTERN

(b) SCHEMATIC OF SAD.

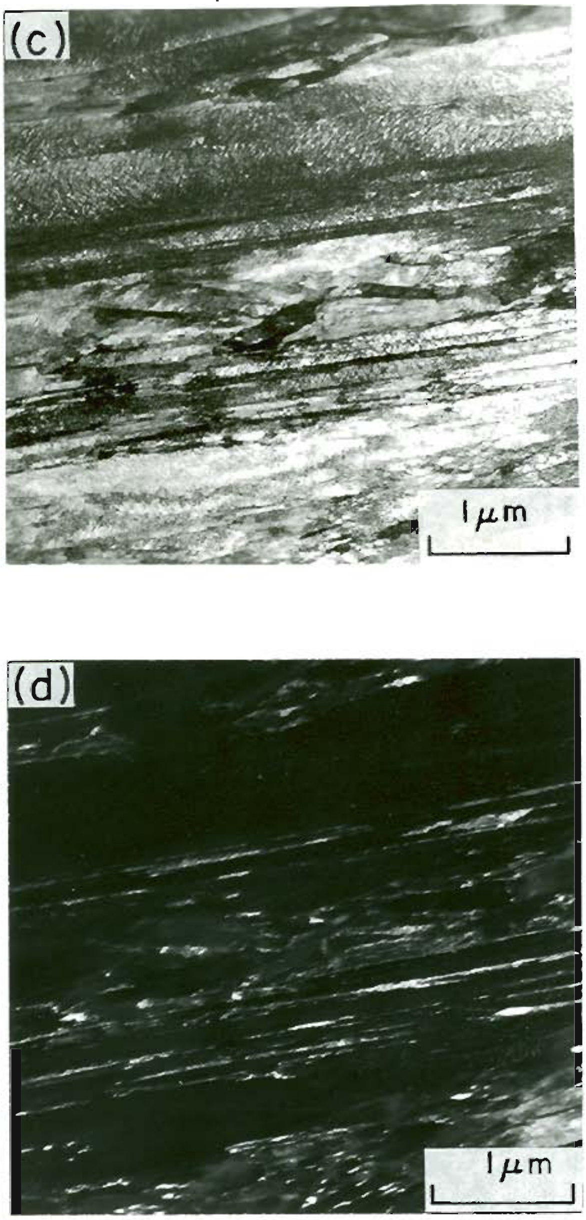

Figure 21. (cont.) TRANSMISSION ELECTRON MICROGRAPHS OF 4340 STEEL AUSTENITIZED AT 1200°C AND TEMPERED AT 180°C SHOWING N-W ORIENTATION RELATIONSHIP BETWEEN AUSTENITE AND MARTENSITE

(c) BF MICROGRAPH

(d) DF MICROGRAPH SHOWING LATH BOUNDARY RETAINED AUSTENITE.

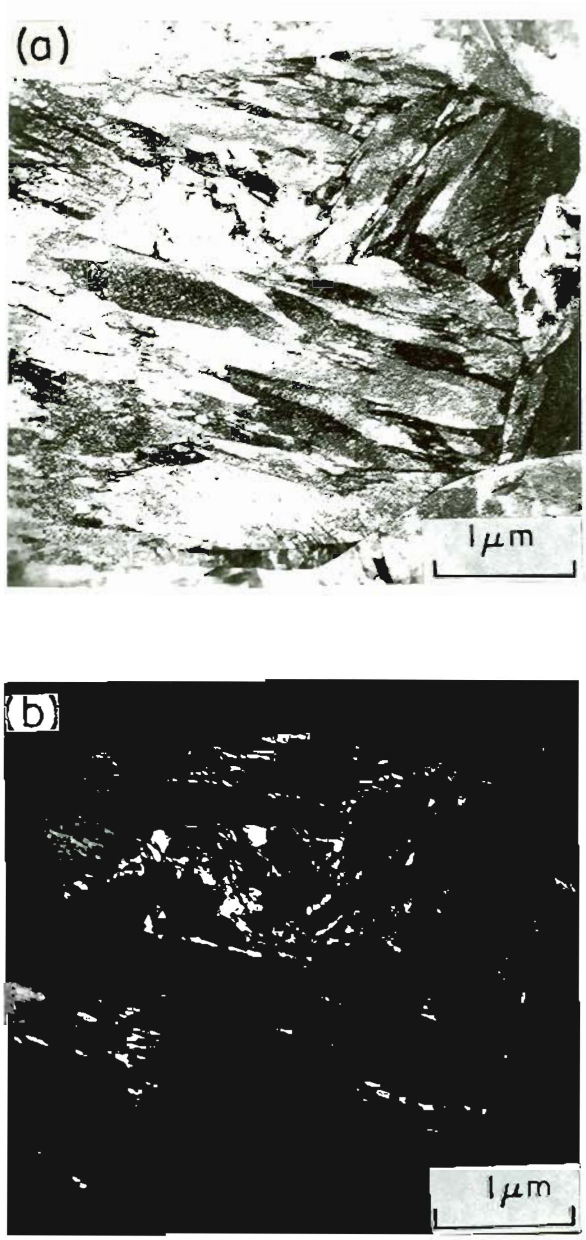

Figure 22. TRANSMISSION ELECTRON MICROGRAPHS OF 4340 STEEL AUSTENITIZED AT 870°C AND TEMPERED AT 180°C

(a) BF MICROGRAPH SHOWING PRIOR AUSTENITE G.B.

(b) DF MICROGRAPH SHOWING RETAINED AUSTENITE.

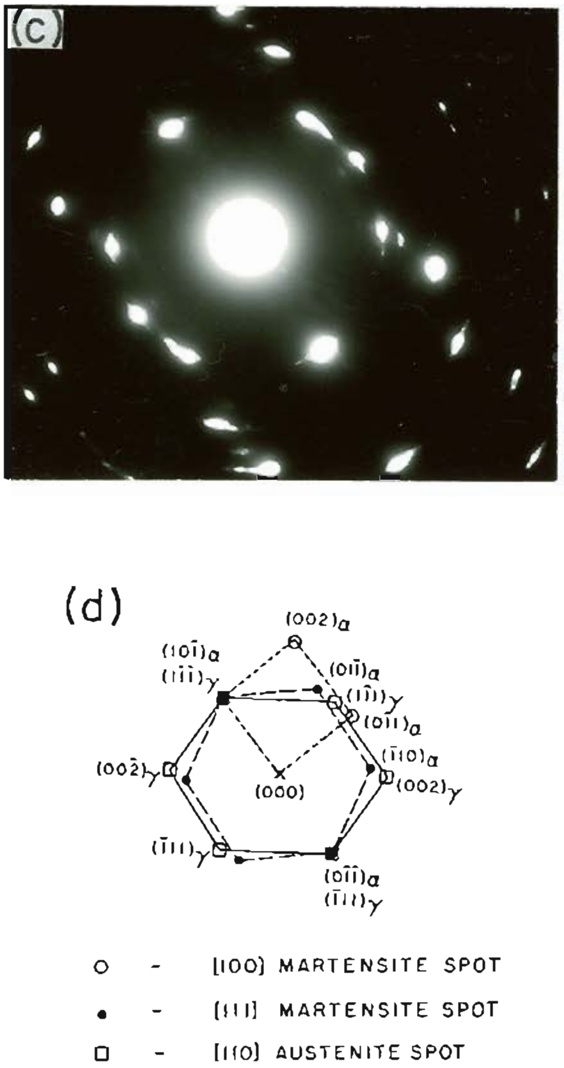

Figure 22. TRANSMISSION ELECTRON MICROGRAPHS OF 4340 STEEL
(cont.) AUSTENITIZED AT 870°C AND TEMPERED AT 180°C

(c) SAD PATTERN

(d) SCHEMATIC OF SAD.

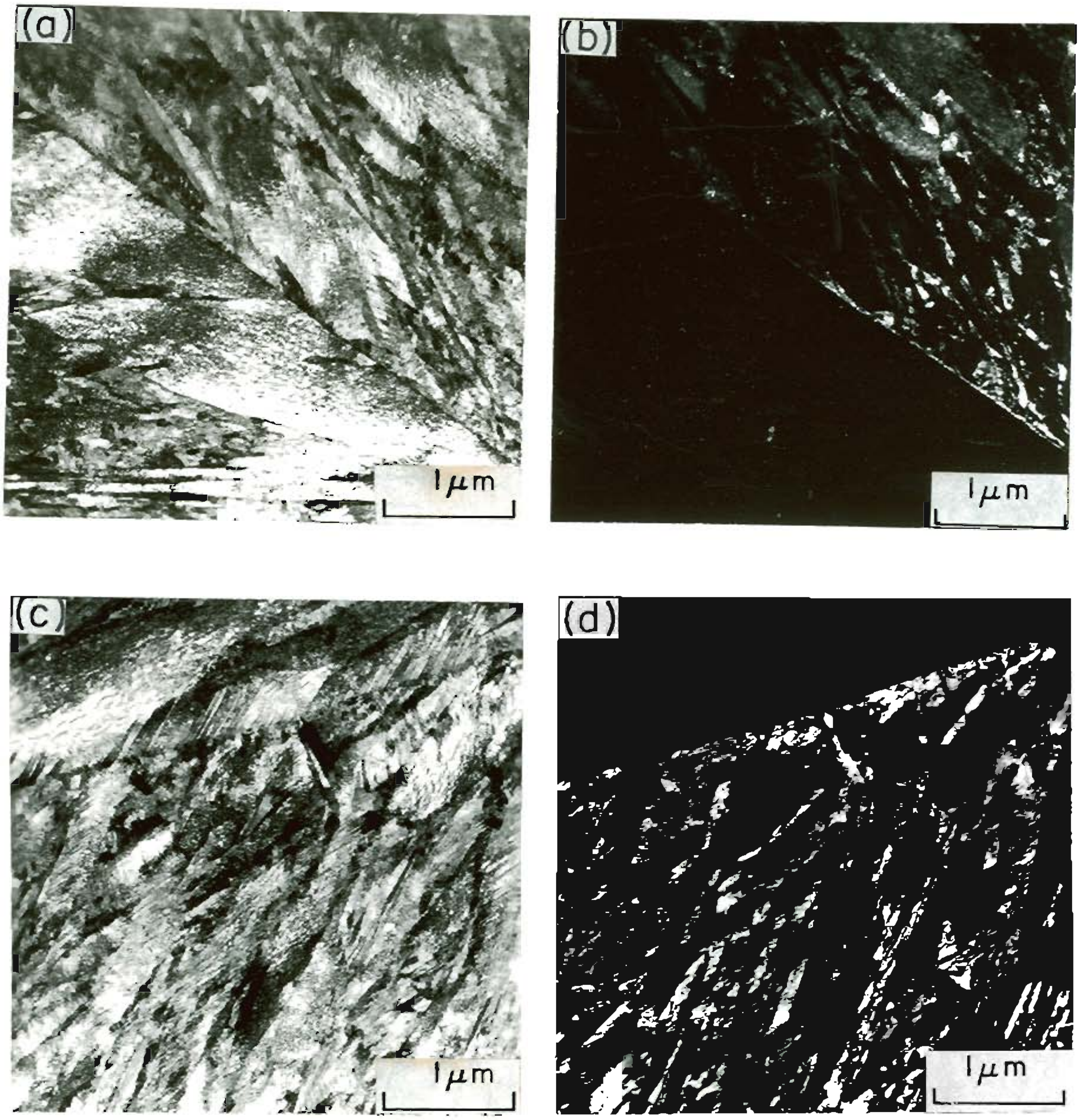

Figure 23. TRANSMISSION ELECTRON MICROGRAPHS OF AISI 4340 STEEL SHOWING THIN FILMS OF RETAINED AUSTENITE AT THE PRIOR AUSTENITE GRAIN BOUNDARIES

(a) and (b) BF AND DF MICROGRAPHS OBTAINED FROM A SPECIMEN AUSTENITIZED AT 1200°C AND TEMPERED AT 180°C

(c) and (d) BF AND DF MICROGRAPHS OF STEP QUENCHED AND TEMPERED AT 180°C SPECIMEN.

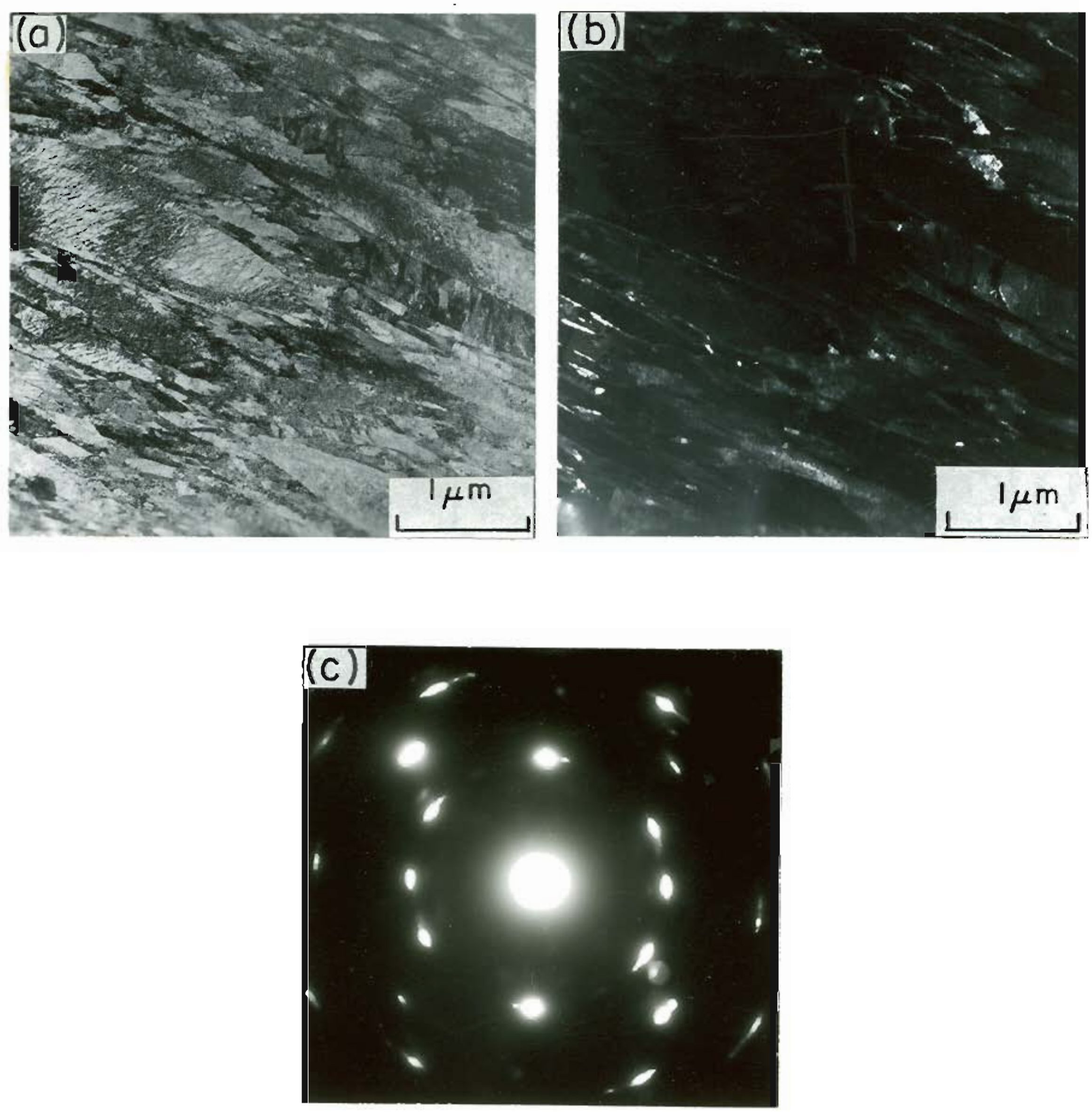

Figure 24. TRANSMISSION ELECTRON MICROGRAPHS OF 4340 STEEL AUSTENITIZED AT 1200°C AND TEMPERED AT 180°C SHOWING SMALL AMOUNT OF RETAINED AUSTENITE WITHIN THE PLASTIC ZONE AHEAD OF A CRACK TIP

(a) BF

(b) DARK FIELD SHOWING SMALL AMOUNTS OF RETAINED AUSTENITE

(c) SAD.

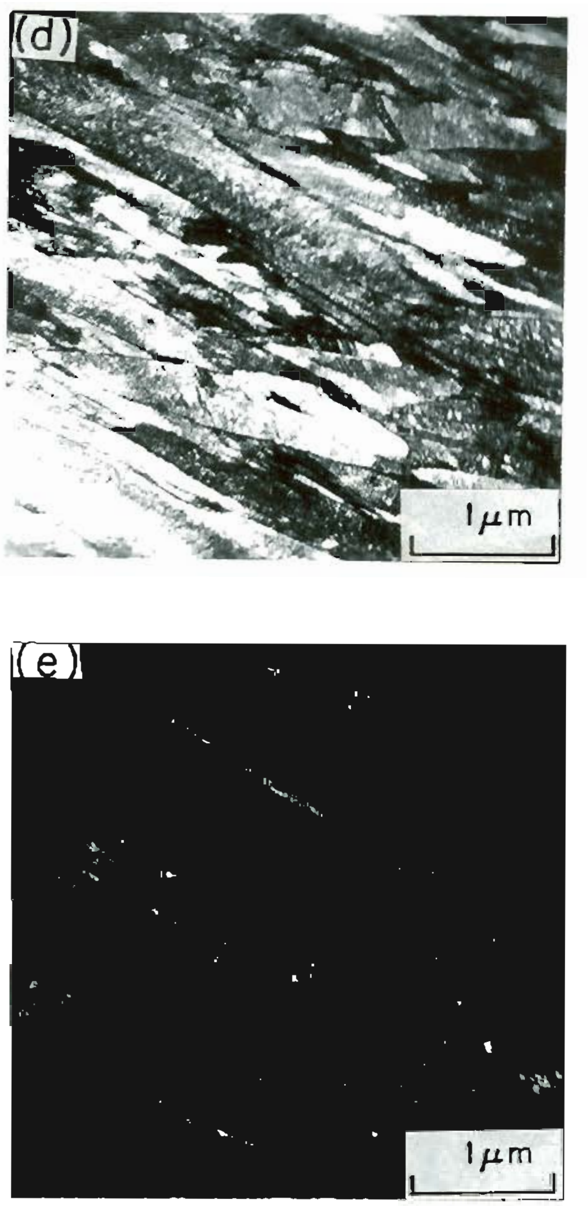

Figure 24. (cont.) TRANSMISSION ELECTRON MICROGRAPHS OF 4340 STEEL AUSTENITIZED AT 1200°C AND TEMPERED AT 180°C SHOWING SMALL AMOUNT OF RETAINED AUSTENITE WITHIN THE PLASTIC ZONE AHEAD OF A CRACK TIP

(d) BF

(e) CORRESPONDING DF SHOWING DISCONTINUOUS FILMS OF RETAINED AUSTENITE.

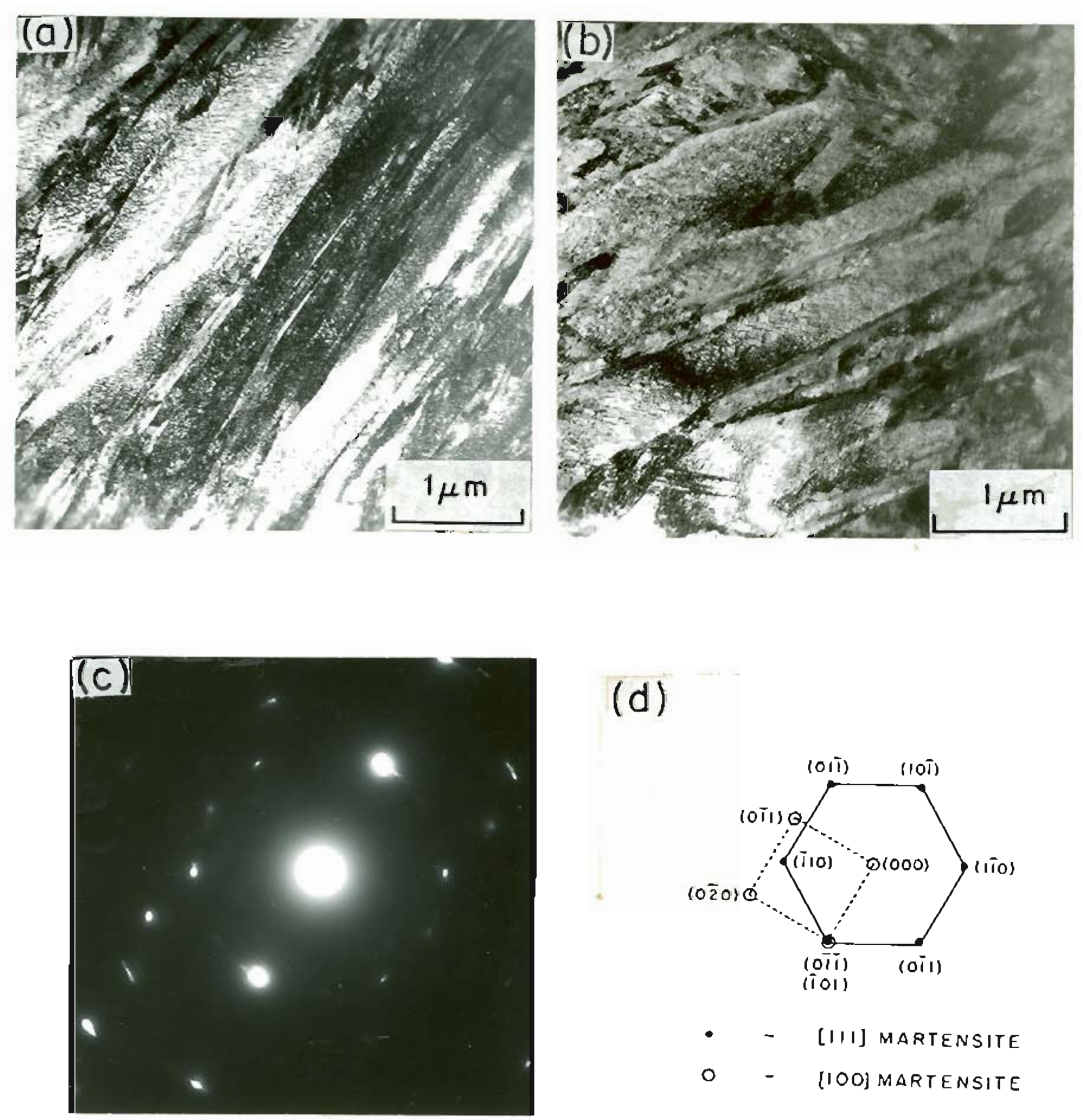

Figure 25. TRANSMISSION ELECTRON MICROGRAPH OF AISI 4340 STEEL AUSTENITIZED AT 1200°C AND TEMPERED AT 180°C SHOWING THE REGIONS WITHOUT RETAINED AUSTENITE WITHIN THE PLASTIC ZONE

(a) BF MICROGRAPH (b) BF MICROGRAPH

(c) SAD (d) SCHEMATIC OF SAD.

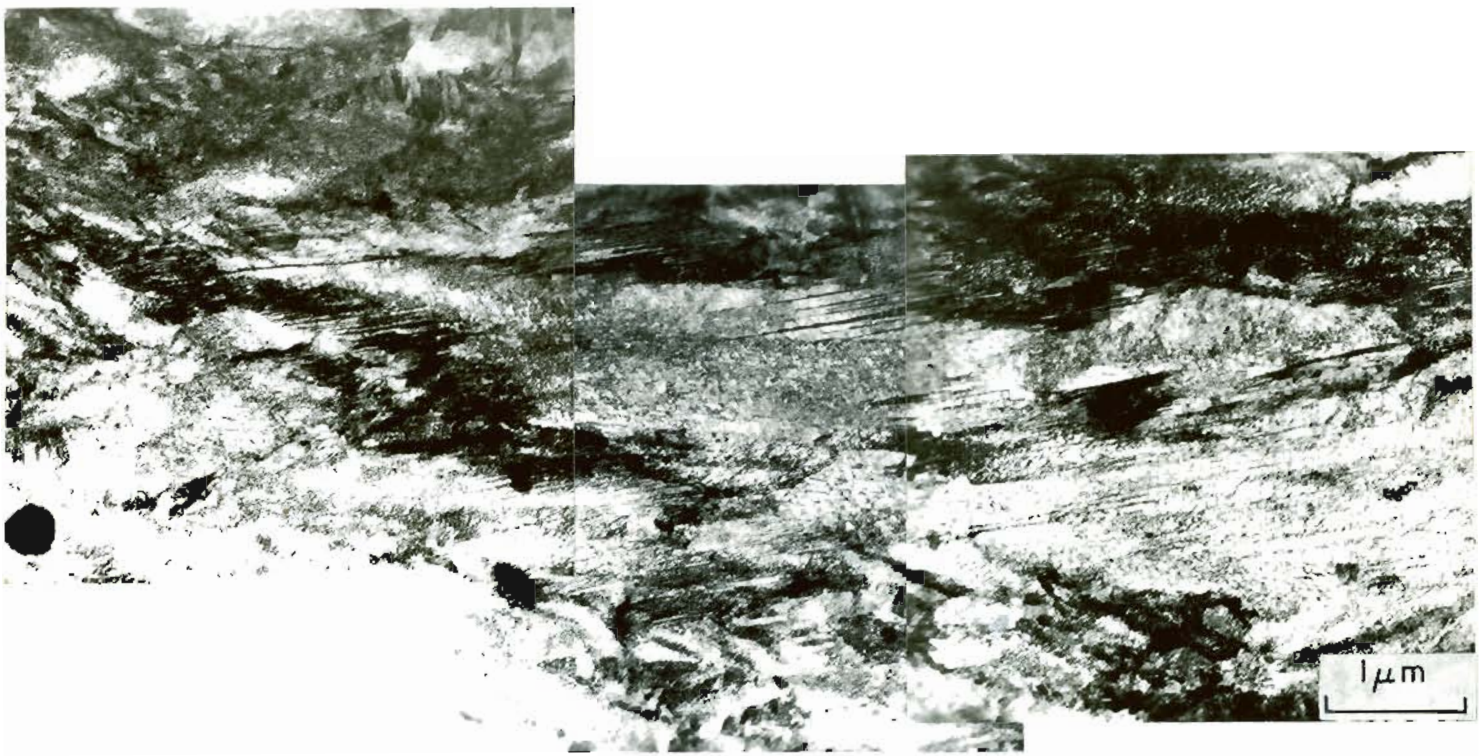

Figure 26. TRANSMISSION ELECTRON MICROGRAPHS OF 4340 STEEL AUSTENITIZED AT 1200°C AND TEMPERED AT 180°C SHOWING EXTENSIVE TWINNING WITHIN THE PLASTIC ZONE AHEAD OF CRACK TIP.

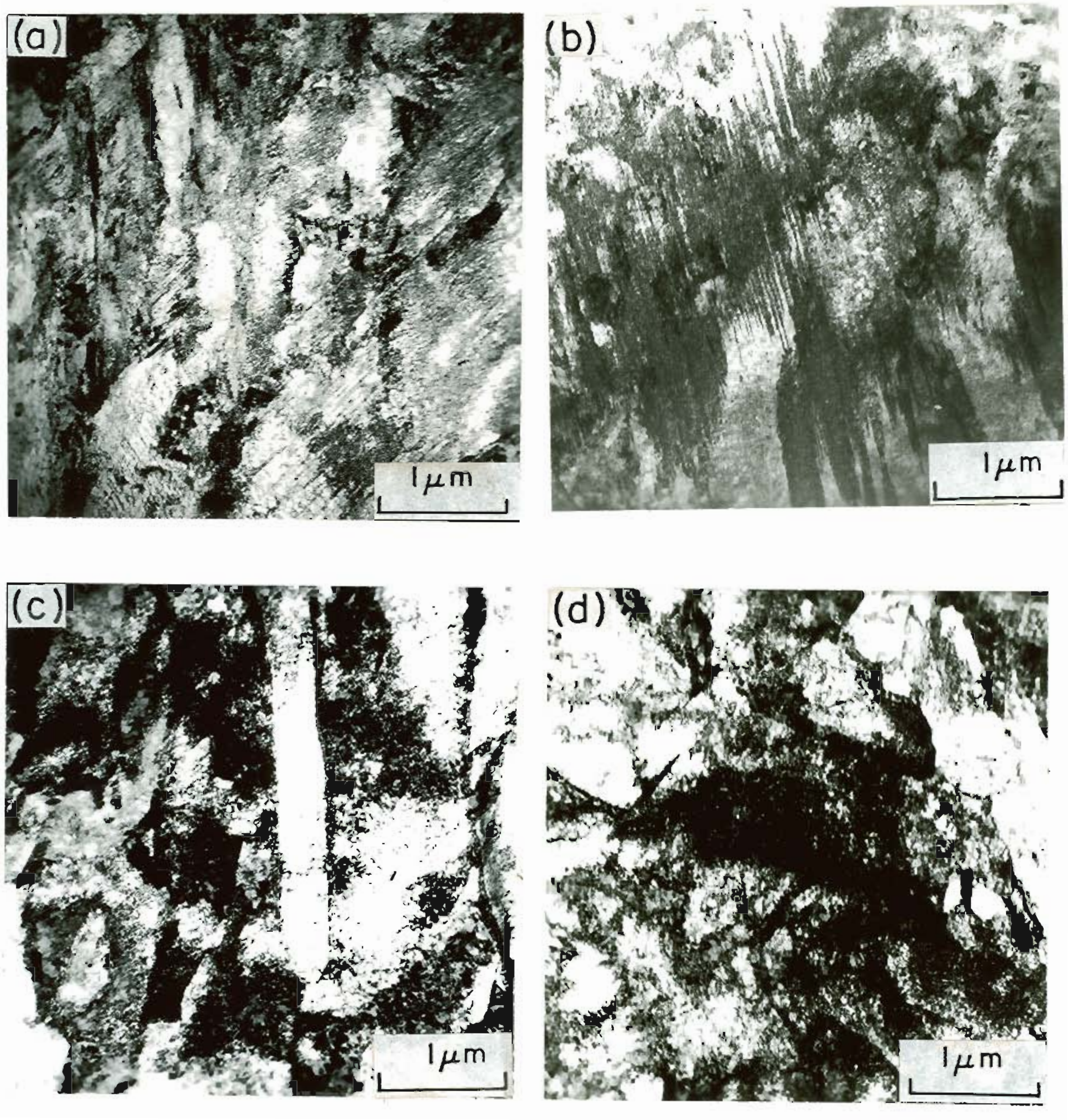

Figure 27. TRANSMISSION ELECTRON MICROGRAPHS OF 4340 STEEL AUSTENITIZED AT 1200°C AND TEMPERED AT 180°C

(a) and (b) THE REGION DEFORMED UNDER PLANE STRAIN CONDITIONS SHOWING EXTENSIVE DISLOCATION NETWORKS AND TWINS

(c) and (d) DEFORMED UNDER PLANE STRESS CONDITION SHOWING ONLY EXTENSIVE DISLOCATION NETWORKS.

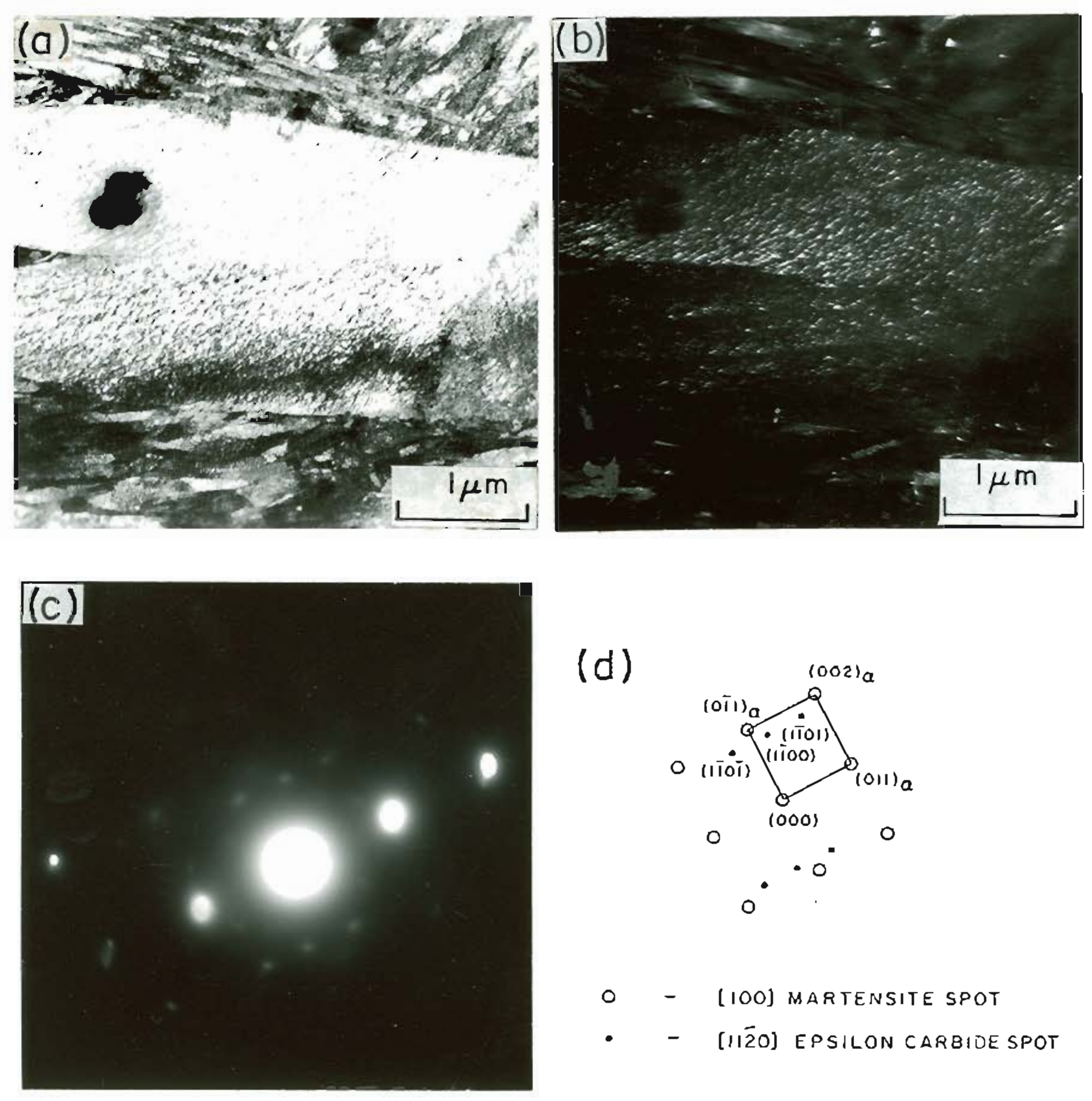

Figure 28. TRANSMISSION ELECTRON MICROGRAPHS OF 4340 STEEL AUSTENITIZED AT 1200°C AND TEMPERED AT 180°C SHOWING EPSILON CARBIDE

(a) BF MICROGRAPH (b) DF MICROGRAPH

(c) SAD PATTERN (d) SCHEMATIC OF SAD.

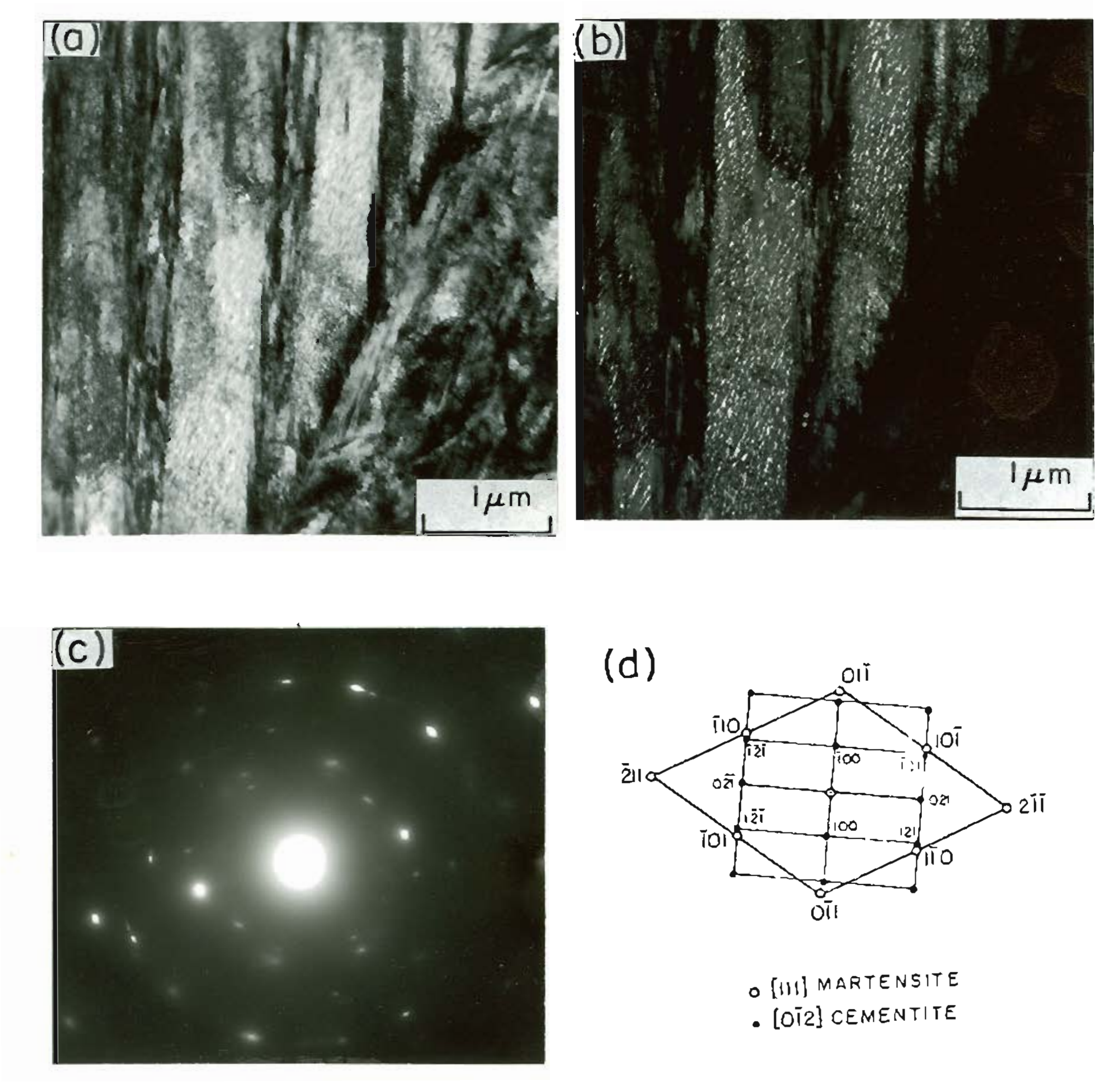

Figure 29. TRANSMISSION ELECTRON MICROGRAPHS OF AISI 4340 STEEL AUSTENITIZED AT 1200°C AND TEMPERED AT 280°C SHOWING CEMENTITE INSIDE THE LATH

(a) BF MICROGRAPH

(b) DF MICROGRAPH USING CEMENTITE SPOT

(c) SAD PATTERN (d) SCHEMATIC OF SAD.

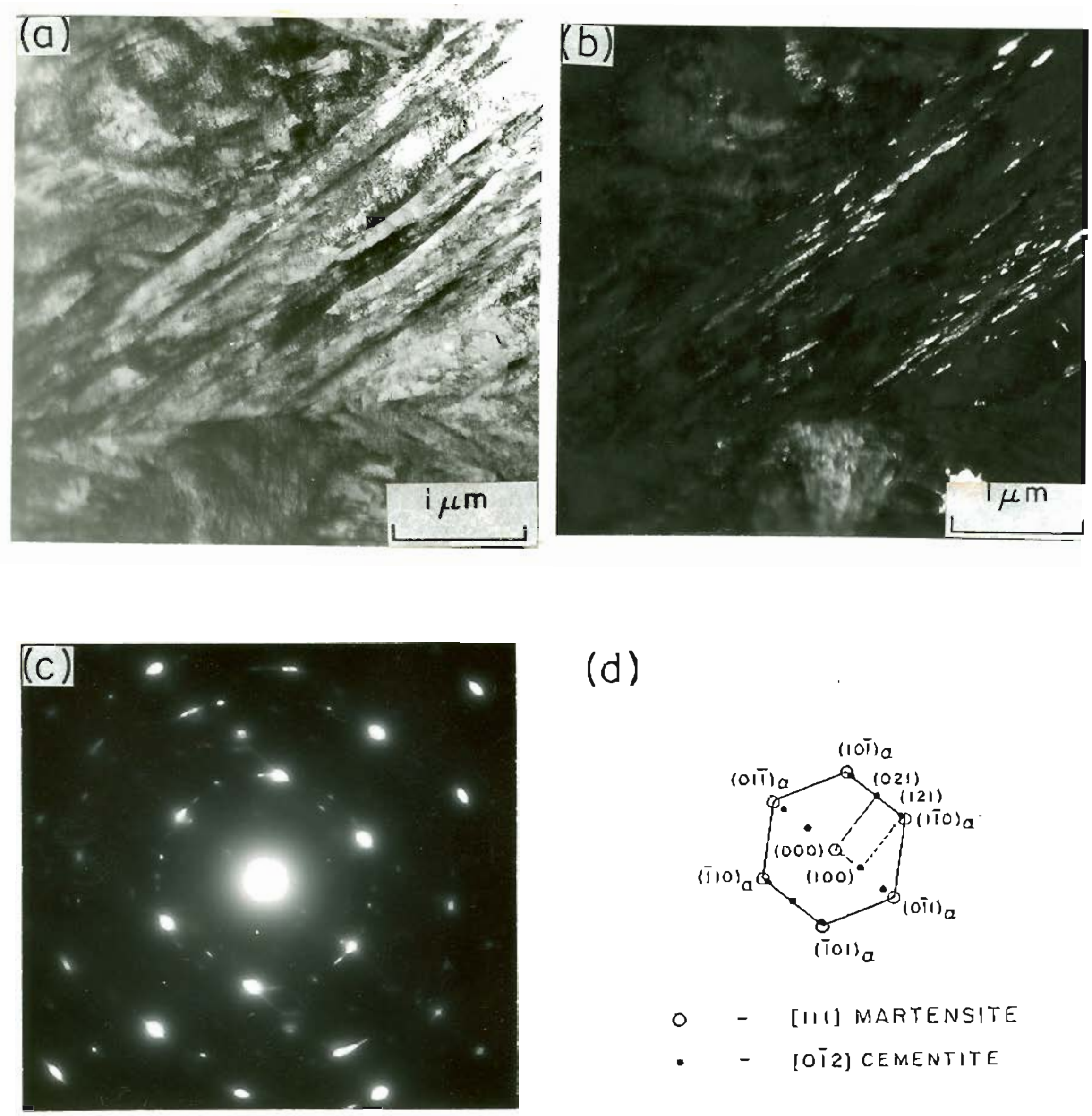

Figure 30. TRANSMISSION ELECTRON MICROGRAPHS OF 4340 STEEL AUSTENITIZED AT 1200°C AND TEMPERED AT 280°C SHOWING CEMENTITE AT THE LATH AND GRAIN BOUNDARIES

(a) BF MICROGRAPH

(b) DF MICROGRAPH SHOWING CEMENTITE ON LATH AND PRIOR AUSTENITE GRAIN BOUNDARY

(c) SAD (d) SCHEMATIC OF SAD.

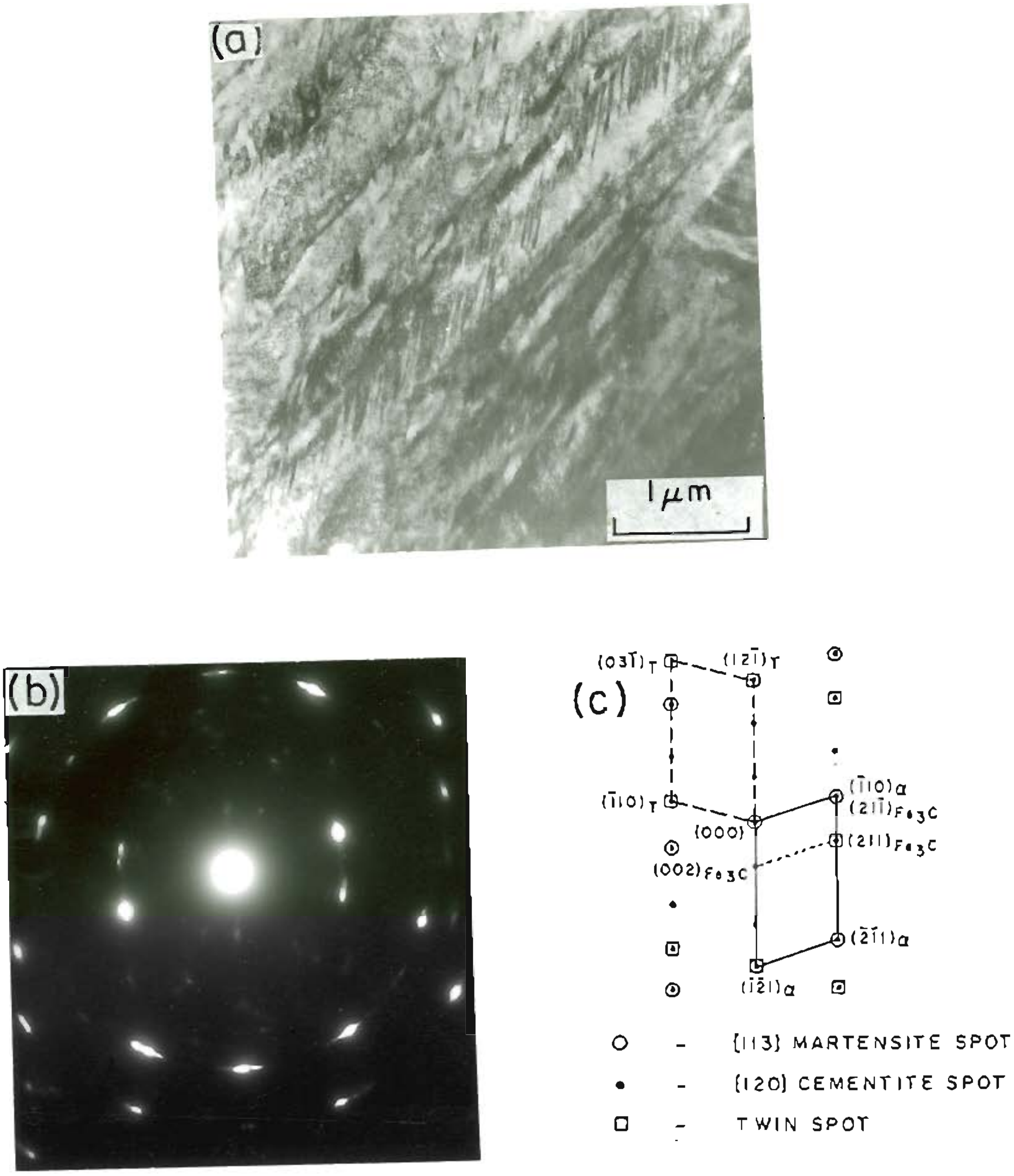

Figure 31. TRANSMISSION ELECTRON MICROGRAPHS OF 4340 STEEL AUSTENITIZED AT 1100°C AND TEMPERED AT 280°C SHOWING CEMENTITE AT THE LATH BOUNDARIES AND ON TWINS

(a) BF MICROGRAPH

(b) SAD

(c) SCHEMATIC OF SAD.

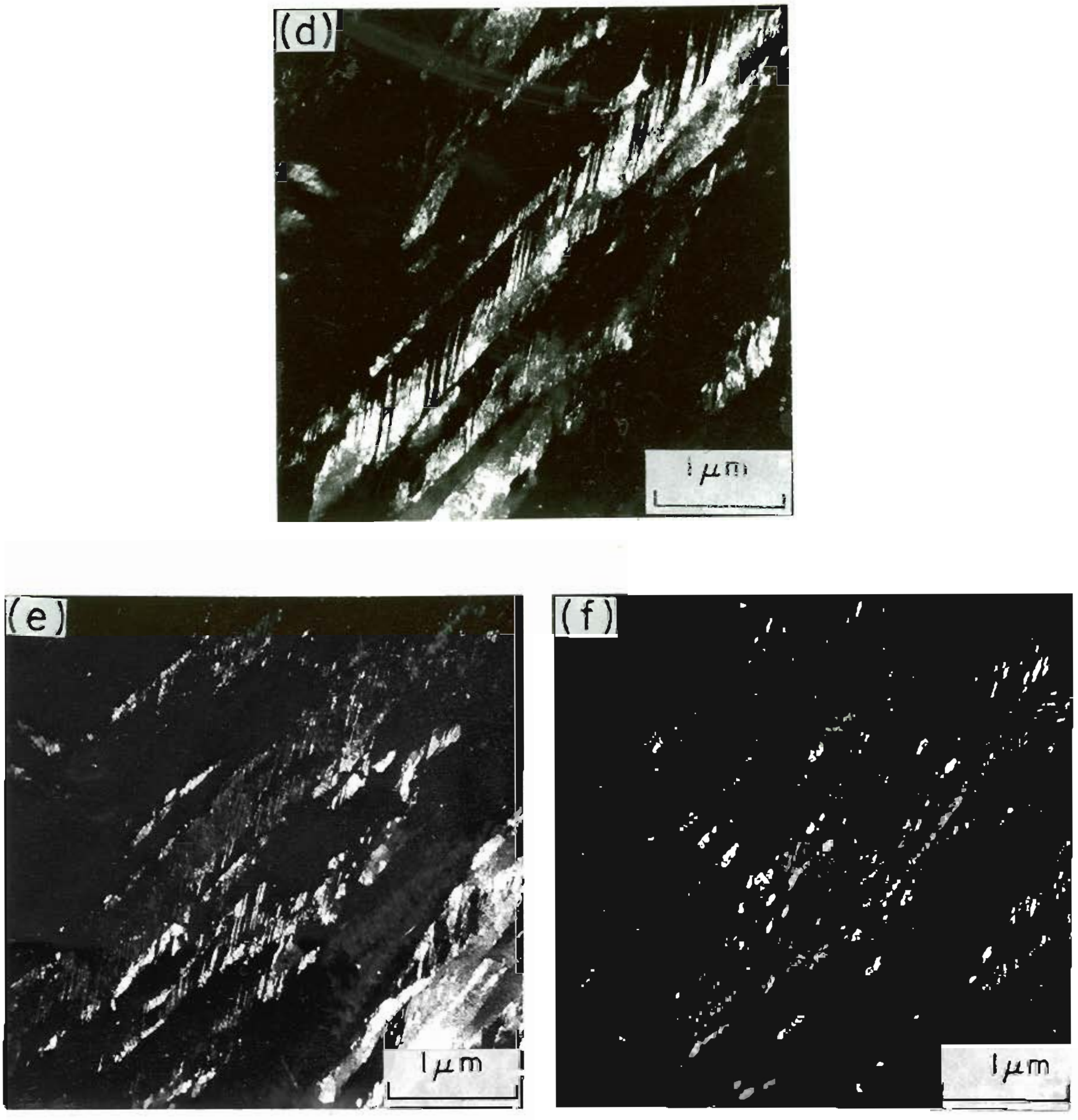

Figure 31. (cont.) TRANSMISSION ELECTRON MICROGRAPHS OF 4340 STEEL AUSTENITIZED AT 1100°C AND TEMPERED AT 280°C SHOWING CEMENTITE AT THE LATH BOUNDARIES AND ON TWINS

(d) DF MICROGRAPH USING MATRIX SPOT

(e) DF MICROGRAPH USING TWIN SPOT

(f) DF MICROGRAPH USING CARBIDE SPOT.

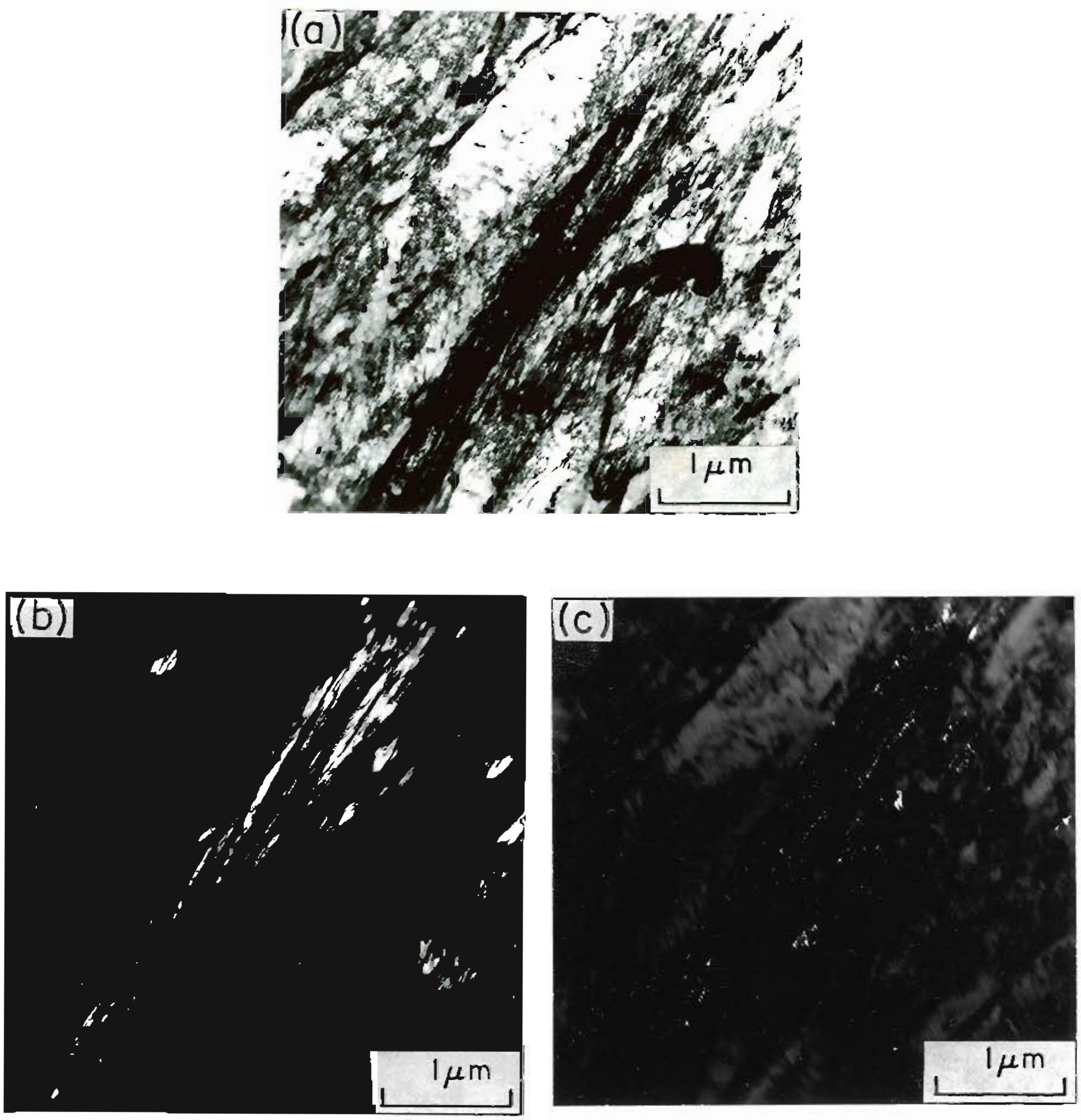

Figure 32. TRANSMISSION ELECTRON MICROGRAPHS OF 4340 STEEL AUSTENITIZED AT 1200°C AND TEMPERED AT 280°C SHOWING CEMENTITE ON TWINS

(a) BF MICROGRAPHS

(b) DF MICROGRAPH USING TWIN SPOT

(c) DF MICROGRAPH USING CARBIDE SPOT.

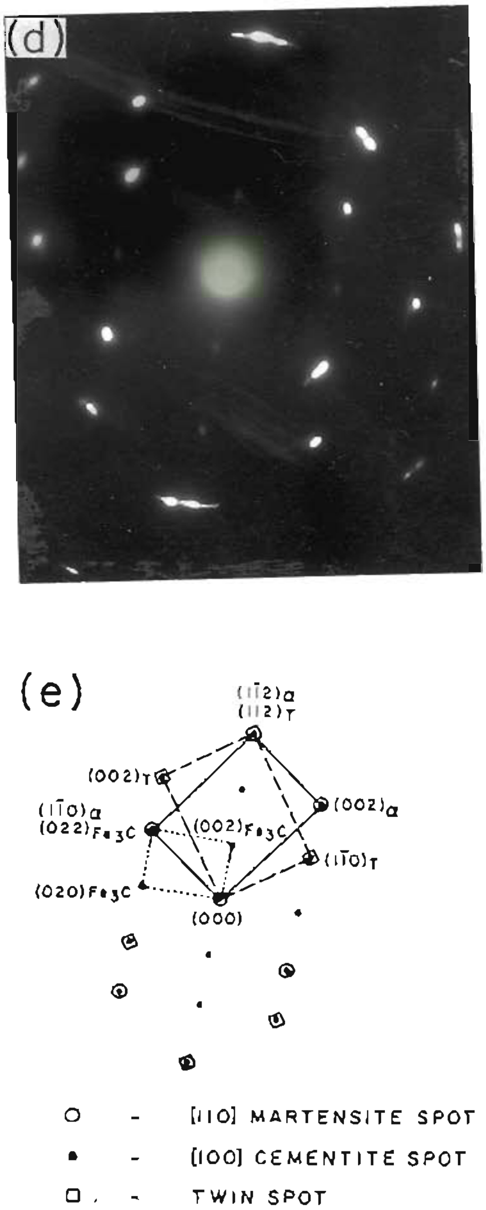

Figure 32. (cont.) TRANSMISSION ELECTRON MICROGRAPHS OF 4340 STEEL AUSTENITIZED AT 1200°C AND TEMPERED AT 280°C SHOWING CEMENTITE ON TWINS

(d) SAD PATTERN

(e) SCHEMATIC OF SAD.

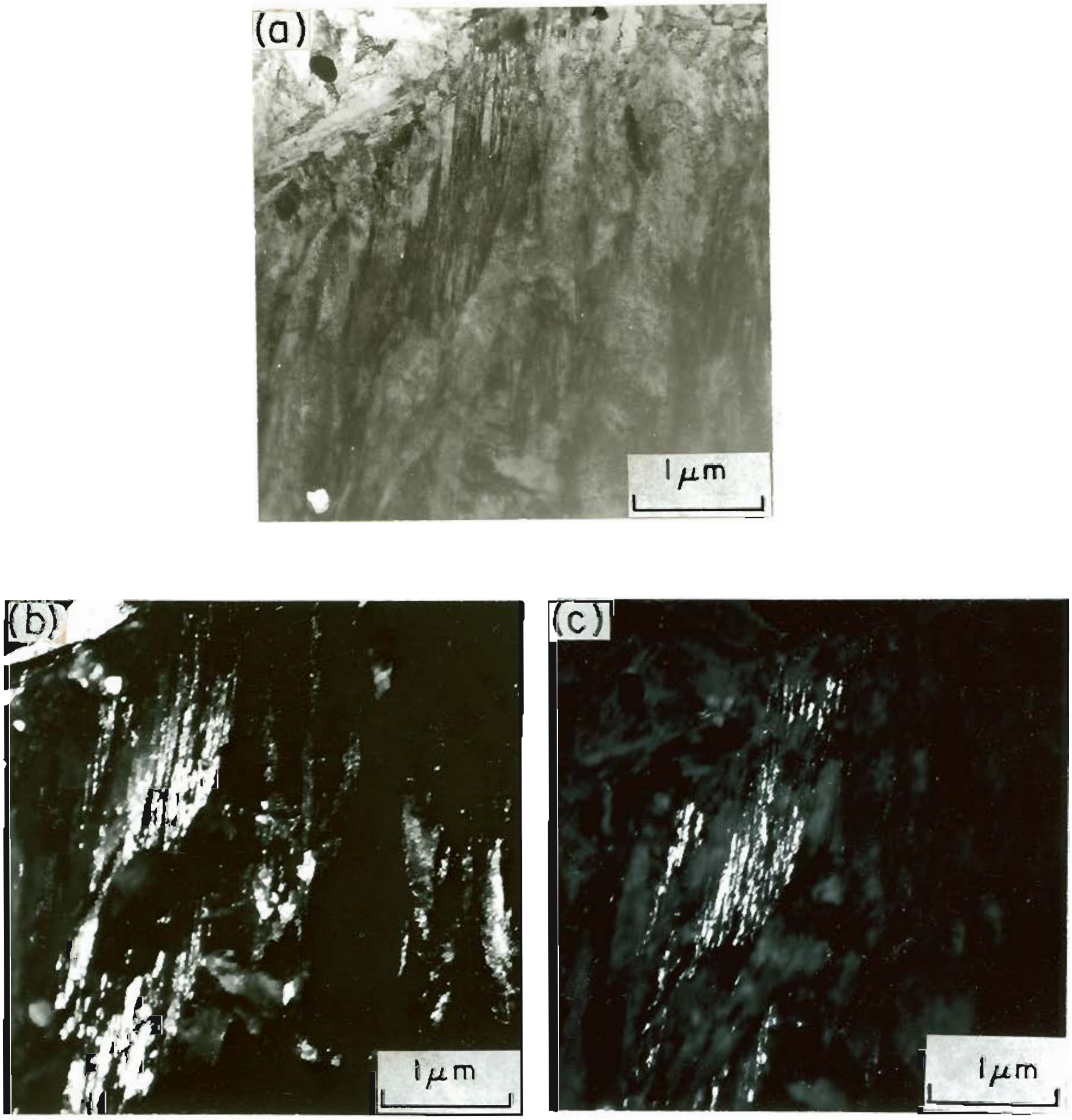

Figure 33. TRANSMISSION ELECTRON MICROGRAPHS OF 4340 STEEL AUSTENITIZED AT 870°C AND TEMPERED AT 280°C SHOWING CEMENTITE ON TWINS

(a) BF MICROGRAPH

(b) DF MICROGRAPH USING TWIN SPOT

(c) DF MICROGRAPH USING CEMENTITE SPOT.

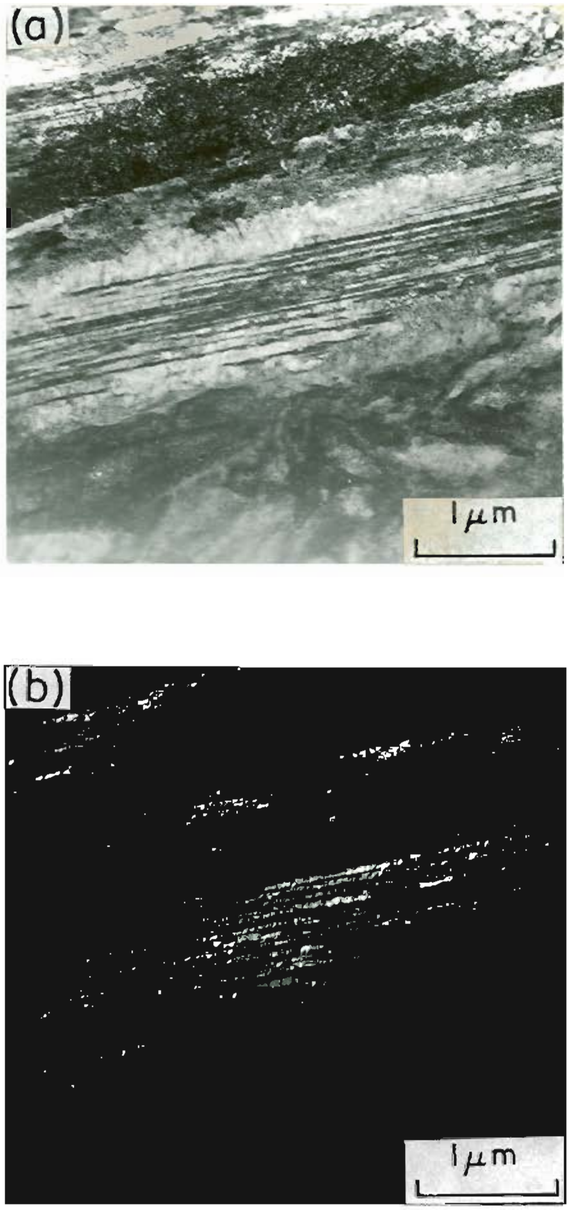

Figure 34. TRANSMISSION ELECTRON MICROGRAPHS OF 4340 STEEL STEP QUENCHED AND TEMPERED AT 280°C SHOWING CEMENTITE ON TWINS

(a) BF MICROGRAPH

(b) DF MICROGRAPH USING CEMENTITE SPOT.

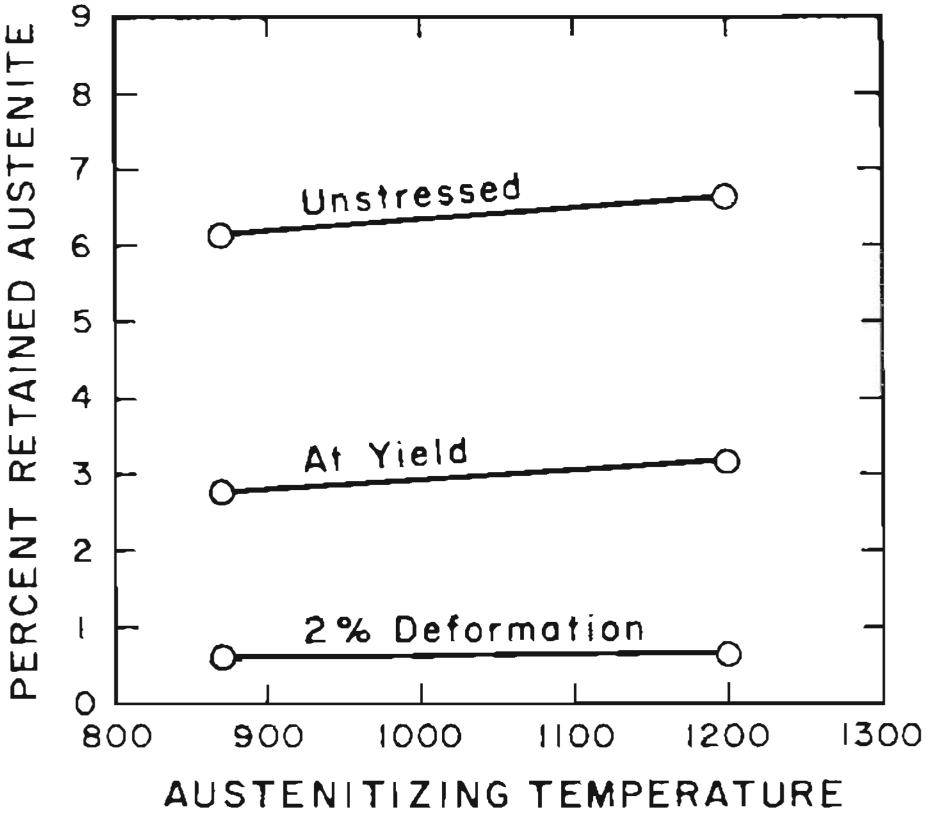

Figure 35. MAGNETIC SATURATION ANALYSIS SHOWING THE VARIATION OF RETAINED AUSTENITE WITH AUSTENITIZING TEMPERATURE IN AS QUENCHED 4340 STEEL.

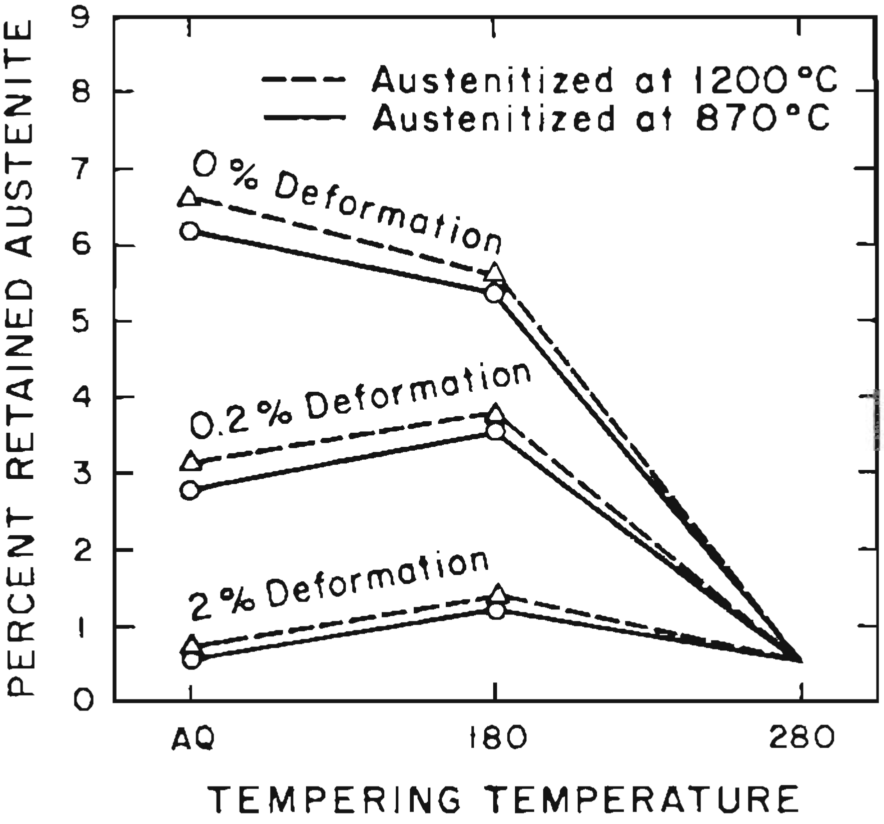

Figure 36. MAGNETIC SATURATION ANALYSIS SHOWING THE VARIATION OF RETAINED AUSTENITE IN AS QUENCHED, QUENCHED AND TEMPERED AISI 4340 STEEL WITH % DEFORMATION.

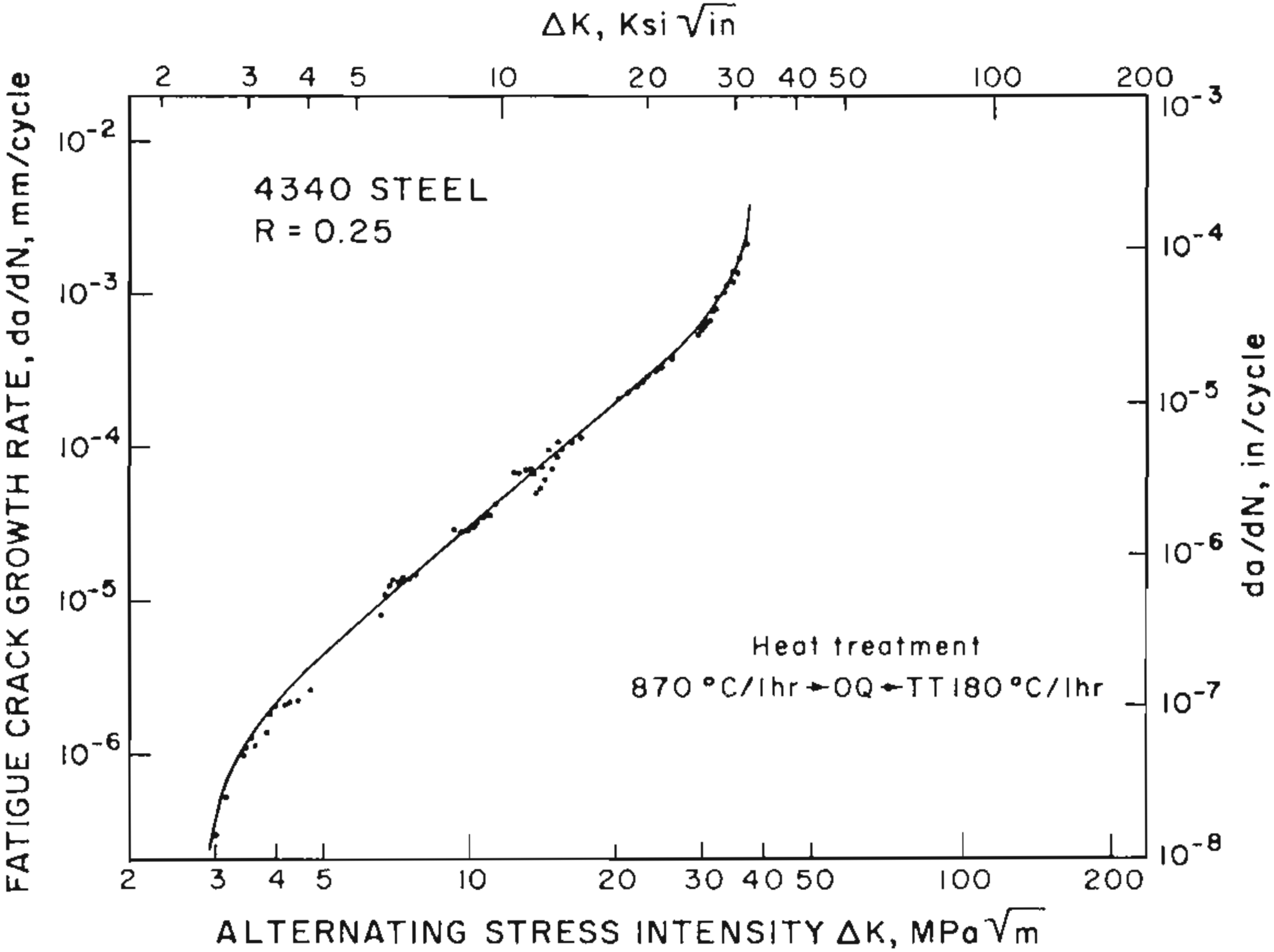

Figure 37. VARIATION OF FATIGUE CRACK GROWTH RATE WITH ALTERNATING STRESS INTENSITY.

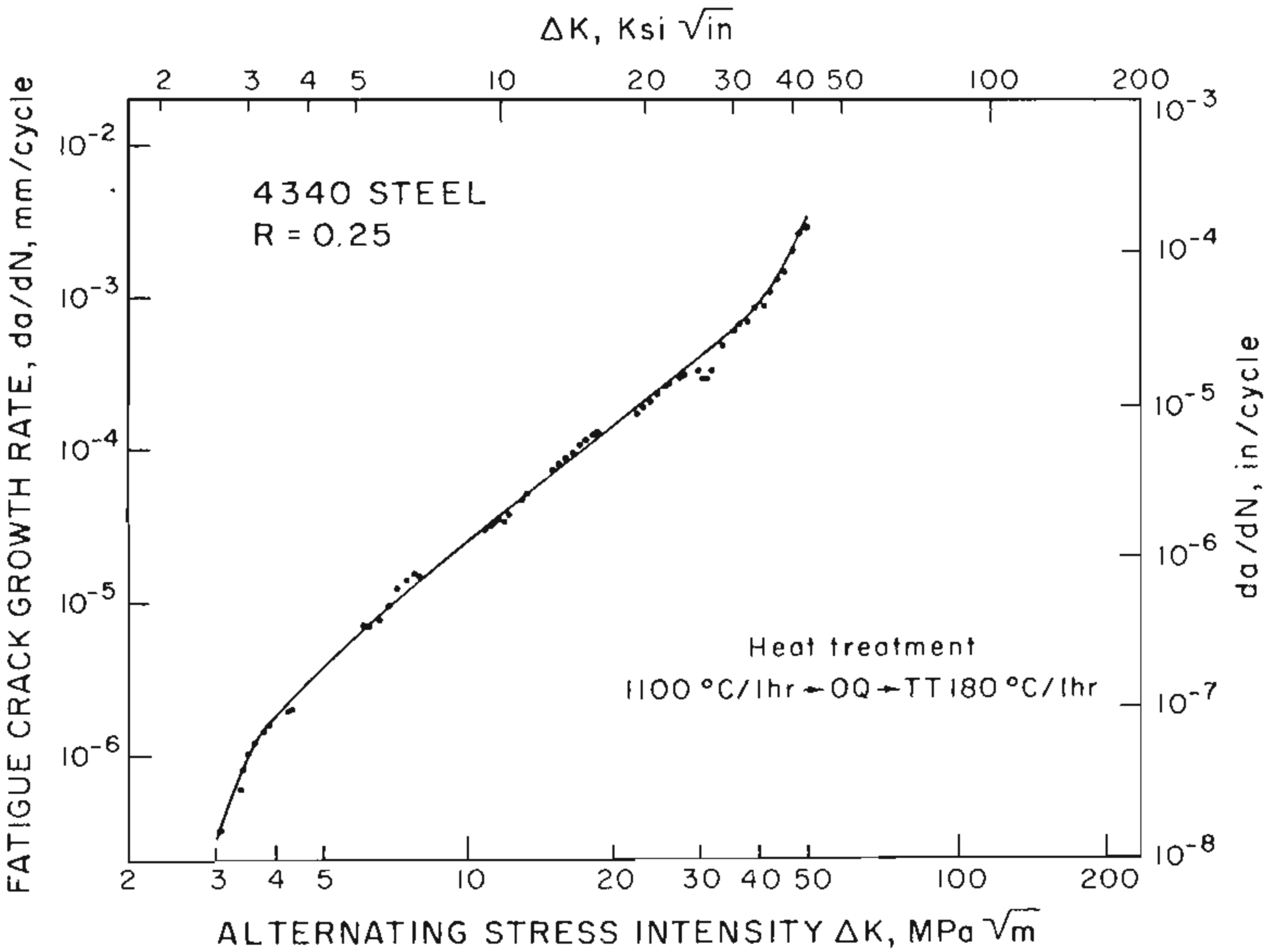

Figure 38. VARIATION OF FATIGUE CRACK GROWTH RATE WITH ALTERNATING STRESS INTENSITY.

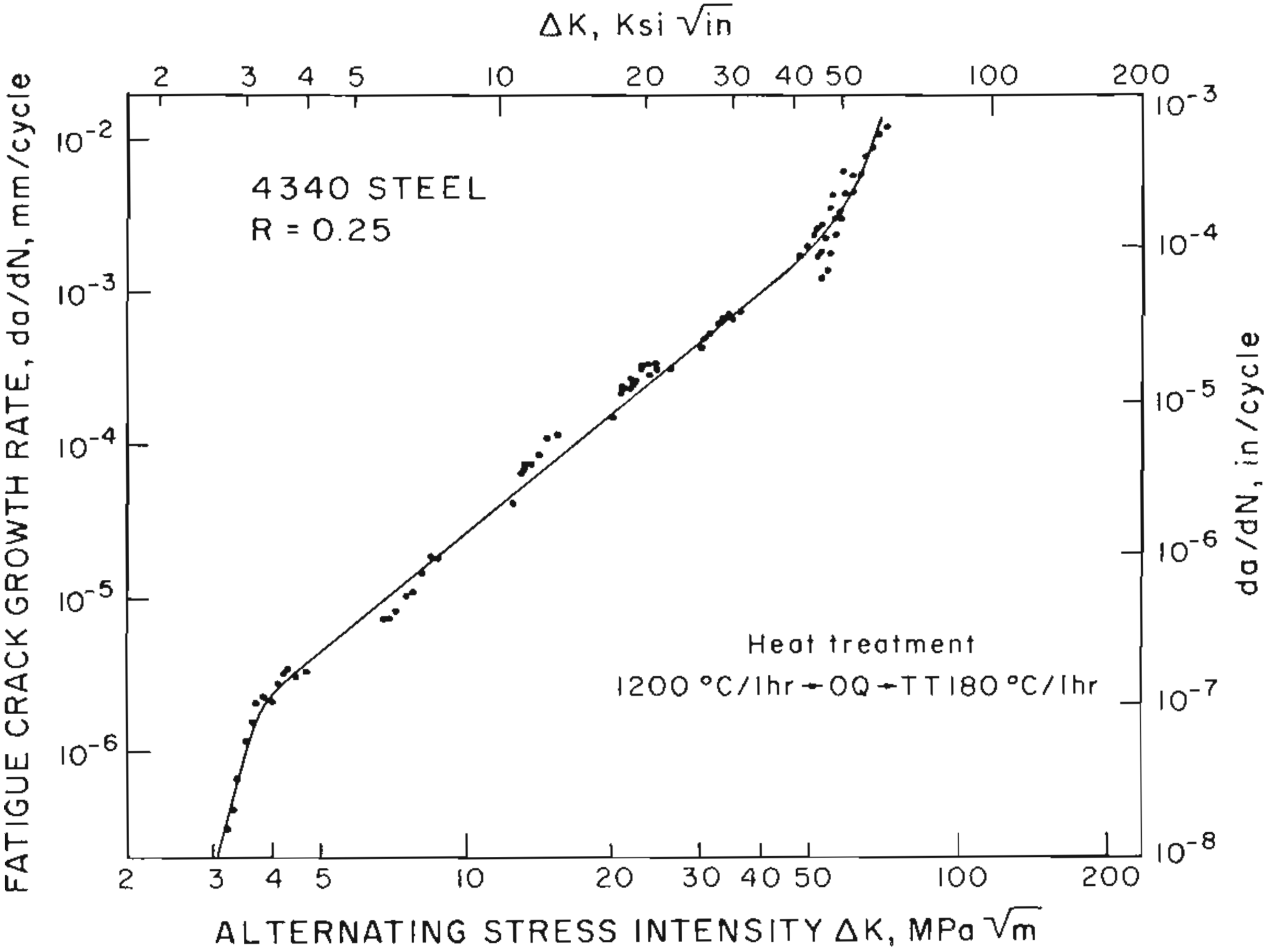

Figure 39. VARIATION OF FATIGUE CRACK GROWTH RATE WITH ALTERNATING STRESS INTENSITY.

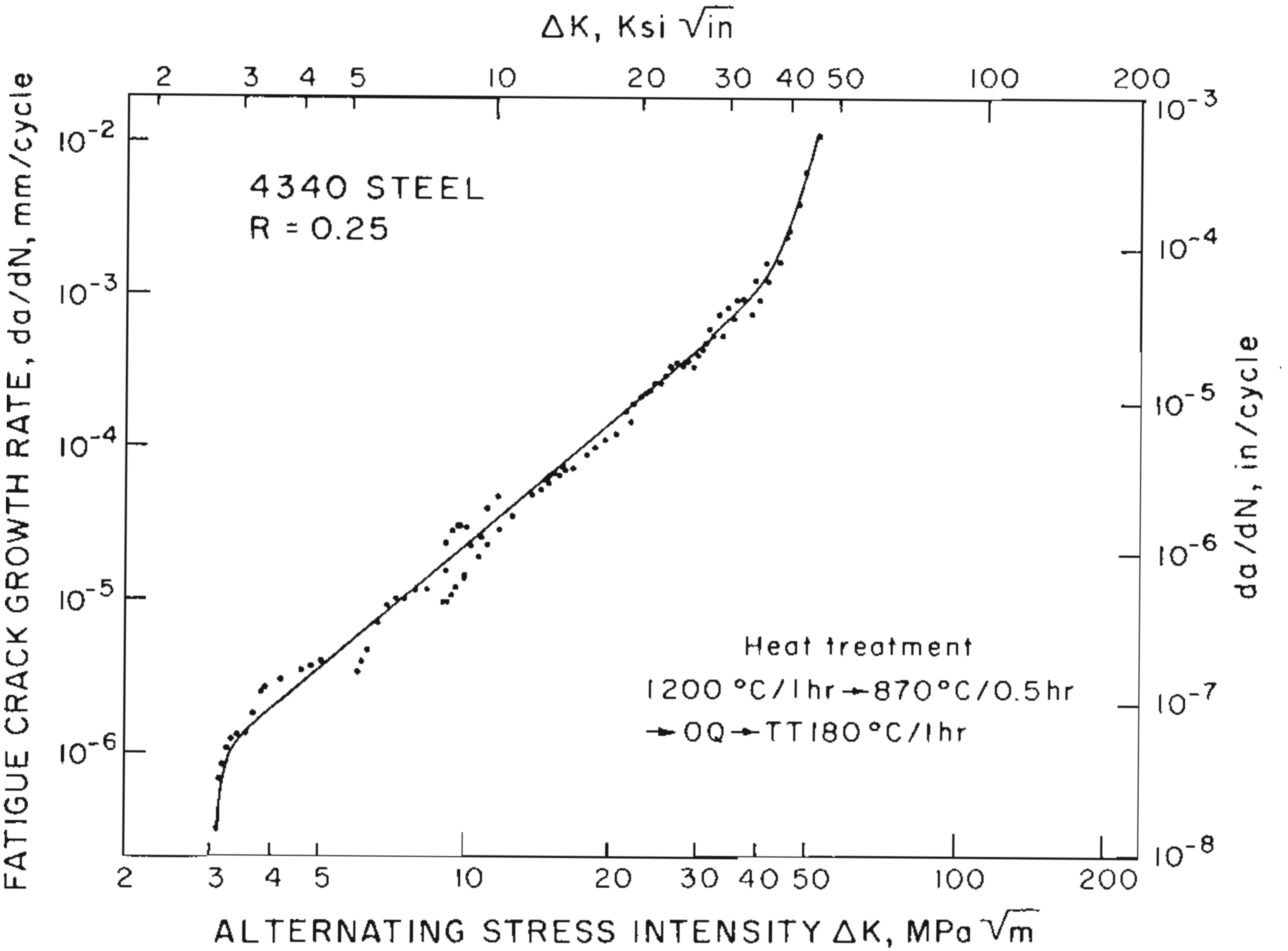

Figure 40. VARIATION OF FATIGUE CRACK GROWTH RATE WITH ALTERNATING STRESS INTENSITY.

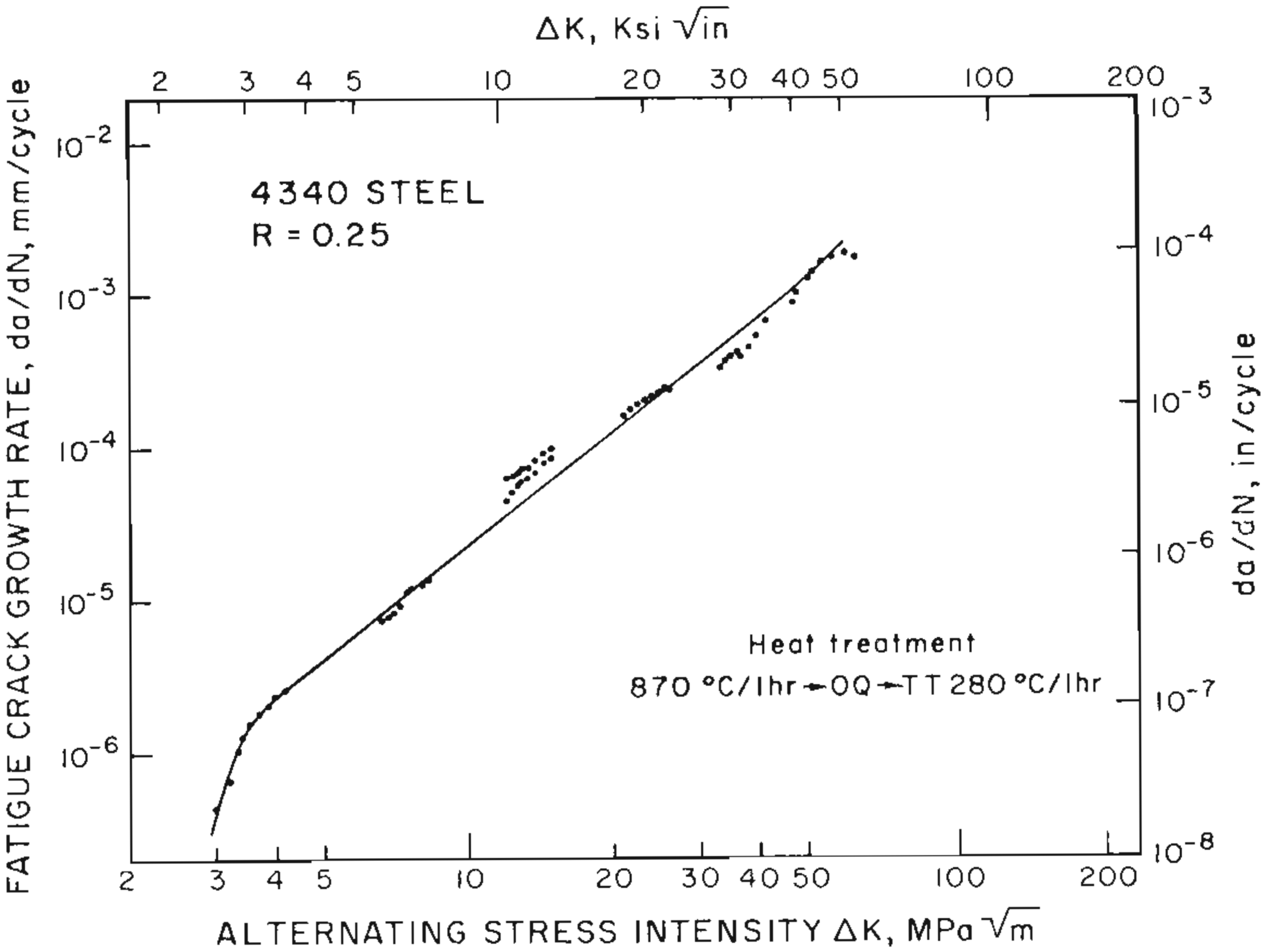

Figure 41. VARIATION OF FATIGUE CRACK GROWTH RATE WITH ALTERNATING STRESS INTENSITY

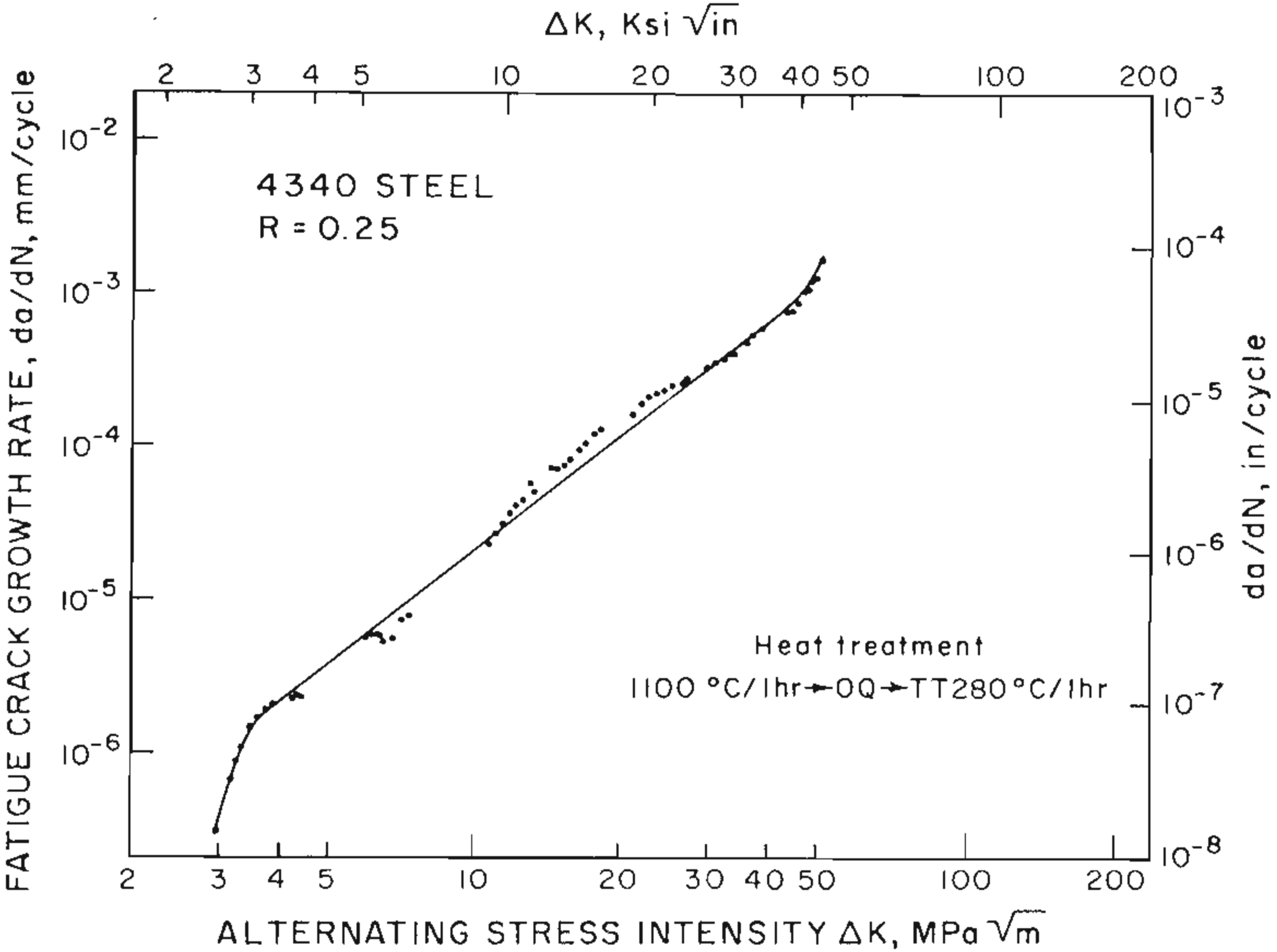

Figure 42. VARIATION OF FATIGUE CRACK GROWTH RATE WITH ALTERNATING STRESS INTENSITY.

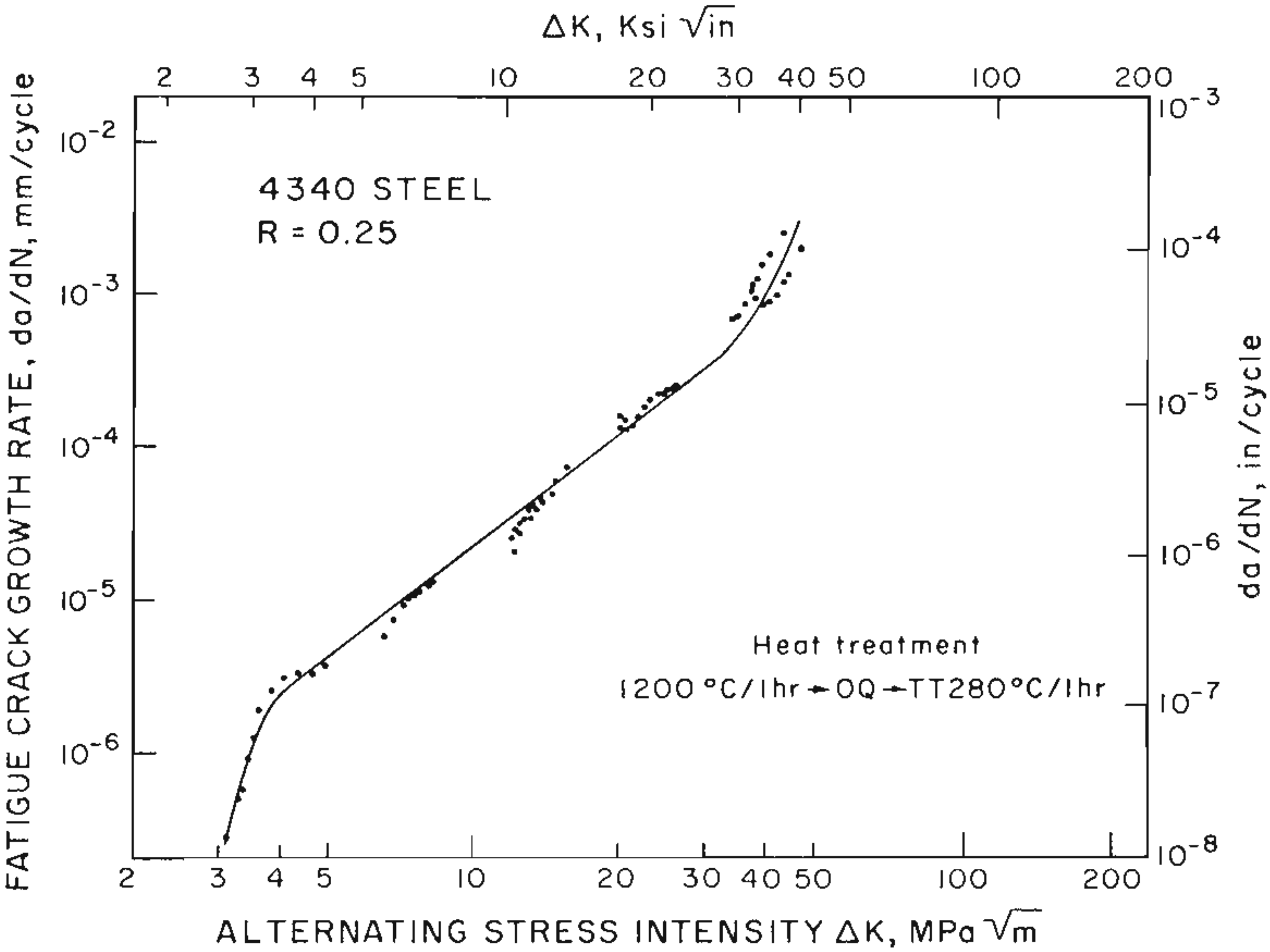

Figure 43. VARIATION OF FATIGUE CRACK GROWTH RATE WITH ALTERNATING STRESS INTENSITY.

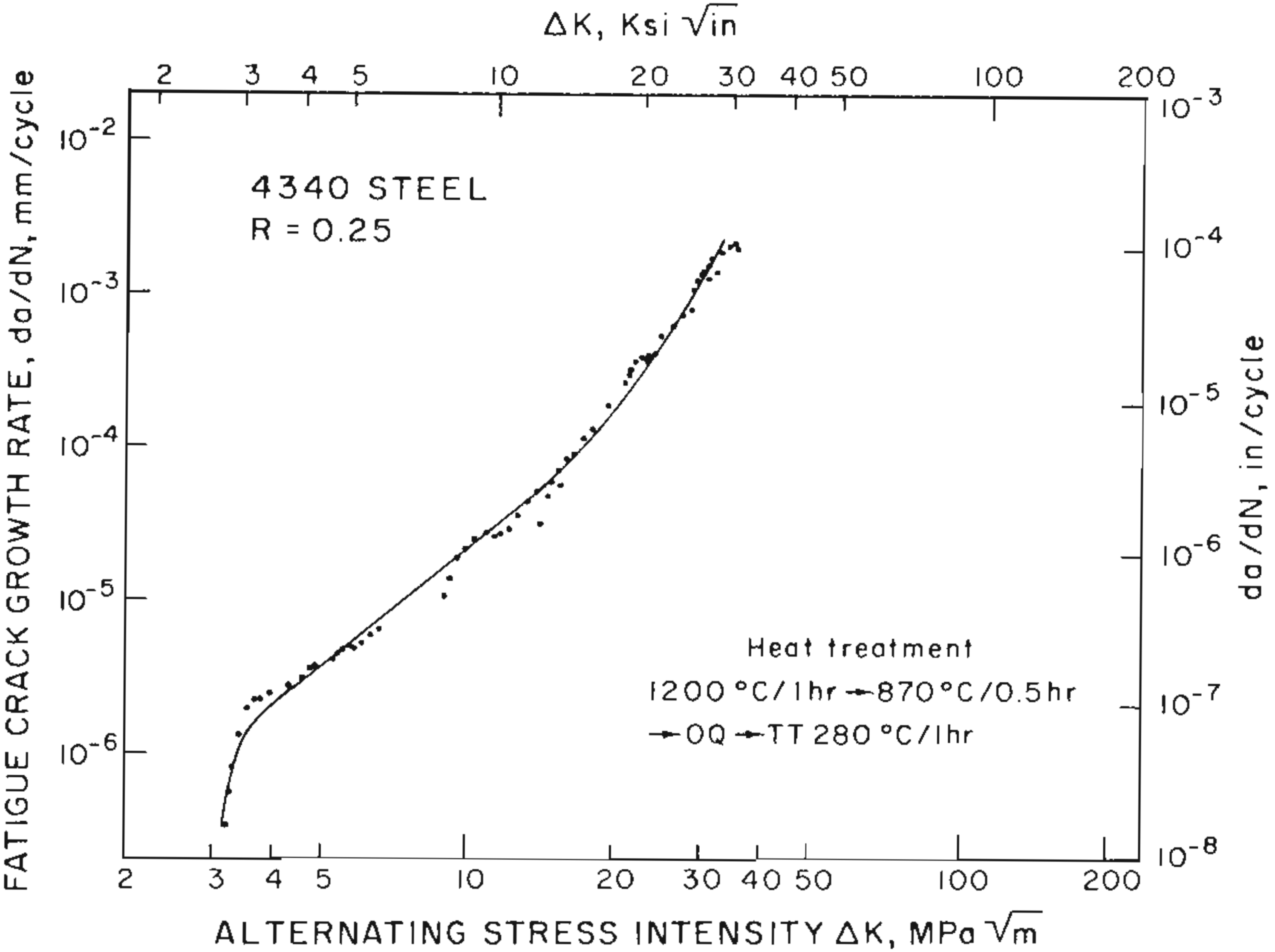

Figure 44. VARIATION OF FATIGUE CRACK GROWTH RATE WITH ALTERNATING STRESS INTENSITY.

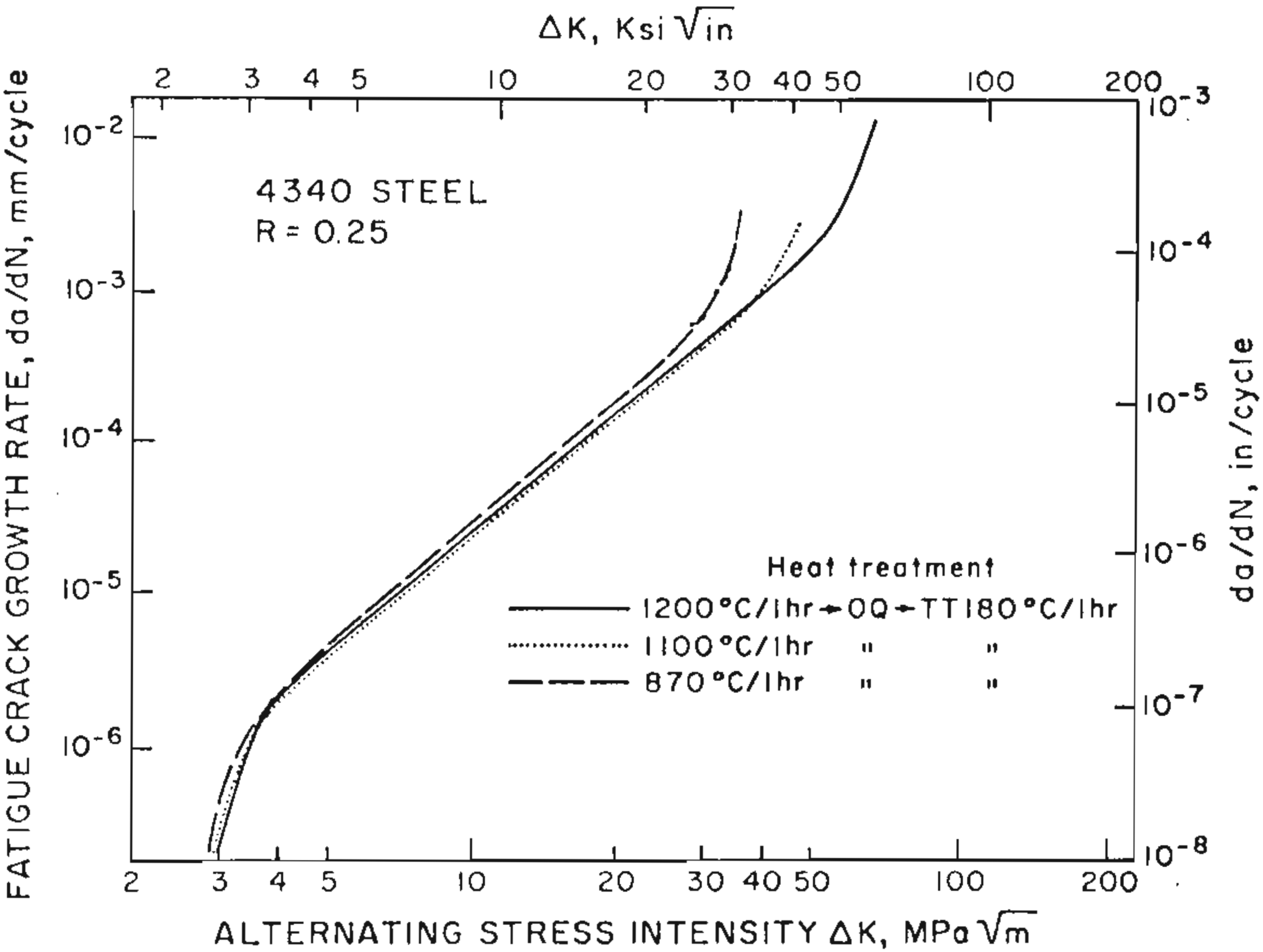

Figure 45. EFFECT OF AUSTENITIZATION TEMPERATURE ON FATIGUE CRACK GROWTH.

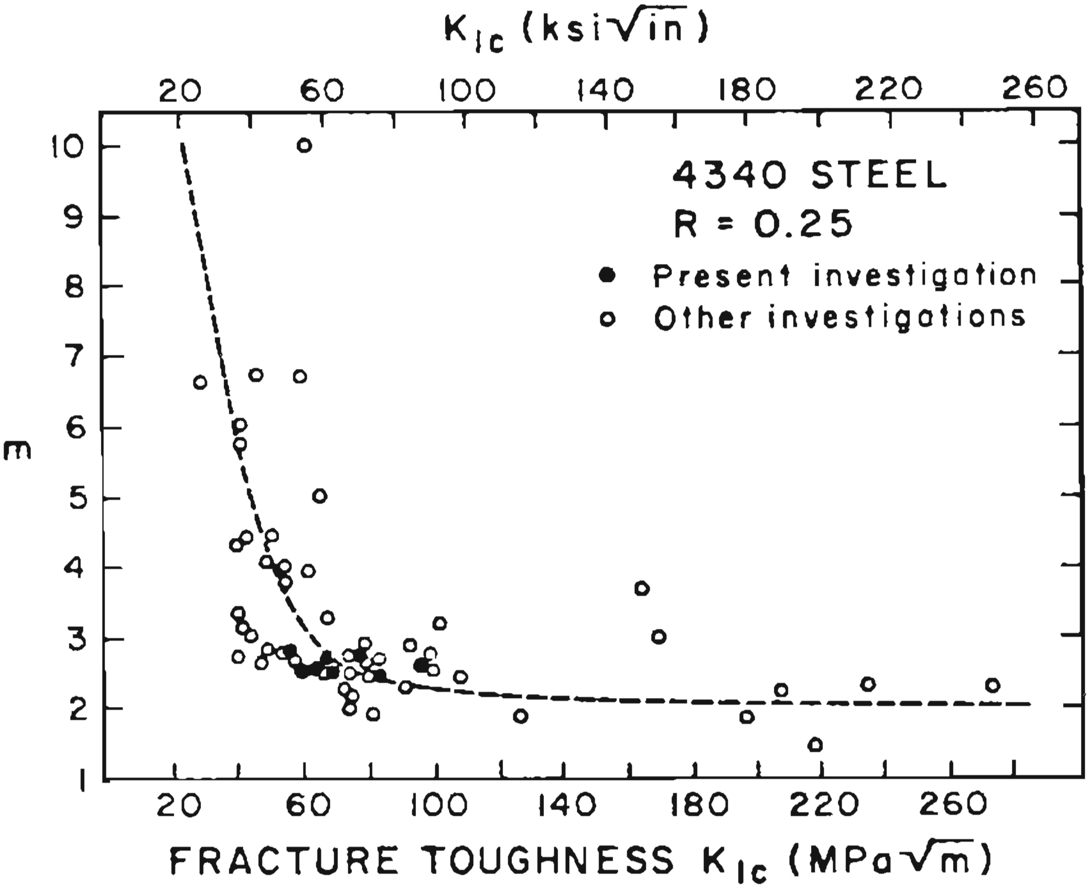

Figure 46. VARIATION OF EXPONENT 'm' OF EQUATION 1 WITH FRACTURE TOUGHNESS K_{1c} FOR A VARIETY OF MEDIUM AND HIGH STRENGTH STEELS. THE RESULTS OF PRESENT INVESTIGATION COMPARED WITH RESULTS OF OTHER INVESTIGATORS.[25]

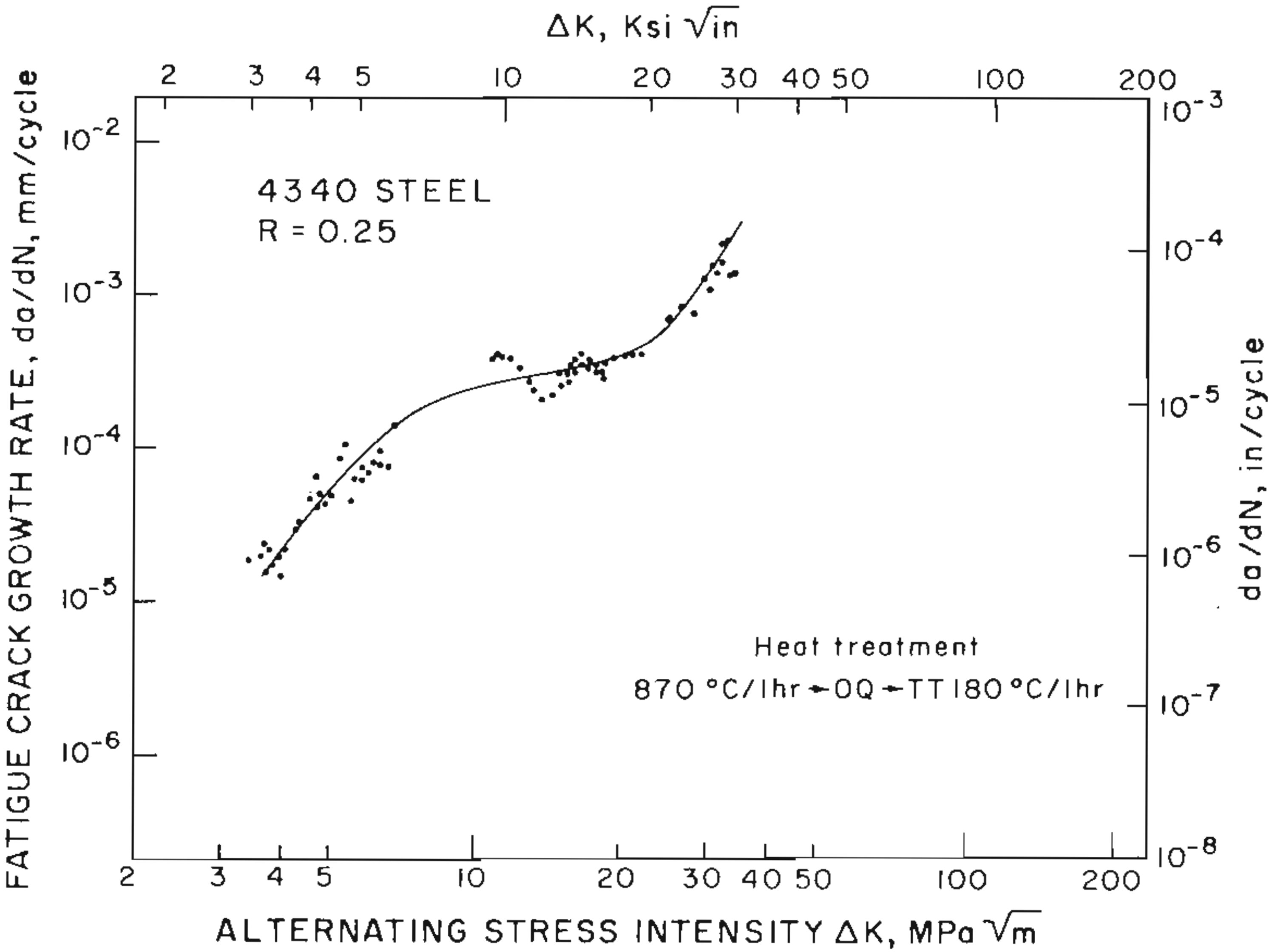

Figure 47. VARIATION OF FATIGUE CRACK GROWTH RATE WITH ALTERNATING STRESS INTENSITY IN CHARGED SPECIMENS.

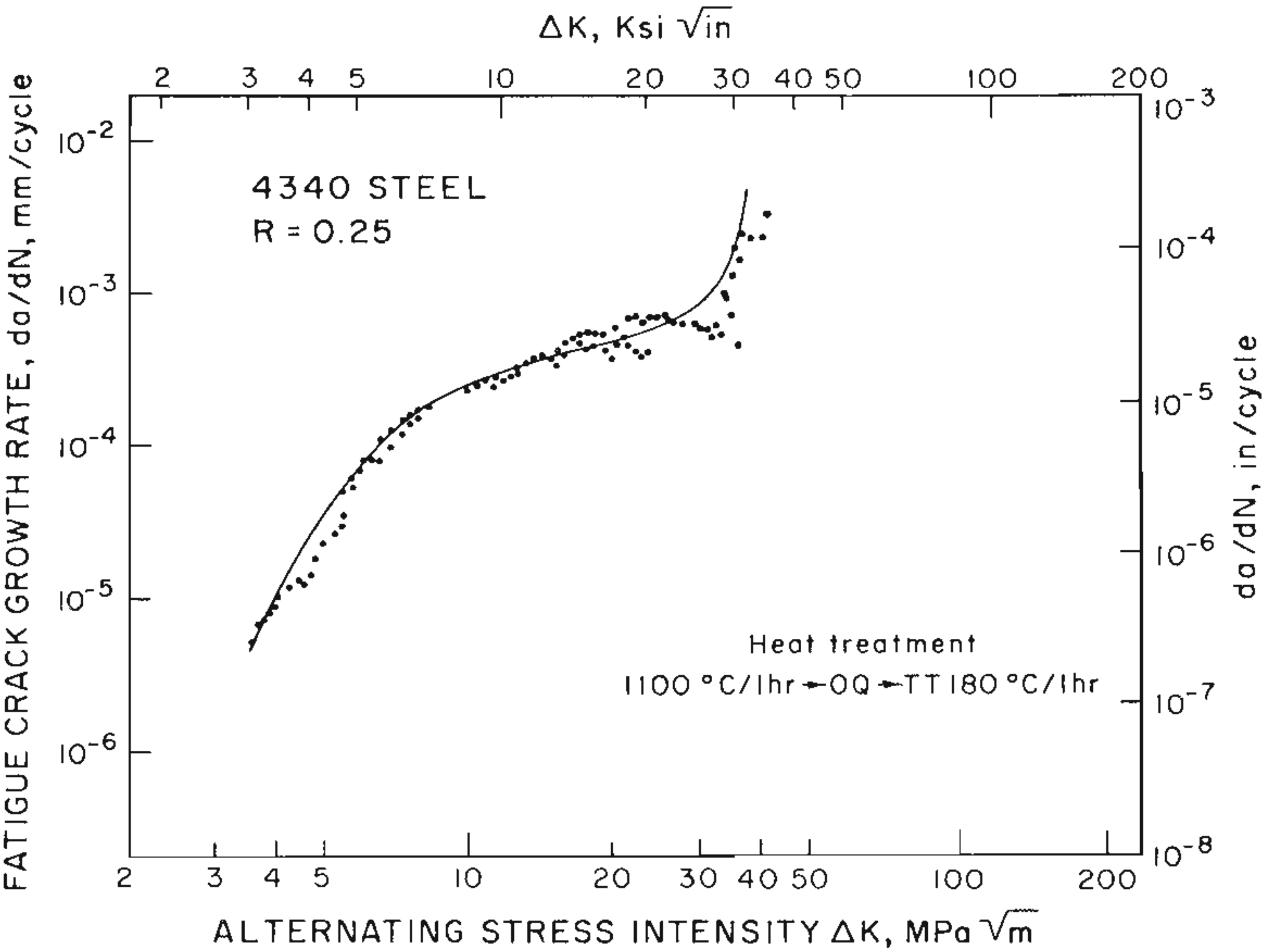

Figure 48. VARIATION OF FATIGUE CRACK GROWTH RATE IN CHARGED SPECIMENS WITH ALTERNATING STRESS INTENSITY

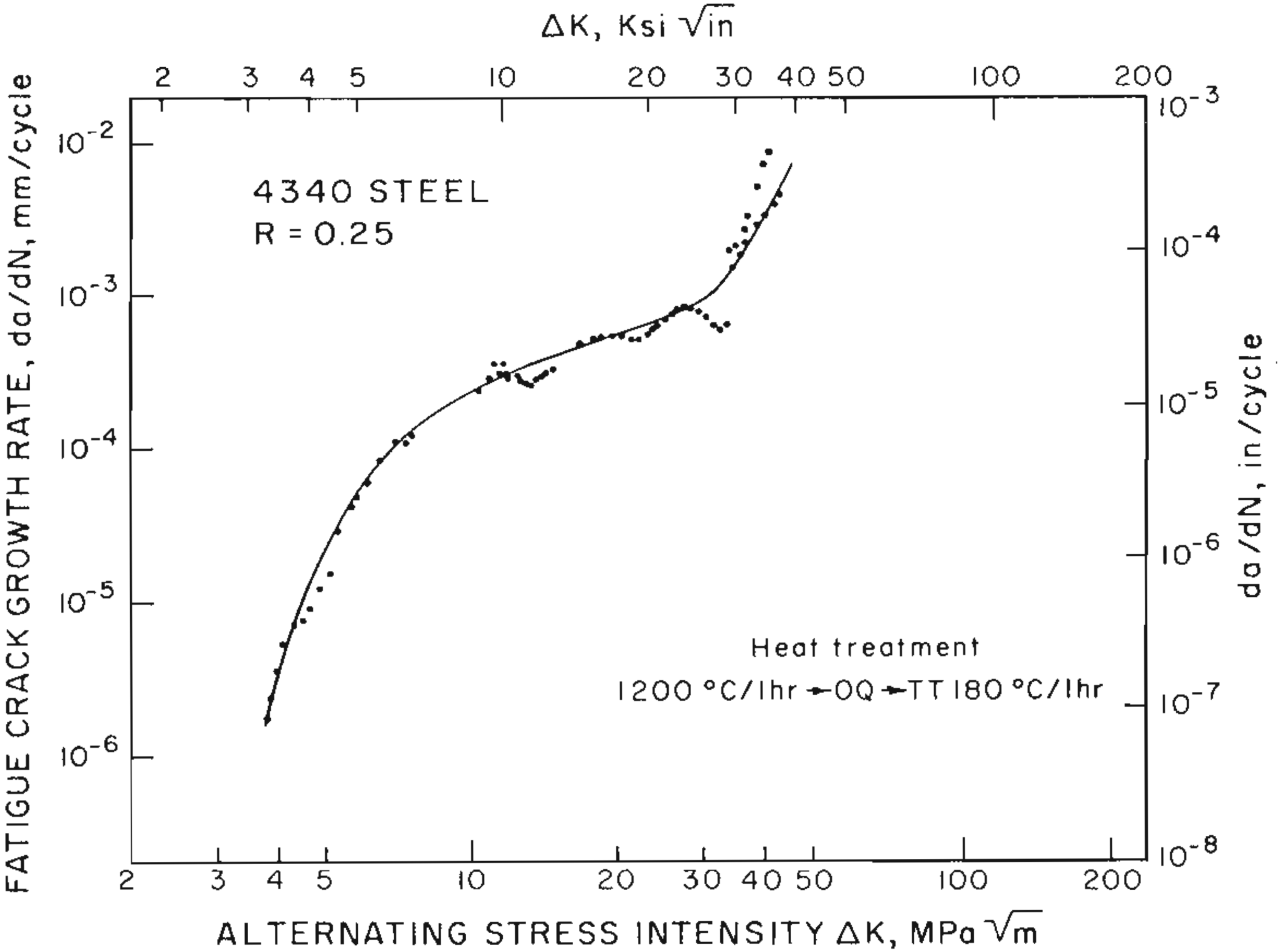

Figure 49. VARIATION OF FATIGUE CRACK GROWTH RATE WITH ALTERNATING STRESS INTENSITY IN CHARGED SPECIMENS.

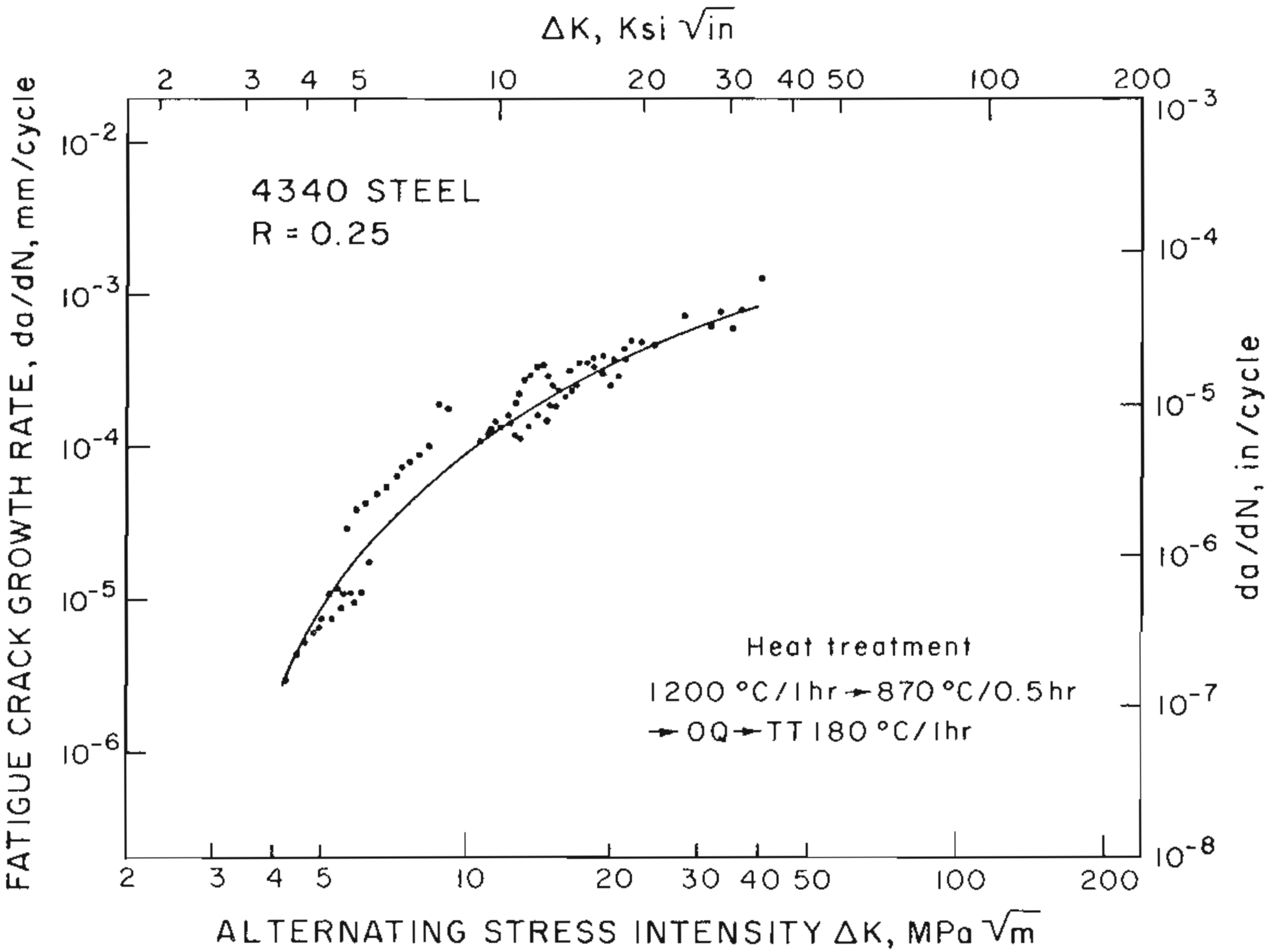

Figure 50. VARIATION OF FATIGUE CRACK GROWTH RATE WITH ALTERNATING STRESS INTENSITY IN CHARGED SPECIMENS.

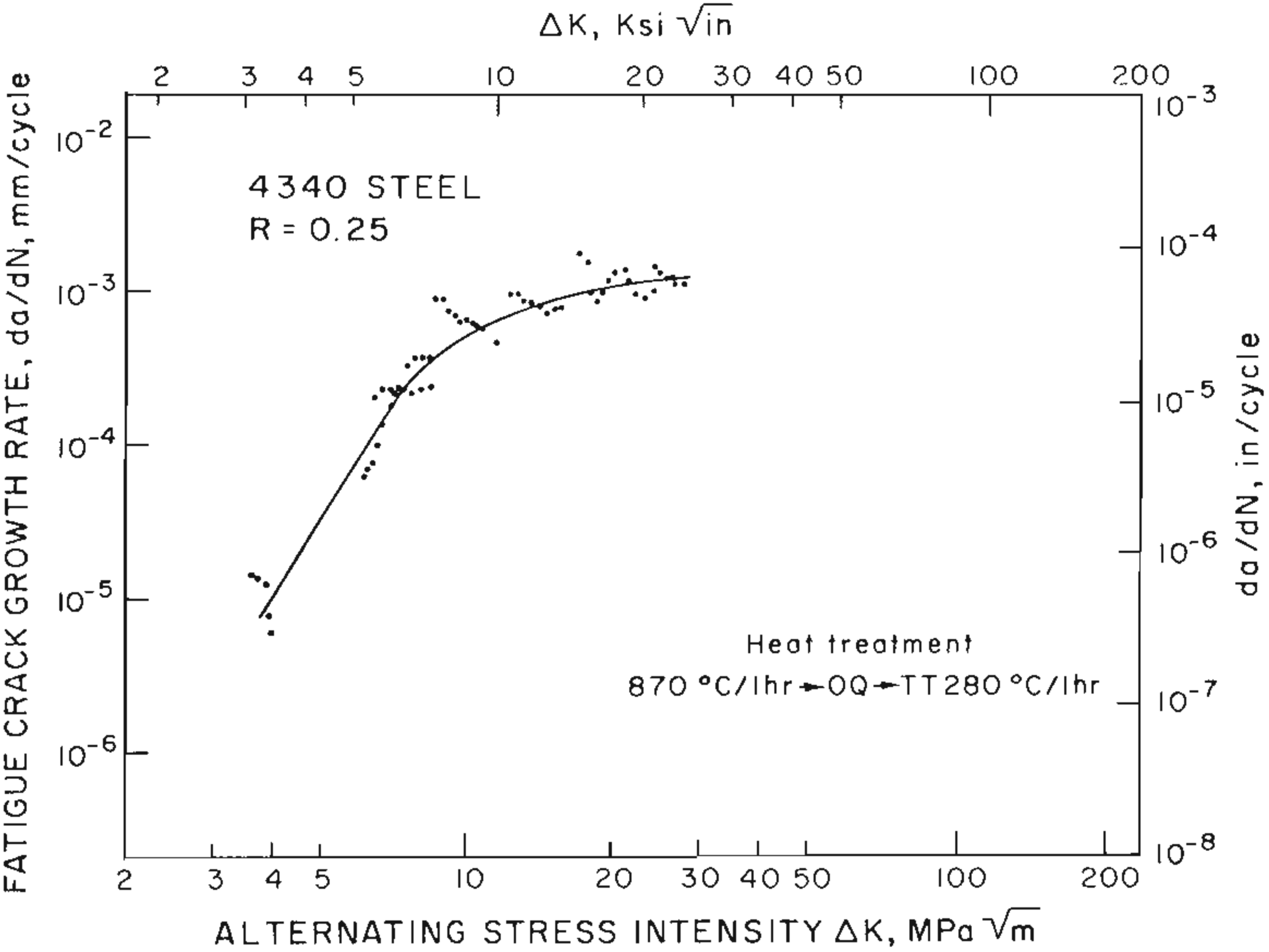

Figure 51. VARIATION OF FATIGUE CRACK GROWTH RATE WITH ALTERNATING STRESS INTENSITY IN CHARGED SPECIMENS.

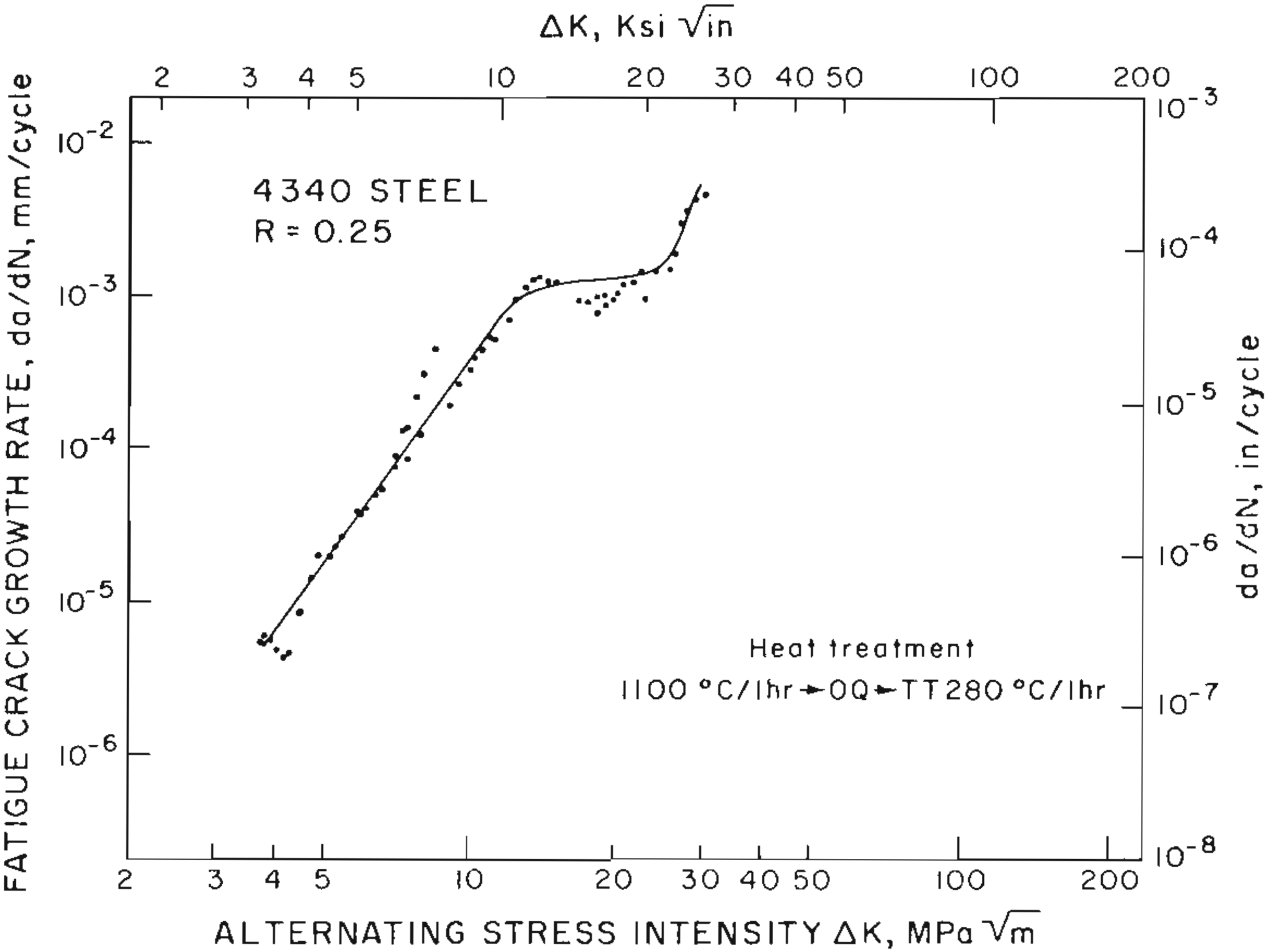

Figure 52. VARIATION OF FATIGUE CRACK GROWTH RATE WITH ALTERNATING STRESS INTENSITY IN CHARGED SPECIMENS.

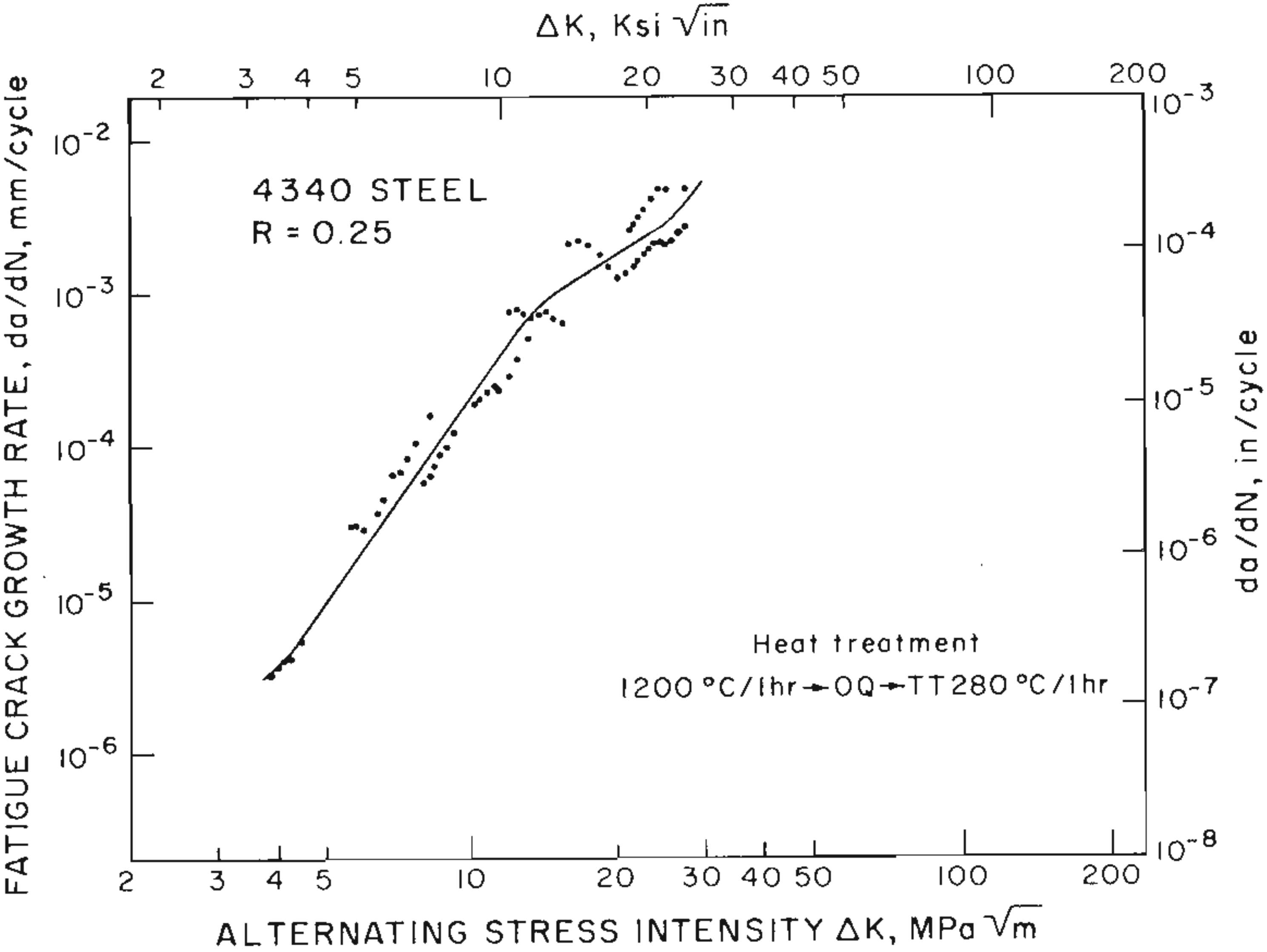

Figure 53. VARIATION OF FATIGUE CRACK GROWTH RATE WITH ALTERNATING STRESS INTENSITY IN CHARGED SPECIMENS.

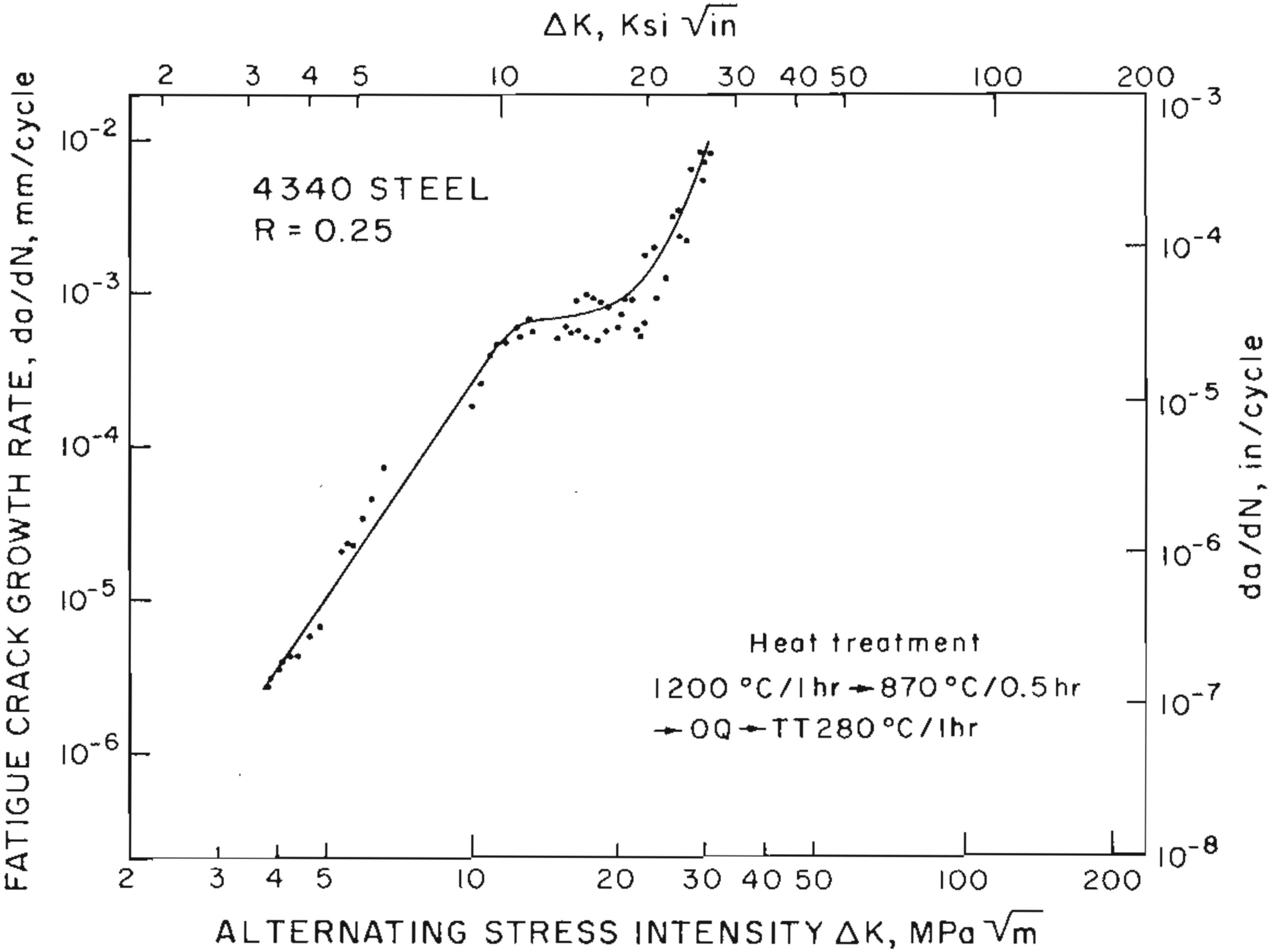

Figure 54. VARIATION OF FATIGUE CRACK GROWTH WITH ALTERNATING STRESS INTENSITY IN CHARGED SPECIMENS.

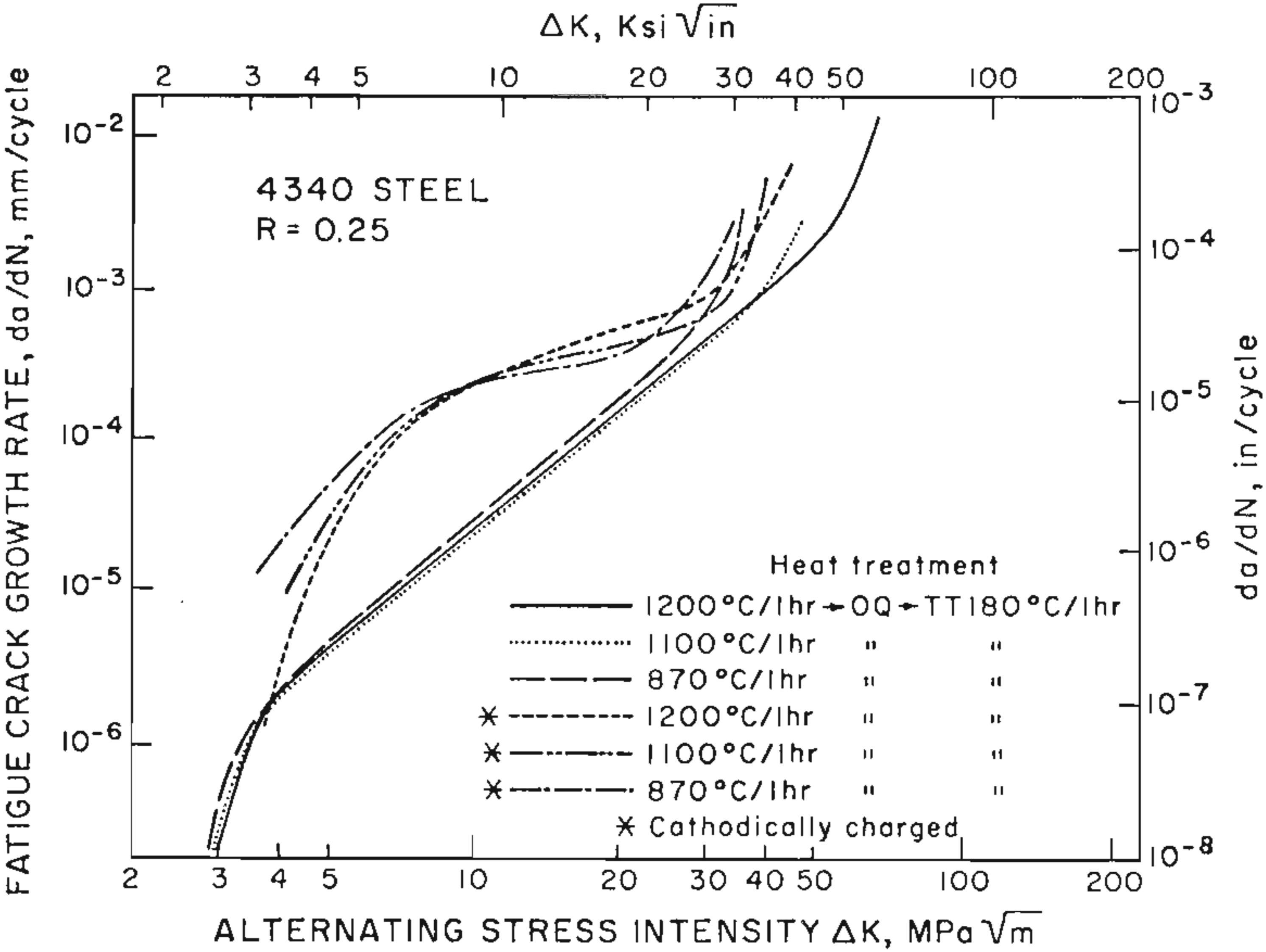

Figure 55. THE EFFECT OF AUSTENITIZATION TEMPERATURE ON FATIGUE CRACK GROWTH RATES IN CHARGED AND IN UNCHARGED SPECIMENS.

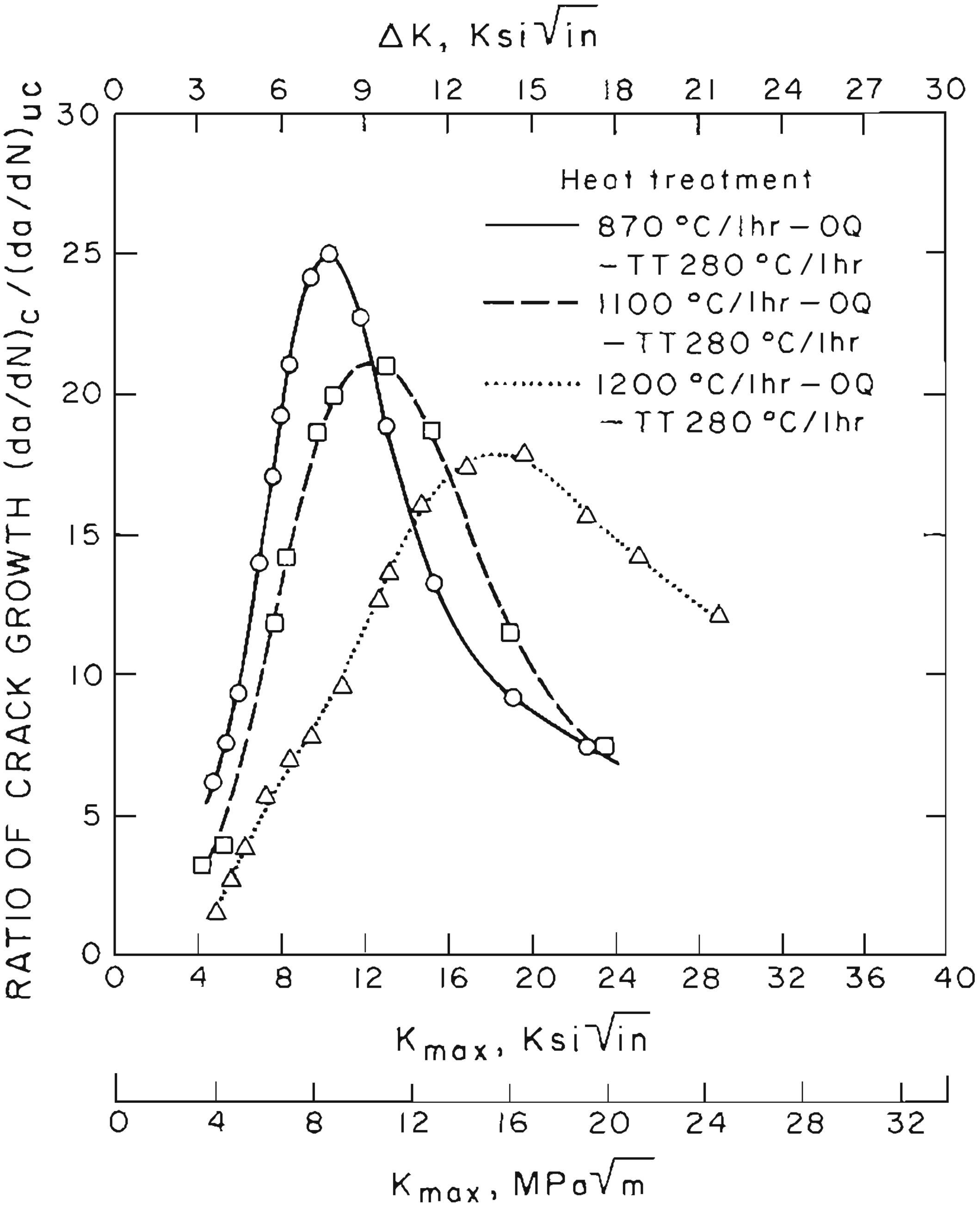

Figure 56. VARIATION OF MAXIMUM ENHANCEMENT IN CRACK GROWTH RATES OF CHARGED SPECIMENS WITH AUSTENITIZING TEMPERATURE.

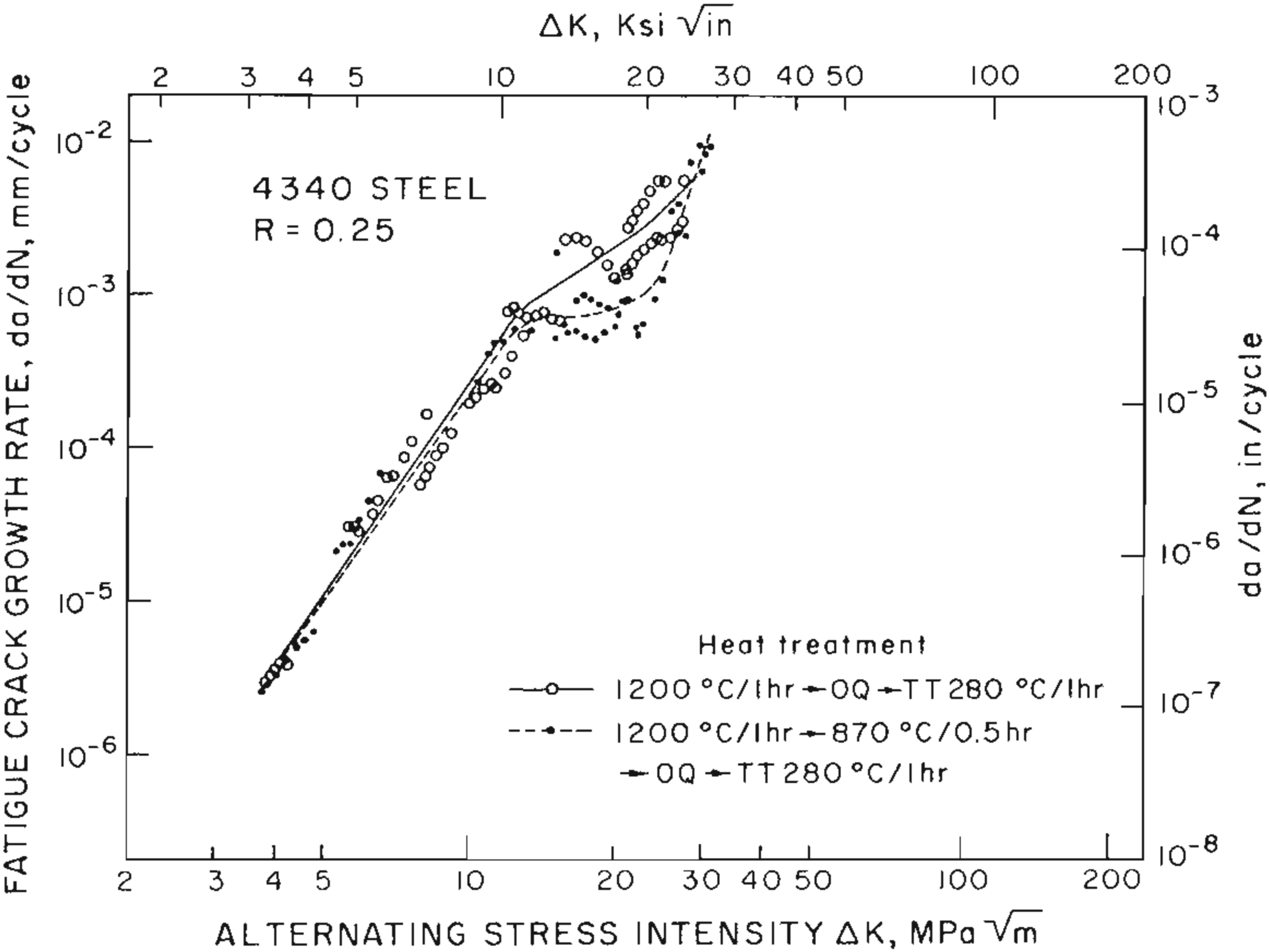

Figure 57. EFFECT OF STEP HEAT TREATMENT IN FATIGUE CRACK GROWTH RATES IN CHARGED SPECIMENS.

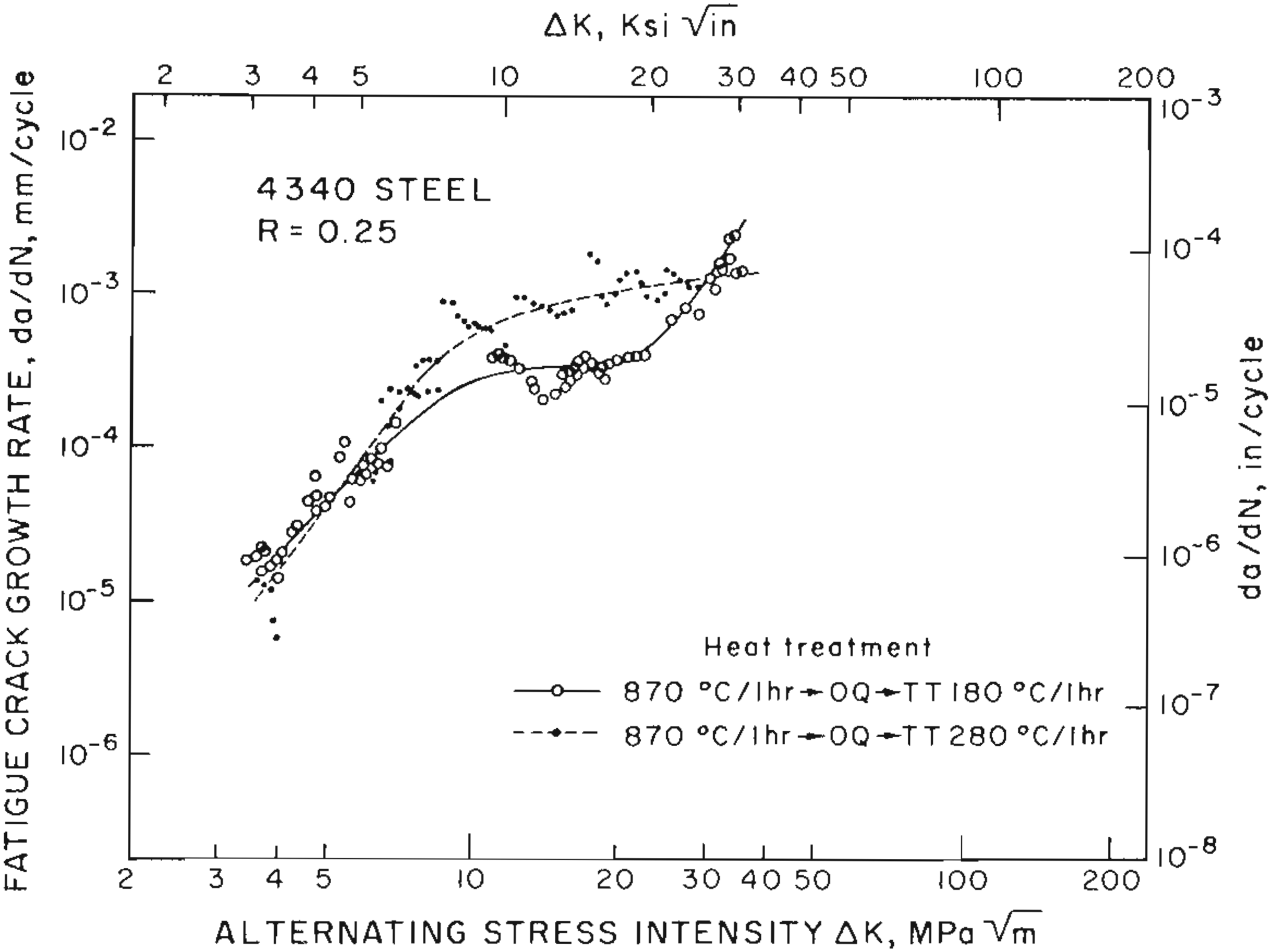

Figure 58. EFFECT OF TEMPERING TEMPERATURE ON FATIGUE CRACK GROWTH RATES IN CHARGED SPECIMENS.

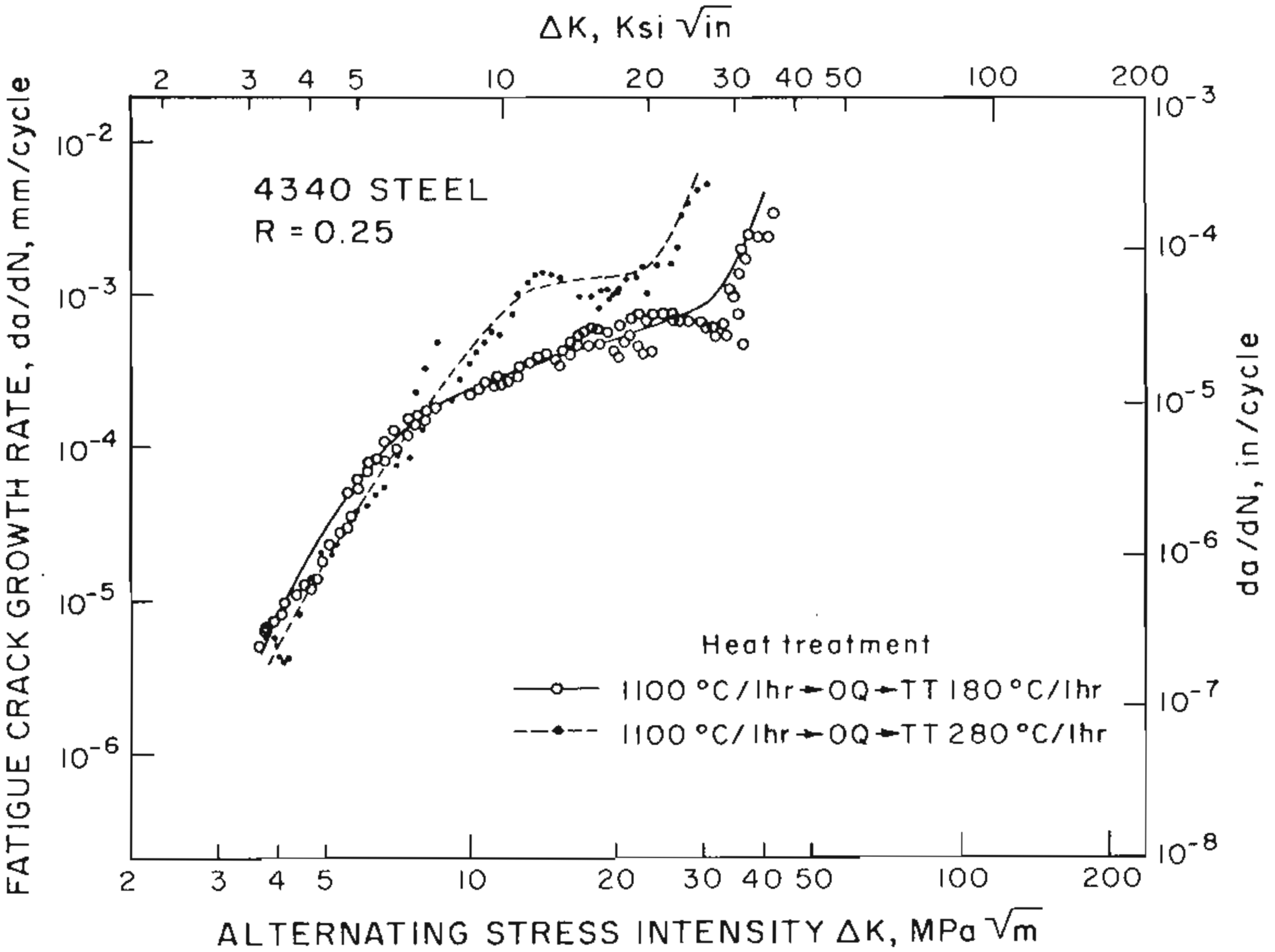

Figure 59. EFFECT OF TEMPERING TEMPERATURE ON FATIGUE CRACK GROWTH RATES IN CHARGED SPECIMENS.

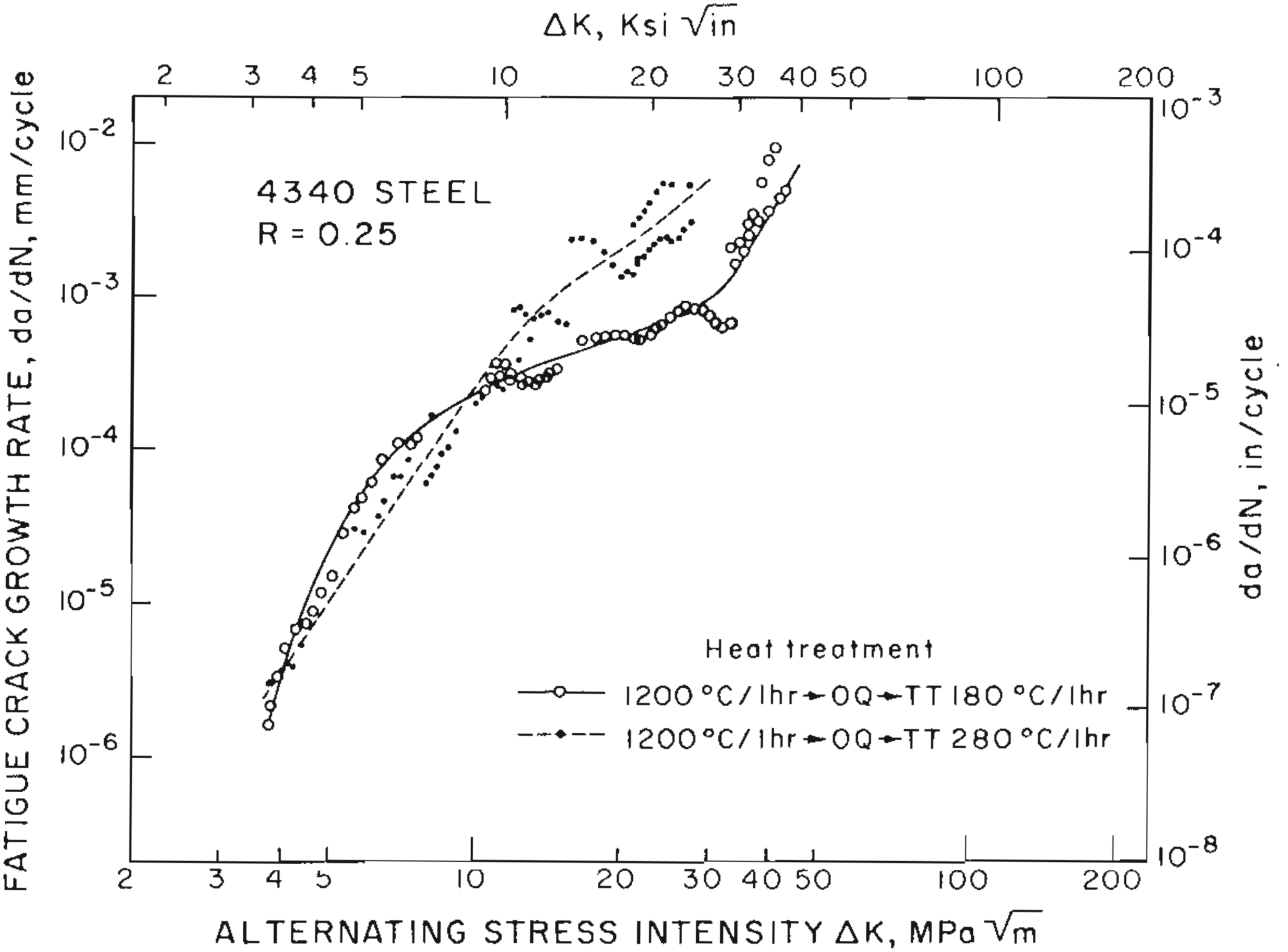

Figure 60. EFFECT OF TEMPERING TEMPERATURE ON FATIGUE CRACK GROWTH RATES IN CHARGED SPECIMENS.

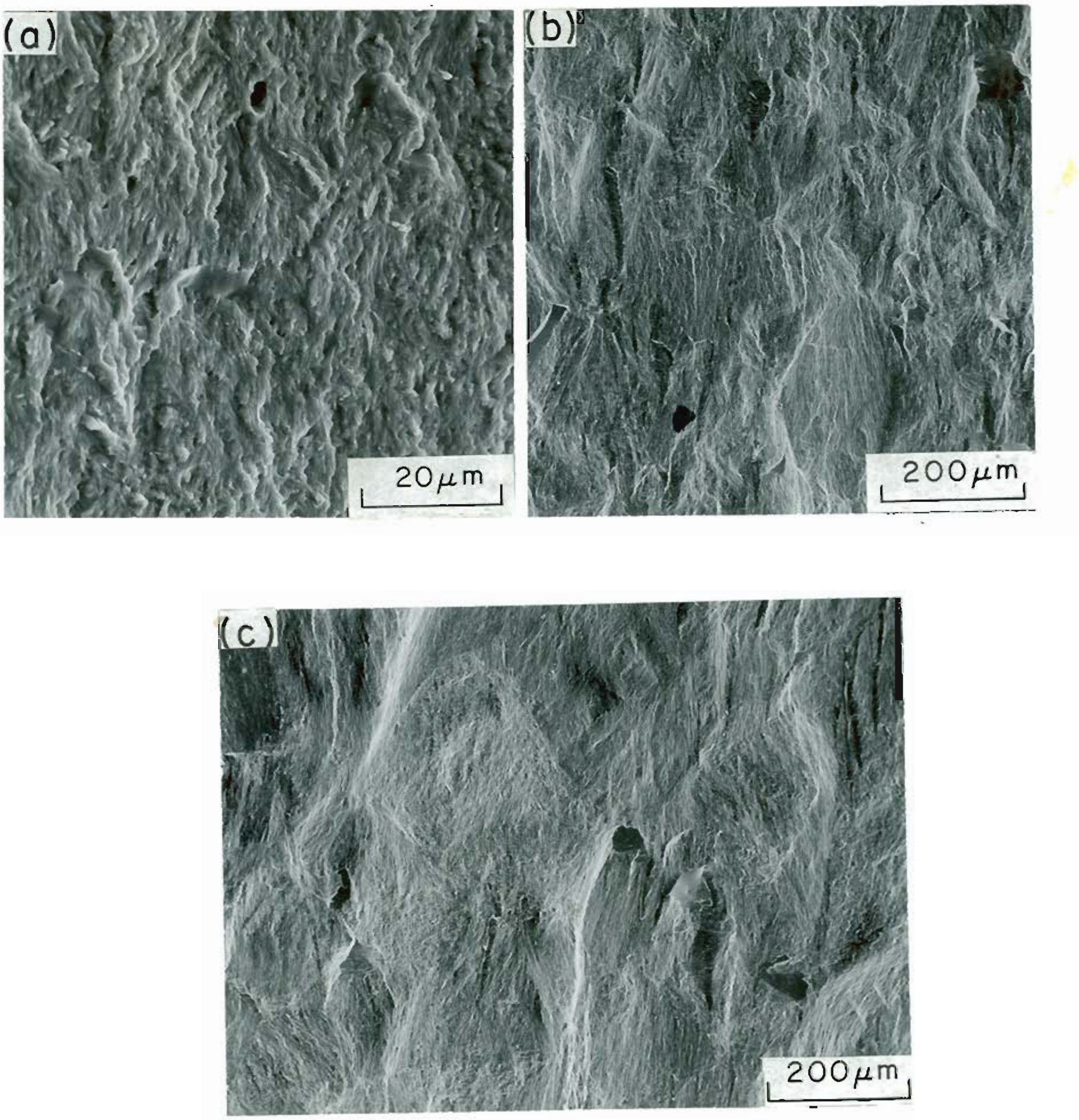

Figure 61. SEM FRACTOGRAPHS OF AISI 4340 STEEL OF UNCHARGED SPECIMENS AT $\Delta K \simeq 3\mathrm{Ksi}\sqrt{\mathrm{in}}$.

(a) AUSTENITIZED AT 870°C AND TEMPERED AT 180°C

(b) AUSTENITIZED AT 1100°C AND TEMPERED AT 180°C

(c) AUSTENITIZED AT 1200°C AND TEMPERED AT 180°C.

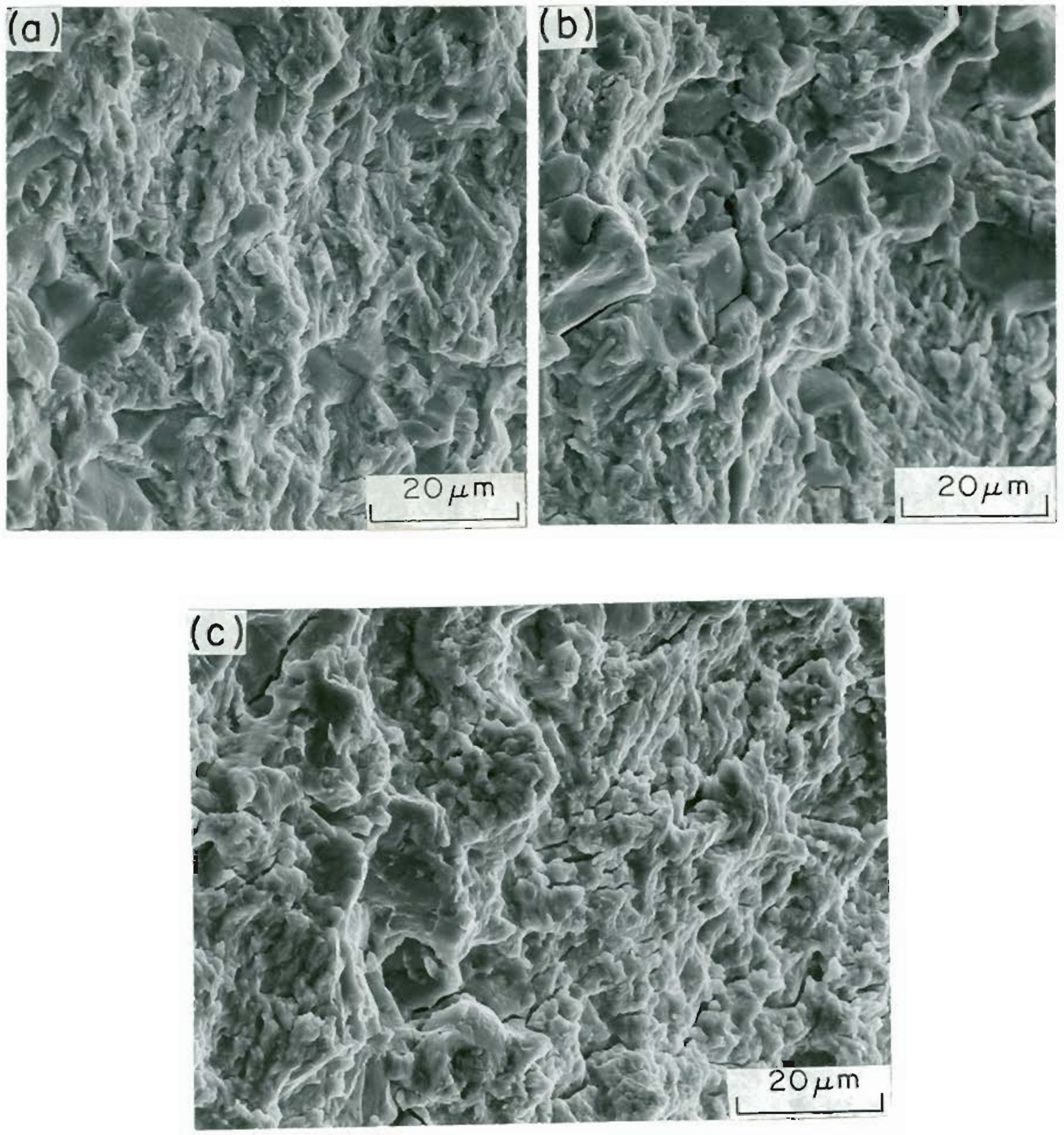

Figure 62. SEM FRACTOGRAPHS OF UNCHARGED SPECIMENS AUSTENITIZED AT 870°C AND TEMPERED AT 280°C SHOWING VARIATION OF INTERGRANULAR FRACTURE WITH THE ALTERNATING STRESS INTENSITY

(a) $\Delta K \simeq 6$ Ksi$\sqrt{in}$

(b) $\Delta K \simeq 10$ Ksi$\sqrt{in}$

(c) $\Delta K \simeq 19$ Ksi$\sqrt{in}$.

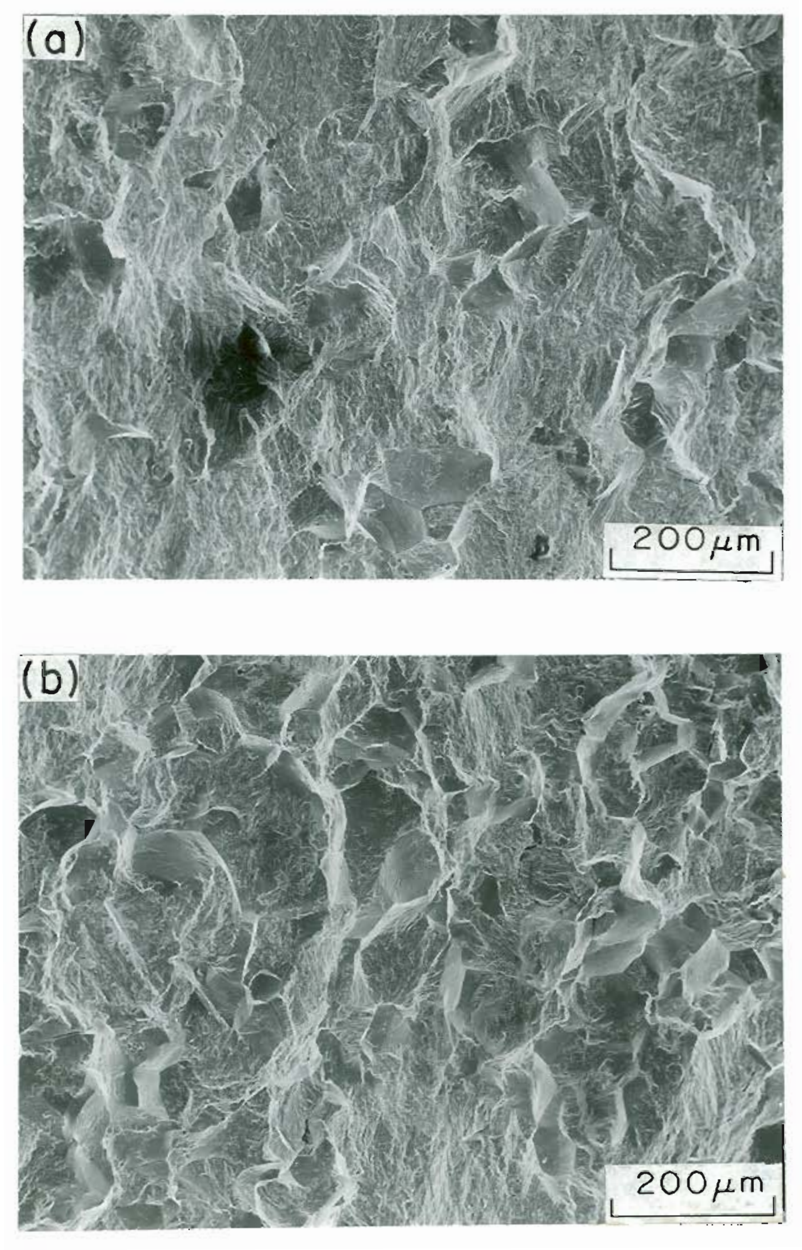

Figure 63. SEM FRACTOGRAPHS OF UNCHARGED SPECIMENS AUSTENITIZED AT 1100°C SHOWING THE VARIATION OF INTERGRANULAR FRACTURE ($\Delta K \simeq 13$ Ksi$\sqrt{in}$) WITH TEMPERING TEMPERATURE

(a) TEMPERED AT 180°C

(b) TEMPERED AT 280°C.

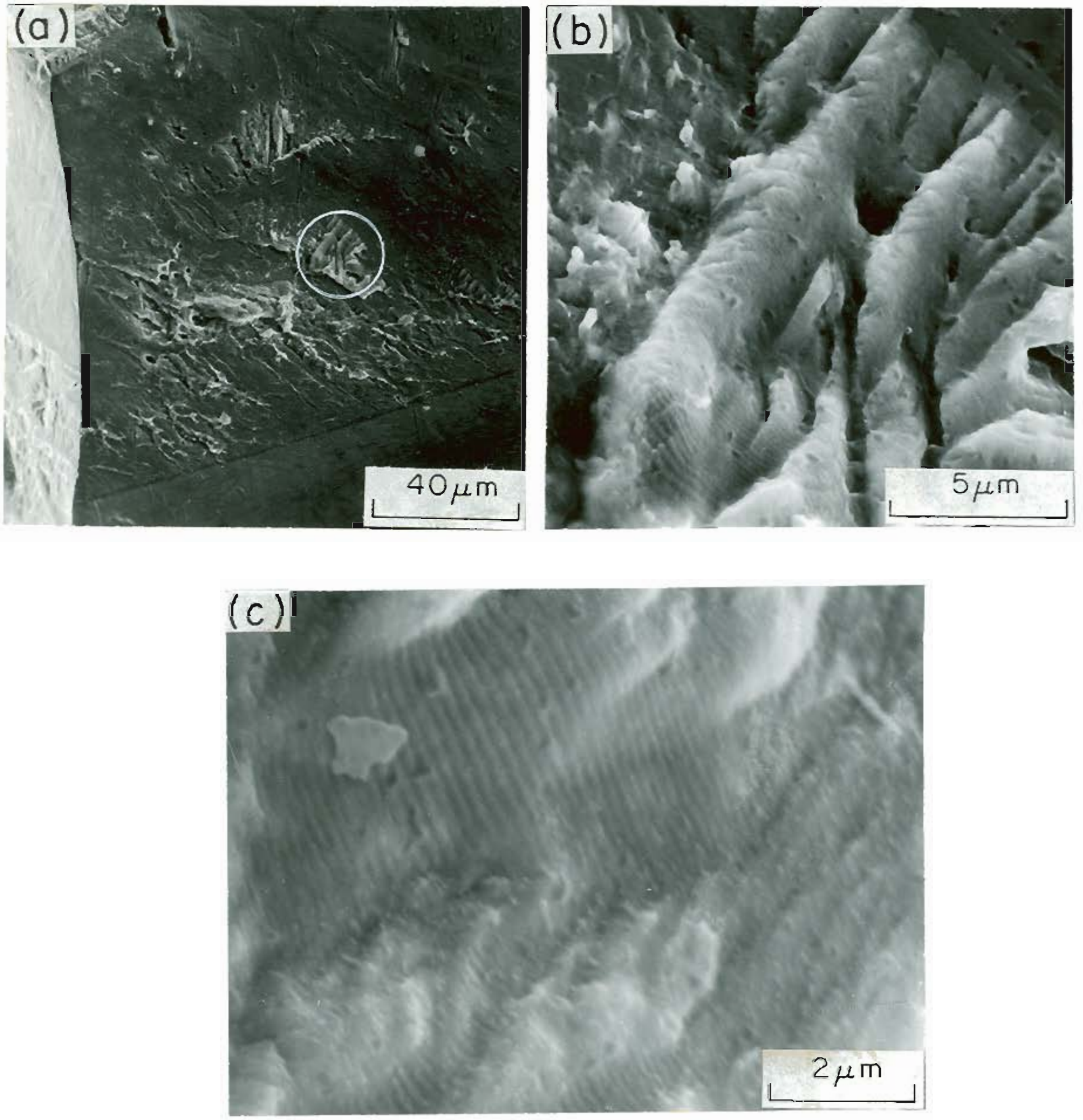

Figure 64. SEM FRACTOGRAPHS OF UNCHARGED SPECIMENS AUSTENITIZED AT 1200°C AND TEMPERED AT 180°C ($\Delta K \approx 17.5$ Ksi$\sqrt{\text{in}}$)

(a) SHOWING INTERGRANULAR FACETS

(b) ENLARGEMENT OF CIRCLED REGION SHOWING FATIGUE STRIATIONS

(c) SHOWING FATIGUE STRIATIONS ON INTERGRANULAR FACET FROM DIFFERENT AREA.

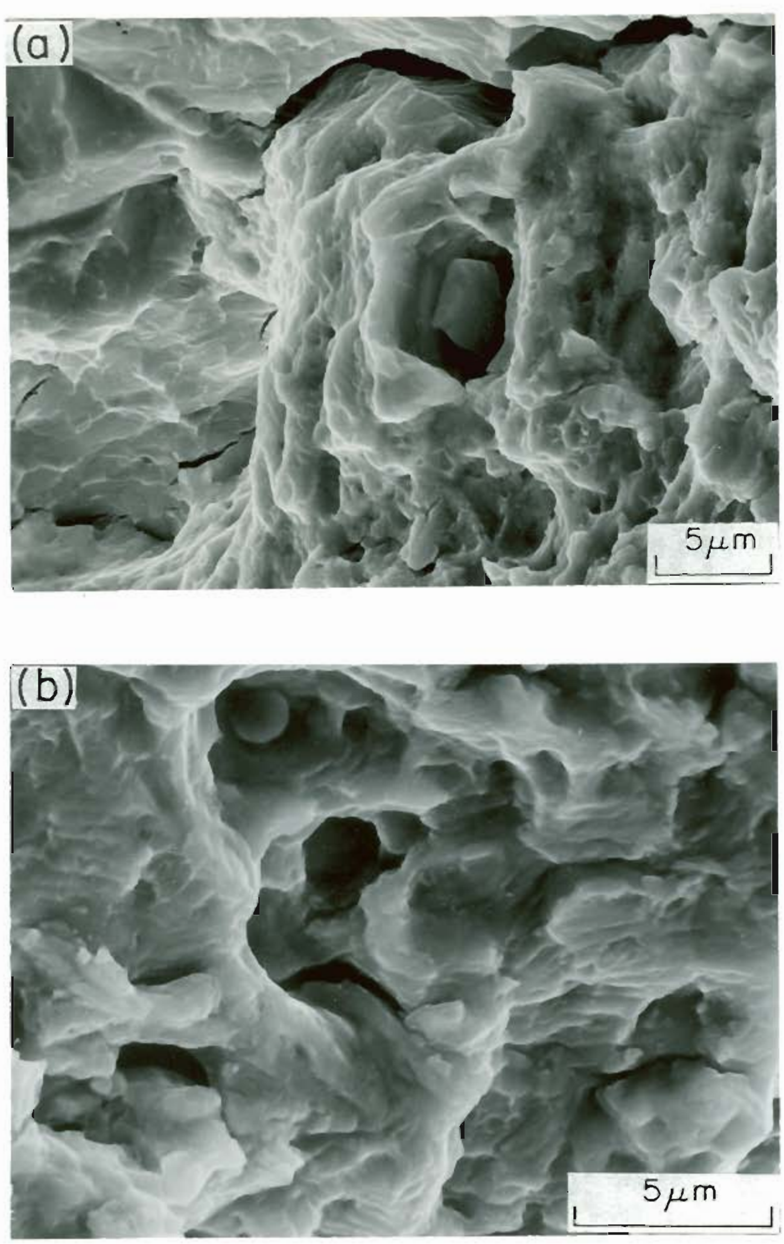

Figure 65. SEM FRACTOGRAPHS OF UNCHARGED SPECIMENS

(a) AUSTENITIZED AT 870°C AND TEMPERED AT 180°C

(b) AUSTENITIZED AT 1100°C AND TEMPERED AT 280°C SHOWING THE MECHANISM OF CRACK GROWTH AT INTERMEDIATE STRESS INTENSITY RANGES ($\Delta K \simeq 18$ Ksi$\sqrt{\text{in}}$).

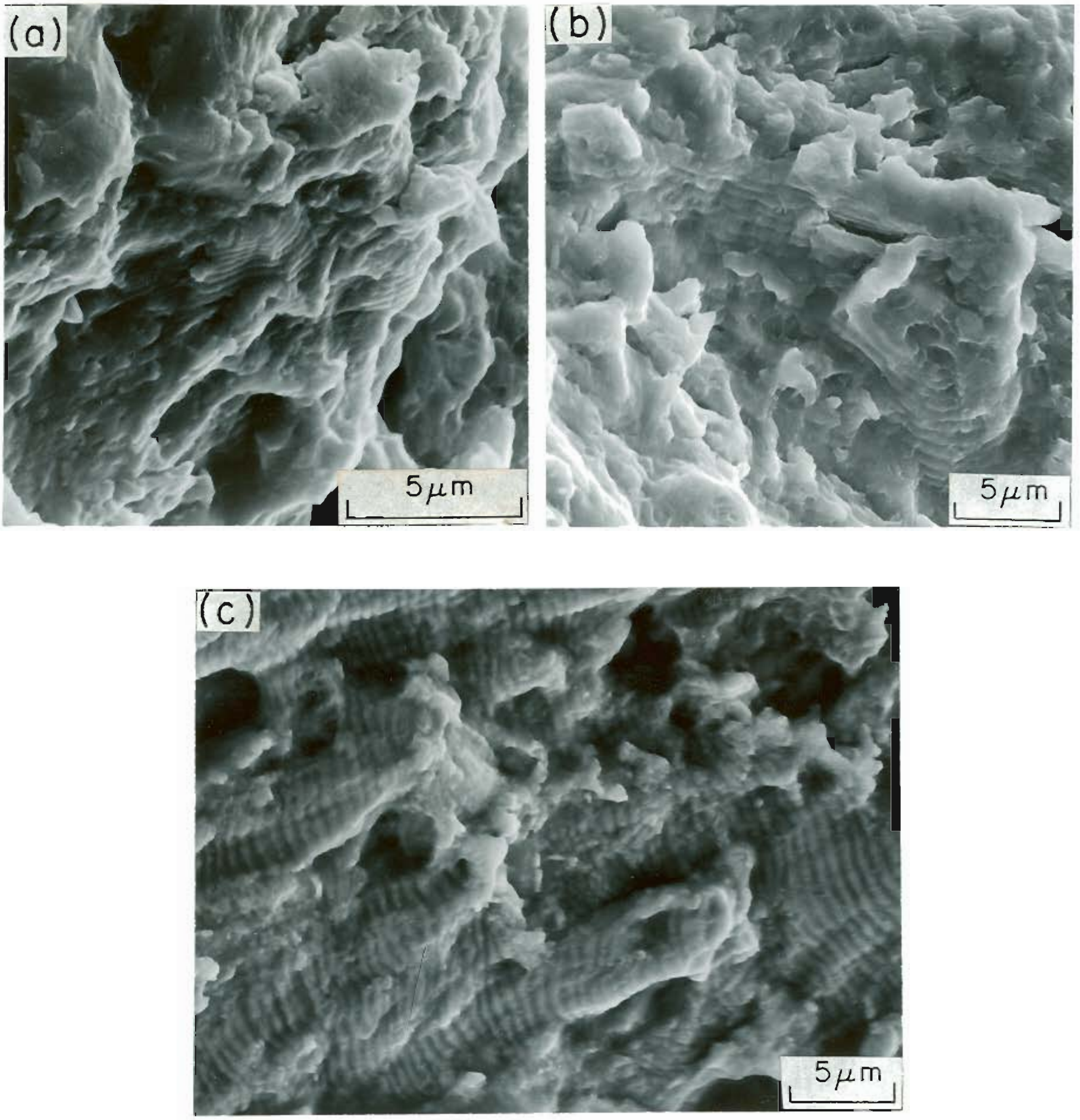

Figure 66. SEM FRACTOGRAPHS OF UNCHARGED SPECIMENS SHOWING THE VARIATION OF FATIGUE STRIATIONS WITH AUSTENITIZING TEMPERATURE

(a) AUSTENITIZED AT 870°C AND TEMPERED AT 180°C $(\Delta K \approx 17\ \mathrm{Ksi}\sqrt{\mathrm{in}})$

(b) AUSTENITIZED AT 1100°C AND TEMPERED AT 180°C $(\Delta K \approx 26\ \mathrm{Ksi}\sqrt{\mathrm{in}})$

(c) AUSTENITIZED AT 1200°C AND TEMPERED AT 180°C $(\Delta K \approx 26\ \mathrm{Ksi}\sqrt{\mathrm{in}})$.

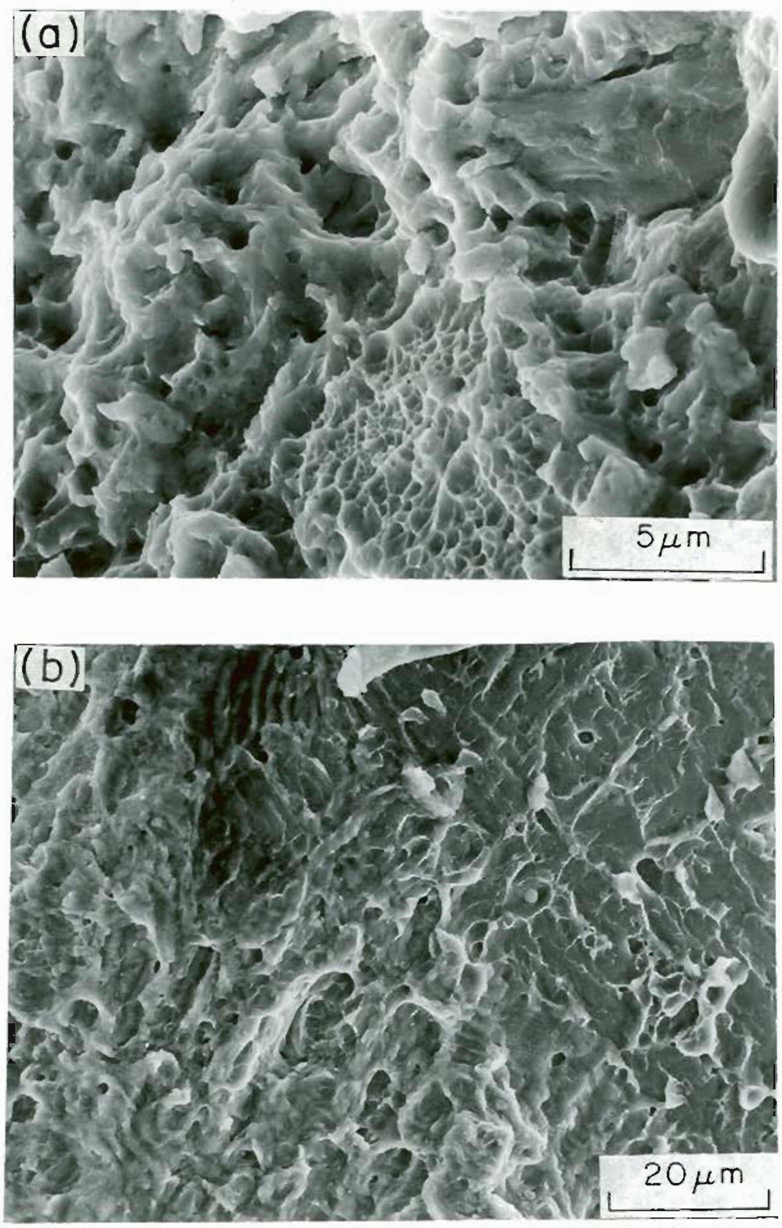

Figure 67. SEM FRACTOGRAPHS OF UNCHARGED SPECIMENS SHOWING THE STATIC FAILURE MODES

(a) AUSTENITIZED AT 870°C AND TEMPERED AT 180°C AT $\Delta K \approx 28$ Ksi$\sqrt{in}$

(b) AUSTENITIZED AT 1200°C AND TEMPERED AT 180°C AT $\Delta K \approx 45$ Ksi$\sqrt{in}$.

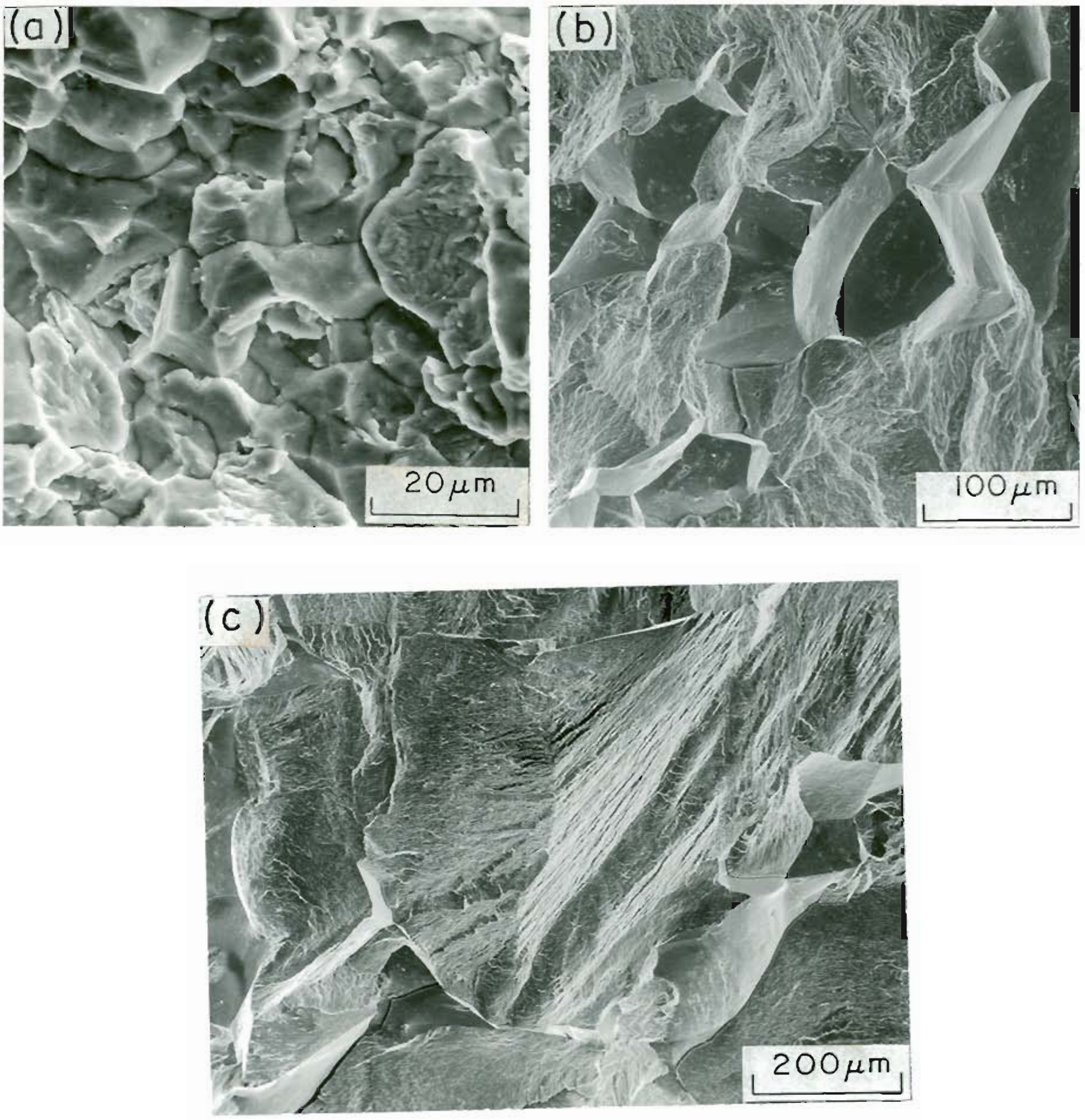

Figure 68. SEM FRACTOGRAPHS OF CHARGED SPECIMENS SHOWING THE VARIATION OF INTERGRANULAR FRACTURE WITH AUSTENITIZING TEMPERATURE AT $\Delta K \approx 3$ Ksi$\sqrt{in}$ FOR 180°C TEMPERED CONDITION

(a) 870°C

(b) 1100°C

(c) 1200°C.

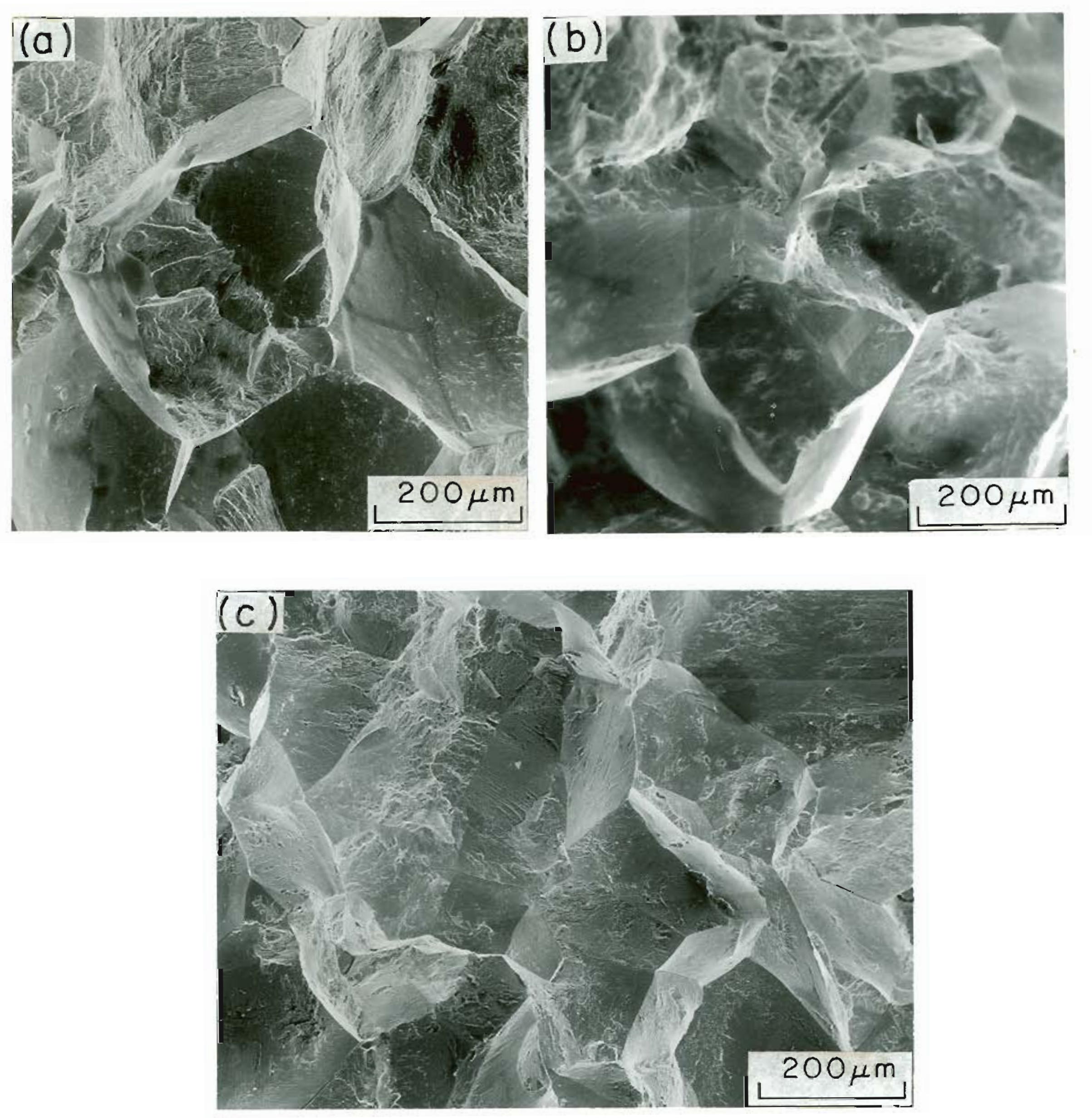

Figure 69. SEM FRACTOGRAPHS OF CHARGED SPECIMENS AUSTENITIZED AT 1200°C AND TEMPERED AT 180°C SHOWING THE VARIATION OF INTERGRANULAR FRACTURE WITH STRESS INTENSITY RANGE

(a) $\Delta K \simeq 5$ Ksi$\sqrt{\text{in}}$

(b) $\Delta K \simeq 13$ Ksi$\sqrt{\text{in}}$

(c) $\Delta K \simeq 22$ Ksi$\sqrt{\text{in}}$.

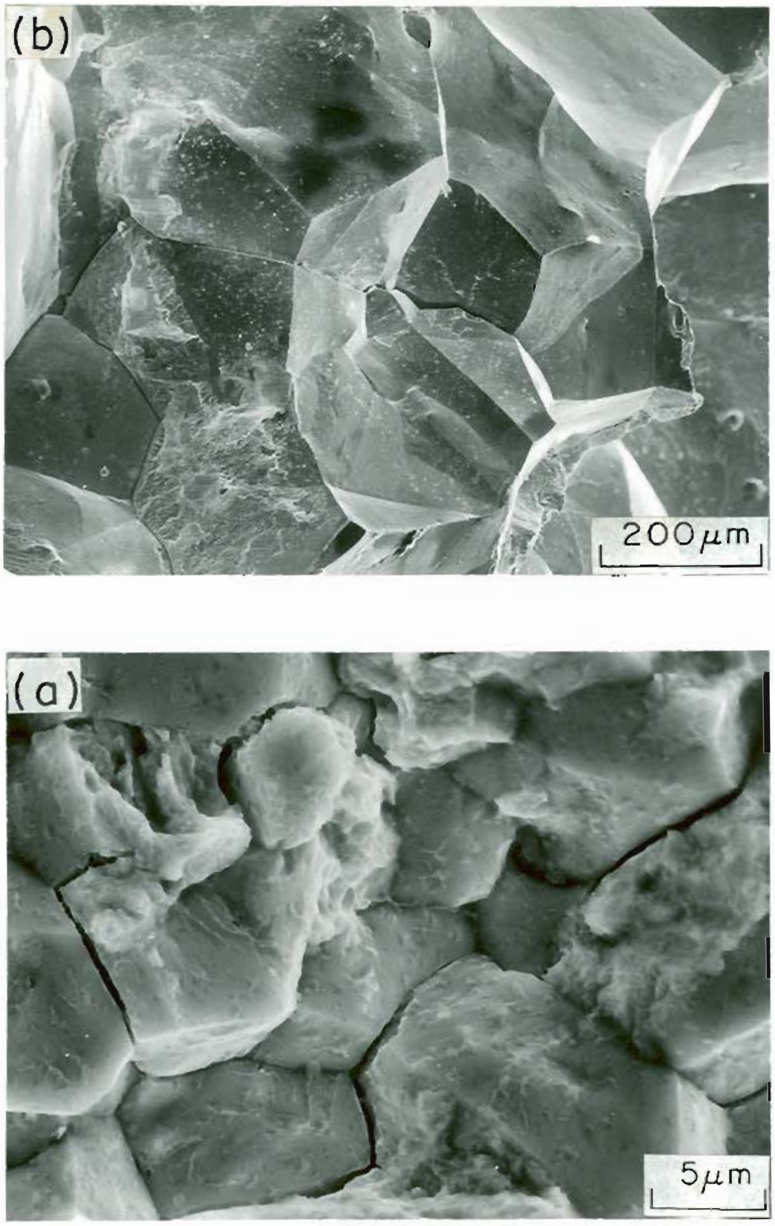

Figure 70. SEM FRACTOGRAPHS OF CHARGED SPECIMENS

(a) AUSTENITIZED AT 870°C AND TEMPERED AT 280°C $\Delta K \simeq 7$ Ksi$\sqrt{\text{in}}$

(b) AUSTENITIZED AT 1200°C AND TEMPERED AT 280°C SHOWING INTERGRANULAR FRACTURE $\Delta K \simeq 18$ Ksi$\sqrt{\text{in}}$.

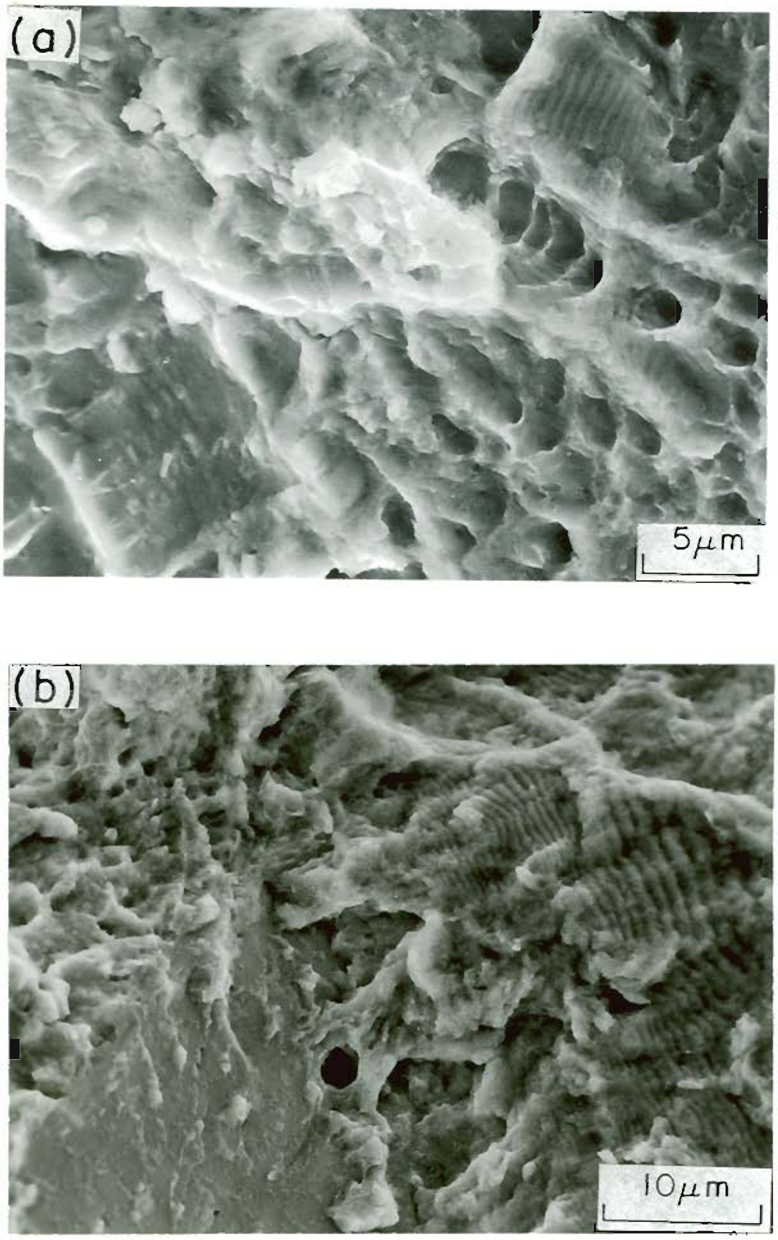

Figure 71. SEM FRACTOGRAPHS OF CHARGED SPECIMENS AUSTENITIZED AT 1200°C AND TEMPERED AT 180°C SHOWING FATIGUE STRIATIONS AND DUCTILE RUPTURE

(a) $\Delta K \simeq 22$ Ksi$\sqrt{in}$

(b) $\Delta K \simeq 31$ Ksi$\sqrt{in}$.

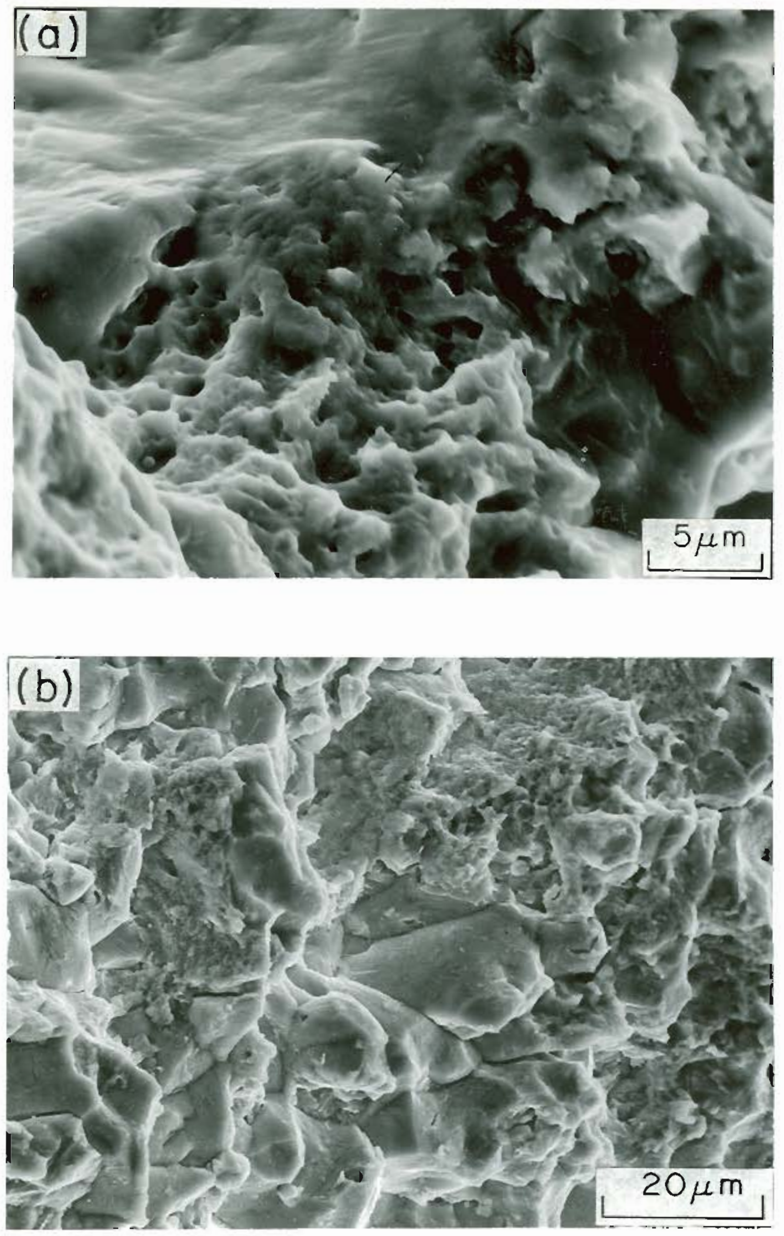

Figure 72. SEM FRACTOGRAPHS OF CHARGED SPECIMENS SHOWING DUCTILE RUPTURE

(a) AUSTENITIZED AT 870°C AND TEMPERED AT 180°C ($\Delta K \simeq 14$ Ksi$\sqrt{\text{in}}$)

(b) AUSTENITIZED AT 870°C AND TEMPERED AT 280°C ($\Delta K \simeq 22$ Ksi$\sqrt{\text{in}}$).

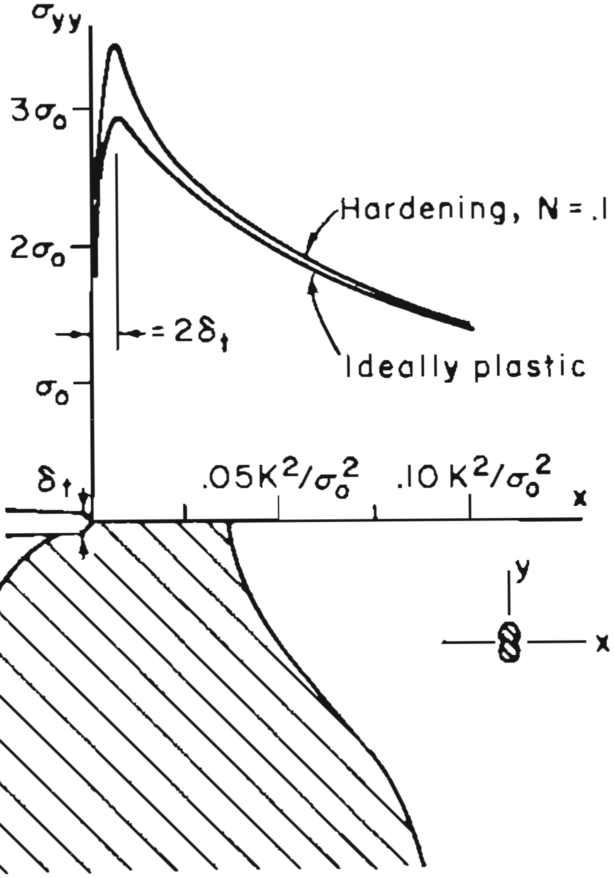

Figure 73. STRESS DISTRIBUTION AHEAD OF A CRACK.

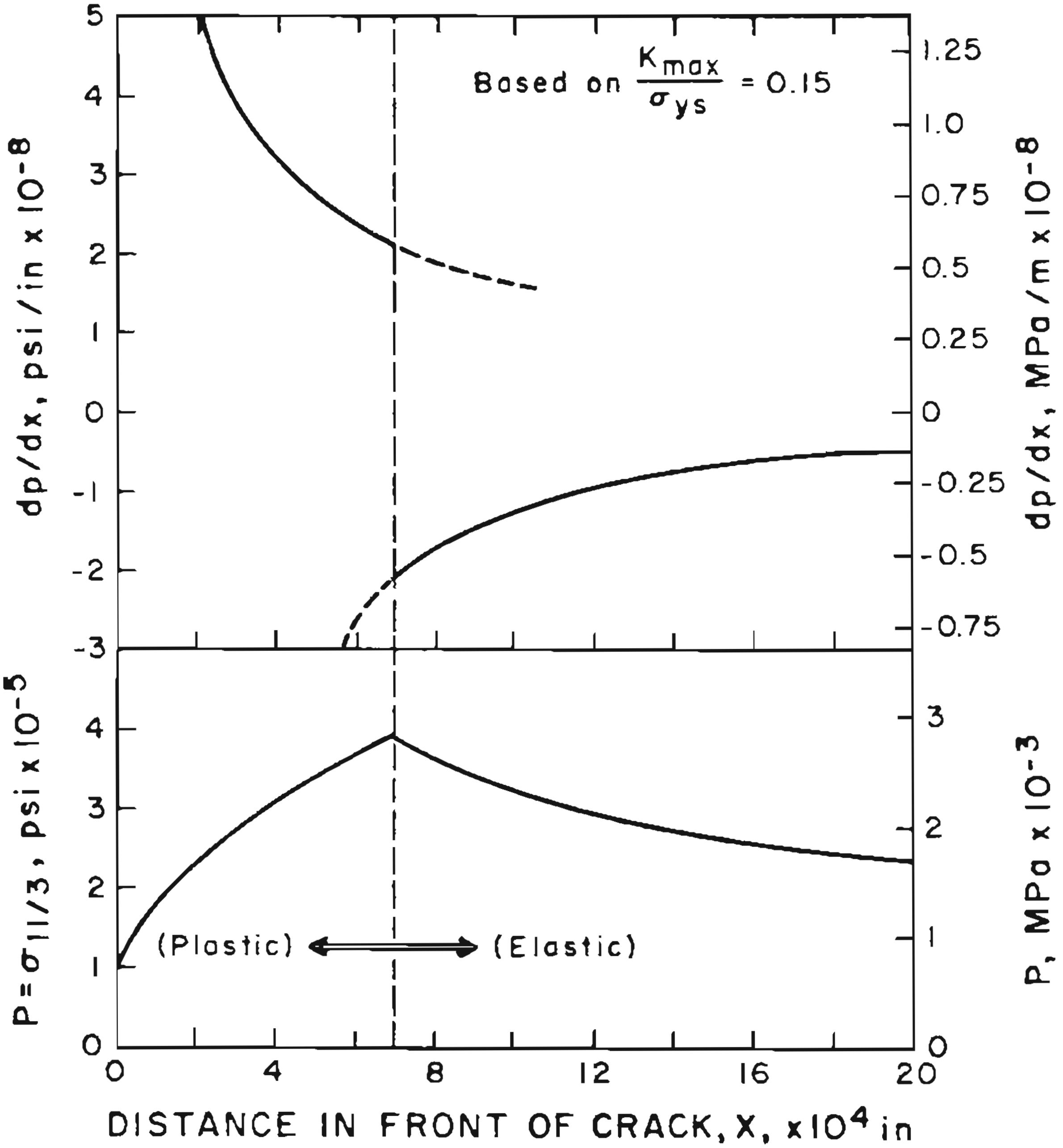

Figure 74. ELASTIC AND PLASTIC PRESSURE TENSORS AND PRESSURE TENSOR GRADIENTS FOR TYPICAL CONDITIONS APPROPRIATE TO INTERMEDIATE STRESS INTENSITIES.

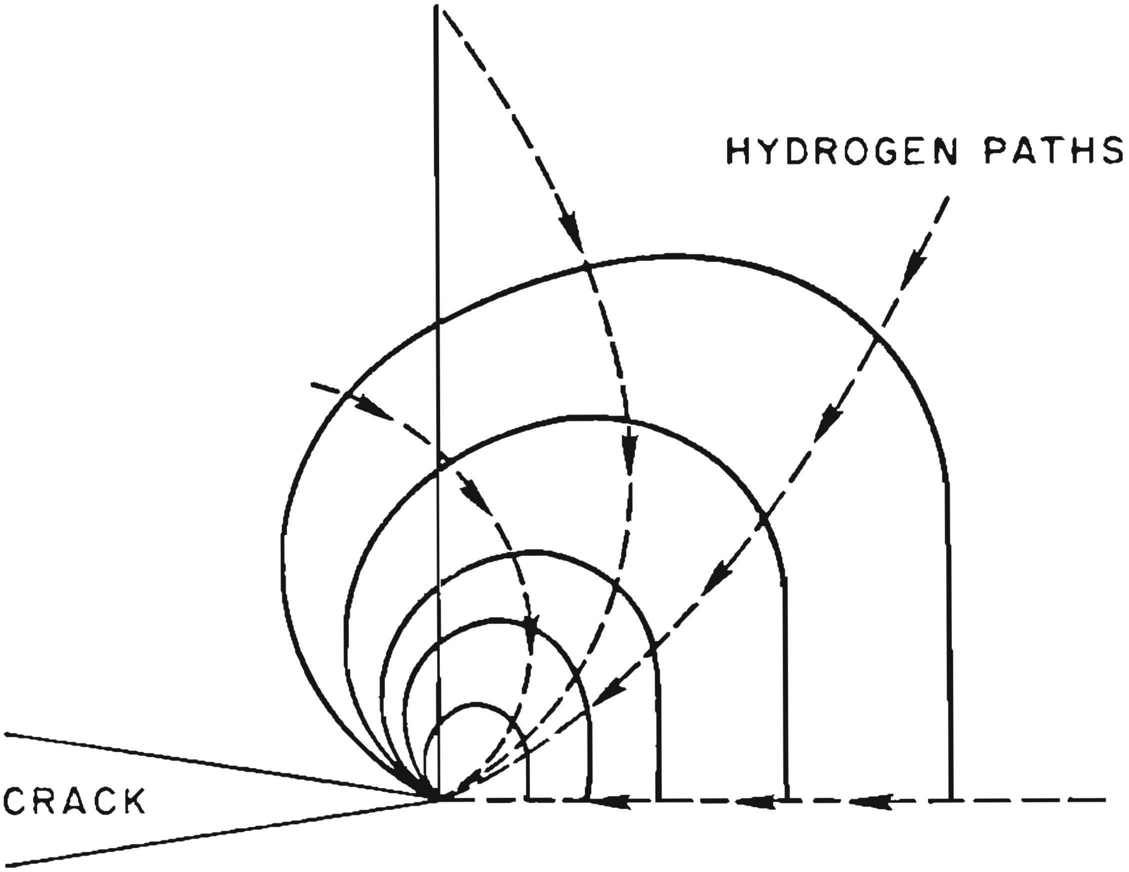

Figure 75. HYDROGEN DIFFUSION UNDER AN ELASTIC MODE I STRESS FIELD.

REFERENCES

1. G. Y. Lai, W. E. Wood, R. A. Clark, V. F. Zackay, and E. R. Parker; Met. Trans., 1974, V. 5, p. 1663.

2. R. O. Ritchie, B. Francis, and W. L. Server; Met. Trans., 1976, V. 7A, p. 831.

3. D. S. McDarmaid; Metals Tech, 1978, V. 5, p. 7.

4. J. L. Youngblood and M. Raghavan; Met. Trans., 1977, V. 8, p. 1439.

5. R. A. Clark, R. O. Ritchie and J. F. Knott; Nat. Phy. Sci., 1972, V. 239, p. 104.

6. W. E. Wood; Engg. Fract. Mech., 1975, V. 7, p. 219.

7. R. M. Horn and R. O. Ritchie; Met. Trans., 1978, V. 9A, p. 331.

8. M. F. Carlson and R. O. Ritchie; Scripta Met., 1977, V. 11, p. 1113.

9. R. O. Ritchie; Metal Science, 1977, V. 11, p. 368.

10. J. F. Lessar and W. W. Gerberich; Met. Trans., 1976, V. 7A, p. 953.

11. C. S. Carter; Corrosion, 1969, V. 25, p. 423.

12. D. Dilipkumar; Ph.D. Thesis, Oregon Graduate Center, Beaverton, 1980.

13. A. R. Marder and G. Kraus; Trans. ASM, 1967, V. 60, p. 651.

14. P. M. Kelly and J. Nutting; Proc. Roy. Soc., 1960, V. 259A, p. 45.

15. T. Ogura, C. J. McMahan, H. C. Feng, and V. Vitec; Acta Met., 1978, V. 26, p. 1317.

17. H. H. Johnson and P. C. Paris; Engg. Fract. Mech., 1968, V. 1, p. 3.

18. P. C. Paris and F. Erdogan; Trans ASME, 1963, V. 85, p. 528.

19. W. G. Clark, Jr.; Engg. Fract. Mech, 1968, V. 1, p. 385.

20. N. E. Frost, L. P. Pook, and K. Denton; Engg. Fract. Mech, 1971, V. 3, p. 109.

21. C. E. Richards and T. C. Lindley; Engg. Fract. Mech, 1972, V. 4, p. 951.

22. C. J. Beevers, R. J. Cooke, J. F. Knott, and R. O. Ritchie; Metal Science, 1975, V. 9, p. 119.

23. W. W. Gerberich and N. R. Moody; Fatigue Mech., ASTM, STP 675, 1979, p. 292.

24. T. C. Lindley, C. E. Richards, and R. O. Ritchie; Metallurgia Metal Forming, 1976, V. 43, p. 268.

25. C. J. Beevers; Advances in Research on Strength and Fracture of Materials (Ed. D. M. R. Taplin), Waterloo, Canada, 1977, V. 1, p. 239.

26. R. O. Ritchie; Met. Trans., 1977, V. 8A, p. 1131.

27. J. A. Bagley and P. R. Toolin; Intl. Journal of Fract., 1973, V. 9, p. 243.

28. P. R. V. Evans, N. B. Owens, and B. E. Hopkins; Engg. Fract. Mech., 1971, V. 3, p. 463.

29. R. O. Ritchie and J. F. Knott; Acta Met., 1973, V. 21, p. 639.

30. R. O. Ritchie; Journal of Engg. Materials, Trans ASME H, 1977, V. 99, p. 175.

31. P. N. Theilin, and M. E. Fine; Met. Trans., 1975, V. 6A, p. 2133.

32. C. T. Hahn and R. Simon; Engg. Fract. Mech., 1973, V. 5, p. 523.

33. P. T. Heald, T. C. Lindley, and C. E. Richards; Mat. Sci. Engg., 1972, V. 10, p. 235.

34. J. P. Benson; Metal Science, 1979, V. 13, p. 535.

35. J. Masounave and J. P. Bailon; Scripta Met., 1976, V. 10, p. 165.

36. E. K. Priddle; Scripta Met., 1978, V. 12, p. 49.

37. M. Klensil, M. Holzman, P. Lukas and P. Rys; J. Iron Steel Inst., 1969, V. 203, p. 47.

38. P. E. Irving and A. Z. Kurzfield; Metal Science, 1978, V. 12, p. 495.

39. R. J. Cooke, P. E. Irving, G. S. Booth, and C. J. Beevers; Engg. Fract. Mech., 1975, V. 7, p. 69.

40. R. J. Cooke, and C. J. Beevers; Mat. Sci. Engg., 1974, V. 13, p. 201.

41. R. J. Cooke and C. J. Beevers; Engg. Fract. Mech., 1973, V. 5, p. 1061.

42. G. Clark, A. C. Pickard and J. F. Knott; Engg. Fract. Mech., 1976, V. 8, p. 449.

43. P. C. Paris, R. J. Bucci, E. T. Wessel, W. G. Clark, and T. R. Mager; ASTM STP 513, 1972, p. 141.

44. T. C. Lindley and C. E. Richards; Mat. Sci. Engg, 1974, V. 14, p. 281.

45. B. P. Haigh; J. Inst. Metals, 1917, V. 18, p. 55.

46. H. J. Gough, and D. G. Sopwith; J. Inst. Metals, 1932, V. 49, p. 93.

47. E. P. Dahlberg; Trans. ASM, 1965, V. 58, p. 46.

48. W. A. Spitzig, and R. P. Wei; Trans. ASM, 1967, V. 60, p. 279.

49. A. J. McEvily and R. P. Wei; Proc. Intl. Conf. on Corrosion Fatigue, University of Connecticut, NACE2, 1972, p. 381.

50. R. P. Wei and G. W. Simmons; Stress Corrosion Cracking and Hydrogen Embrittlement of Iron base Alloys, NACE 5, 1973, p. 751.

51. G. A. Miller, S. J. Hudak, and R. P. Wei; ASTM Journal of Testing and Evaluation, 1973, V. 1, p. 524.

52. J. P. Galligher; Journal of Materials JMLSA, 1971, V. 3, p. 941.

53. J. M. Barsom; Engg. Fract. Mech, 1971, V. 3, p. 15.

54. J. M. Barsom; Intl. Journal of Fract. Mech., 1971, V. 7, p. 163.

55. I. M. Austen and P. McIntyre; Metal Science, 1979, V. 13, p. 420.

56. I. M. Austen and E. F. Walker; Proc. Intl. Conf. on Effect of Environment on Fatigue, London (I. Mech. E), 1977, p. 1.

57. I. M. Austen and E. F. Walker; Mech. of Env. Sensitive Cracking of Materials, London (Met. Soc), 1977, p. 334.

58. A. T. Stewart; Proc. Intl. Conf. on Effect of Environment on Fatigue, London (I. Mech. E), 1977, p. 291.

59. P. Machneier, C. D. Little, M. H. Horowitz, and R. P. Oates; Metals Tech, 1979, V. 6, p. 291.

60. J. D. Frandsen and H. L. Marcus; Met. Trans., 1977, V. 8A, p. 265.

61. J. D. Frandsen, N. E. Paton, and H. L. Marcus; Met. Trans., 1974, V. 5, p. 1655.

62. D. P. Williams and H. G. Nelson; Met. Trans., 1970, V. 1, p. 63.

63. R. P. Gonfolf and R. P. Wei; Scripta Met, 1974, V. 8, p. 661.

64. C. G. Hancock and H. H. Johnson; Trans. Met. Soc. AIME, 1966, V. 236, p. 513.

65. R. P. Wei and J. D. Landes; ASTM Journal of Testing, 1969, V. 9, p. 25.

66. W. W. Gerberich, J. P. Birat and V. F. Zackay; Proc. Intl. Conf. on Corrosion Fatigue, University of Connecticut, NACE 2, 1972, p. 396.

67. R. J. Bucci; Ph.D. Thesis, Lehigh University, 1970.

68. K. B. Davies and C. E. Fedderson; Intl. Journal of Fract., 1973, V. 9, p. 116.

69. G. E. Forsythe; J. Soc. Indust. Appl. Math, 1957, V. 5, p. 74.

70. R. O. Ritchie; Report, Dept. of Metallurgy, University of Cambridge, London, 1972.

71. M. F. Brown and J. E. Srawley; ASTM STP381, 1965, p. 113.

72. M. S. Bhat; Ph.D. Thesis, University of California, Berkeley, 1977.

73. K. B. Das; ASTM STP 543, 1974, p. 106.

74. N. C. Law, R. P. Howell, and D. V. Edmonds; Metal Science, 1979, V. 13, p. 507.

75. B. V. N. Rao, J. Y. Koo, and G. Thomas; Proc. of EMSA, 1975, p. 30.

76. J. M. Chilton, C. J. Barton, and G. R. Speich; J. Iron & Steel Inst., 1970, p. 184.

77. M. F. Carlson, B. V. N. Rao, and G. Thomas; Met. Trans., 1979, V. 10A, p. 1273.

78. E. R. Parker; Met. Trans., 1978, V. 9A, p. 1033.

79. K. H. Khan, and W. E. Wood; Met. Trans., 1978, V. 9A, p. 899.

80. G. B. Olsen and M. Cohen; Met. Trans., 1976, V. 7A, p. 1095.

81. F. Licroisey and A. Pinean; Met. Trans., 1972, V. 3, p. 387.

82. D. H. Haung, and G. Thomas; Met. Trans., 1977, V. 8A, p. 1661.

83. A. Kamada, N. Koshizuka, and T. Funakoshi; Trans. Journal of Iron and Steel Institute, 1976, V. 16. p. 407.

84. K. H. Khan and V. C. Kannan; Proc. EMSA, 1977, p. 256.

85. G. Thomas and B. V. N. Rao; Proc. Intl. Conf. on Martensite Transformation, Keive, Naukora USSR, 1978, p. 57.

86. B. V. N. Rao; Met. Trans., 1979, V. 10A, p. 645.

87. M. Sarikaya, B. V. N. Rao, and G. Thomas; Proc. EMSA, 1979, p. 538.

88. C. K. Syn, B. Fultz, and J. W. Morris; Met. Trans., 1978, V. 9A, p. 1635.

89. C. L. Magee and R. G. Davies; Acta Met., 1971, V. 19, p. 345.

90. V. F. Zackay and E. R. Parker; Alloy and Microstructural Design (ed. J. K. Tein), Academic Press, 1976, p. 213.

91. A. S. Tetelman and A. J. McEvily; Fract. of Structural Materials, John Wiley & Sons, Inc., New York, 1967, p. 252.

92. G. R. Speich and W. C. Lesle; Met. Trans., 1972, V. 3, p. 1043.

93. R. W. K. Honeycombe; Structure and Strength of Alloys, Climax Molybdenum Publication, 1974.

94. G. Y. Lai; Met. Trans., 1975, V. 6A, p. 1649.

95. S. Murphy and A. Whiteman; Met. Trans., 1970, V. 1, p. 1469.

96. K. H. Jack; Journal of Iron & Steel Inst., 1951, V. 169, p. 26.

97. D. H. Haung and G. Thomas; Met. Trans., 1971, V. 2, p. 1587.

98. R. D. Goolsby, W. E. Wood, E. R. Parker, and V. F. Zackay; Electron Microscopy and Structure of Materials (ed. G. Thomas), University of California Press, 1972, p. 798.

99. R. M. Horn and R. O. Ritchie; Met. Trans., 1978, V. 9A, p. 1039.

100. A. K. Seal and R. W. K. Honeycombe; J. Iron & Steel Inst., 1958, V. 188, p. 9.

101. Y. Bagaryatskii; Dokl. Akad. Nauk. SSSR, 1950, V. 73, p. 1161.

102. W. E. Wood, Tech. Report, N 00019-77-C-0135, Feb. 1978.

103. G. A. Miller; Trans. ASM, 1968, V. 61, p. 442.

104. G. A. Miller; Trans. ASM, 1969, V. 62, p. 615.

105. R. M. N. Pelloux; Engg. Fract. Mech., 1970, V. 1, p. 697.

106. H. W. Liu; J. Basic Engg. Trans. ASME, D, 1963, V. 85, p. 116.

107. P. S. Pao, W. Wei, and R. P. Wei; Envi. Sensitive Fract. Engg. Materials, (Z. A. Forolius, ed.), Proc. TMS-AIME Fall Meeting, 1977, p. 565.

108. M. Nageswararao, R. Meyer, M. Wilhelm, and V. Gerold; Proc. Intl. Conf. Mech. Env. Sensitive Cracking of Materials, London (Met. Soc), 1977, p. 383.

109. A. R. Troiano; Trans. ASM, 1960, V. 52, p. 54.

110. J. D. Frandsen and H. L. Marcus; Scripta Met., 1975, V. 9, p. 1089.

111. R. O Ritchie, M. H. C. Cedeno, V. F. Zackay, and E. R. Parker; Met. Trans., 1978, V. 9A, p. 35.

112. W. W. Gerberich, Y. T. Chen, and C. St. John; Met Trans., 1975, V. 6A, p. 1485.

113. J. K. Tien; Effect of Hydrogen on Behavior of Materials, (A. W. Thompson et al. Ed.) TMS-AIME Publication, 1975, p. 309.

114. J. R. Rice and M. A. Johnson; Inelastic Behavior of Solids, (M. F. Kanninen et al. Ed) McGraw-Hill, New York, 1970, p. 641.

115. R. J. Richards, S. Purushothaman, J. K. Tien, J. D. Frandsen, and O. Buck; Met. Trans., 1978, V. 9A, p. 1107.

116. R. O. Ritchie, J. F. Knott, and L. C. E. Geniets; The Microstructure and Design of Alloys, Proc. 3rd Intl. Conf. on Strength of Metals and Alloys, London, 1973, p. 124.

117. C. J. McMahan, D. L. Briant, and S. K. Banerji; Advance in Research on Strength and Fracture, (D. M. R. Taplin, Ed) Waterloo, Canada, 1977, V. 1, p. 19.

118. K. Yoshino and C. J. McMahan; Met. Trans., 1974, V. 5, p. 363.

119. C. L. Briant, and S. K. Banerji; Intl. Metals Reviews, 1978, V. 4, p. 164.

120. C. L. Briant and S. K. Banerji; Met. Trans., 1979, V. 10A, p. 1729.

121. G. W. Simmons, P. S. Pao, and R. P. Wei; Met. Trans., 1978, V. 9A, p. 1147.

122. G. Thomas; Met. Trans., 1978, V. 9A, p. 439.

123. B. D. Graig; Acta Met., 1977, V. 25, p. 1027.

124. P. C. Hughes, I. R. Lamborn, and B. B. Liebert; J. Iron Steel Inst., 1965, V. 203, p. 728.

125. W. S. Owen; ibid., 1954, V. 177, p. 445.

126. A. S. Tettleman; Fundamental Aspects of Stress Corrosion Cracking, NACE, Houston, Texas, 1969, p. 446.

127. W. W. Gerberich; Hydrogen in Metals, (I. M. Bernstein, Ed.) ASM Ohio, 1974, p. 446.

128. R. A. Davis; Corrosion, 1964, V. 20, p. 93.

BIOGRAPHICAL NOTE

The author was born on 15 January 1950 in Kollur, India. After matriculation in 1965 he joined Government Polytechnic, Vijayanda, and received his diploma in Metallurgy in 1968. Then he joined Government Polytechnic as a teaching assistant. In 1972 while working as a teaching assistant, the author passed the associate membership examination for the Indian Institute of Metals. In 1973 the author joined the University of Roorkee, Roorkee, and received a Master of Engineering in Physical Metallurgy in 1975. Prior to joining the Oregon Graduate Center in September 1976, he worked as a Research Assistant at I.I.T., Bombay, India.

The author completed all requirements for the degree Doctor of Philosophy at the Oregon Graduate Center in September 1980.

The author has accepted a position as Advanced Engineer with Westinghouse Electric Corporation, Philadelphia, Pennsylvania.